Applications of interacting particle systems in life- and social-sciences across scales

Michael Fischer

universität wien

DISSERTATION / DOCTORAL THESIS

Titel der Dissertation / Title of the Doctoral Thesis

Applications of interacting particle systems in life- and social-sciences across scales

verfasst von / submitted by

Michael Fischer, BSc MSc

angestrebter akademischer Grad / in partial fulfillment of the requirements for the degree of

Doktor der Naturwissenschaften (Dr. rer. nat.)

Wien, 2022 / Vienna 2022

Studienkennzahl lt. Studienblatt / degree programme code as it appears on the student record sheet:	A 796 605 405
Studienrichtung lt. Studienblatt / degree programme as it appears on the student record sheet:	Mathematik
Betreut von / Supervisor:	Univ.-Prof. Dr. Christian Schmeiser
Betreut von / Supervisor:	Prof. DI Dr. Marie-Therese Wolfram

Acknowledgements

Ich würde einfach größere Türen bauen.
I would just build bigger doors.

Isaak Sattig

Much time has passed since my son made that statement. I had just told him about my first research project. At that time, I did not know that the relationship between door width and outflow still is an important topic in experimental pedestrian research. I have also learned many other things in the last few years and it is time to thank the people who have accompanied me on this journey.

I would like to start with the scientific support. First of all, there is my supervisor Marie, with whom it all began and who always sets all levers in motion when anyone, not just me, needs support. I hope the future holds more such supervisors. Then, of course, there is my supervisor Christian. Unfortunately, much of our collaboration took place during the pandemic, which made our scientific exchanges difficult some of the time. Still, it was always fascinating to work with someone with so much experience and intuition. I am thankful to Bertram for the friendly communication and productive collaboration. Thanks to Sara, who, as my official project leader, together with Christian, always helped me out when she could. After 15 years at the University of Vienna, I also have to thank the faculty. Especially the dean's office and institute team that keeps everything running and therefore supports us focussing on science. Matteo deserves a special mention here, who looks after the PhD students (and postdocs) like the apple of his eye. Through the two years of funding in Linz, RICAM was my second academic home. Therefore, I would like to thank Annette, Susanne, Peter, Flo and Wolfgang for their support of any kind. I would especially like to thank Christoph, who taught me a trick or two in Mathematica. For years, the Institute of Mathematics at BOKU has accompanied me with tireless support. Thanks to Norbert, Professor Kuba, Klaus and the rest.

Privately and often academically, my flatmate Oliver has accompanied me in my journey in math. A special thanks goes to David and Josef, who have listened to my problems over and over again. Of course I also have to mention my former office mate (and now collaborator) Laura, with whom I could philosophise about mathematics for the last four years.

I want to close this list with thanking Mani, Tobi, Saku, Lukas, Bettina, Tamar, Markus, Giulia, Julia, Julia, Raphi, Thomas, Tom, Max, Martina, the crew of V1, many more and my family, especially Sebastian and of course Isaak.

Zusammenfassung

Die vorliegende Arbeit beschäftigt sich mit der Modellierung, Analysis und Simulation verschiedener Anwendungen aus Biologie, Sozialwissenschaften und den Fußgängerdynamiken. Wir betrachten Modellierungsansätze auf mikroskopischer, mesoskopischer und makroskopischer Ebene. Wir gehen auf die Verbindung der unterschiedlichen Ebenen und deren jeweiligen Vor- und Nachteile ein, beginnend mit einer breiten Präsentation dieser Techniken in der Modellierung.

Im folgenden Kapitel 2 untersuchen wir ein soziologisches Phänomen in den Fußgängerdynamiken. Wir modellieren das im Forschungszentrum Jülich durchgeführte Experiment auf mikroskopischer Ebene und kalibrieren das Modell auch. Im Anschluss leiten wir eine partielle Differentialgleichung her und analysieren diese. Die experimentell festgestellten Phänomene reproduzieren wir auf beiden Skalen.

Im Kapitel 3 setzen wir Arbeiten zum ELO-Rating, dem verbreiteten Rating im Schachspiel, fort. Wir erweitern vorige Arbeiten um einen Faktor der Performance-Schwankung. Numerische Simulationen auf beiden Skalen zeigen eine gute Übereinstimmung zwischen mikroskopischer und mesoskopische Skala. Wir können die partielle Differentialgleichung nutzen, um analytisch zu zeigen, dass eine richtige Wahl der Parameter zu einer Konvergenz des Ratings R zur erwartenden Stärke ρ führt.

Im letzten Kapitel 4 leiten wir einen neuen diffusiven Term auf makroskopischer Ebene aus mikroskopischen Überlegungen her. Diese Herleitung ist rigorous und damit können wir die Existenz einer schwachen Lösung auf makroskopischer Ebene zeigen. Wir unterstreichen unsere Erkenntnisse mit Simulationen auf beiden Skalen.

Abstract

The present work deals with modeling, analysis and simulation of various applications in biology, social sciences and pedestrian dynamics. We consider modeling approaches at microscopic, mesoscopic, and macroscopic levels. We address the connection between the different levels and their respective advantages and disadvantages, beginning with a broad presentation of these techniques in modeling.

In the next Chapter 2, we study a sociological phenomenon in pedestrian dynamics. We model the experiment conducted at the Jülich Research Center at the microscopic level and also calibrate the model. Subsequently, we derive a partial differential equation and analyse it. We reproduce the experimentally observed phenomena at both scales.

In Chapter 3, we continue work on the ELO rating, the widely used rating in chess. We extend previous work to include a factor of performance-fluctuation. Numerical simulations on both scales show good agreement between microscopic and mesoscopic scales. We can use the partial differential equation to show analytically that a proper choice of parameters leads to a convergence of the rating R to the expected strength of ρ.

In the last Chapter 4, we derive a new diffusive term at the macroscopic level from microscopic considerations. We consider particles repelling each other within a finite radius. The macroscopic derivation is rigorous and thus we can show the existence of a weak solution on the macroscopic level. We emphasize our findings with simulations at both scales.

Contents

1 General Introduction

The right understanding of any matter and a misunderstanding of the same matter do not wholly exclude each other.

Franz Kafka in The Trial

Contents

The basic aim of mathematical modelling is to formulate, solve and, if necessary, extend or refine a mathematical model for a real problem. A mathematical model can therefore be described as any set of mathematical rules, equations and inequalities that can be calculated in a deterministic or stochastic sense and that describe an aspect of a real process, see [34, 126, 229]. Basically, the process of modelling contains the following steps,

- specification of the real problem
- choice of scales and the corresponding mathematical description
- development of the mathematical model
- analysis and solution of the model

- interpretation of the results and comparison with the real problem
- refinement or extension of the model
- presentation of the results

When choosing a model, we distinguish between qualitative and quantitative ones. The former are models that are intended to give predictions for the qualitative structure of a process. The latter are models that are to be used for quantitative predictions for the values of variables, see [34, 126].

A distinction is also made in modelling between deterministic and stochastic models, see [34]. Deterministic models are based on known physical laws or laws from another discipline. The same input will always lead to the same result. In contrast, stochastic models contain probability distributions. As a result, the same input can lead to different output values.

Modeling includes many different fields of mathematics. Examples are dynamical systems, differential equations, game theoretic approaches, or statistical models. The last two fields are widely used in psychology, sociology, political science and economics, see [14, 176, 197]. Dynamical systems and differential equations, on the other hand, are widely used in the natural sciences, e.g., physics, earth sciences, chemistry, engineering and computer science, see [62, 168]. Mathematics has also found its place in the aforementioned social sciences and biology, where many initially believed the phenomena to be outside the realm of mathematical representation. Mathematical modeling did not become an important research tool here until the second decade of the 20th century, but first examples from modeling in genetics are in the curriculum of European schools through Mendel's theory of heredity and thus chronologically were 100 years earlier, see [90].

Before developing a mathematical model, one must be clear about the space and time scales. We briefly discuss the different scales using an example of pedestrian dynamics. Many considerations are based on microscopic ideas and interactions on that scale. The interacting objects, motivated by physics, are often called particles; in the context of pedestrians and social sciences, also agents. Most common microscopic models are 1st and 2nd ordinary differential equations (ODE) for position x and velocity v, they are off-lattice based, therefore continuous in space. Also off-lattice are stochastic differential equations (SDE). In comparison to ODEs one or more of the terms is a stochastic process, resulting in a solution which is also a stochastic process. Therefore it is a non-deterministic model. Often SDEs contain a variable which represents random white noise modelling some perturbation. Lattice-based cellular automata (CA) are also widely used. They are discrete in time and space. There are both deterministic and stochastic versions. John Conway's Game of Life is a famous example of the former. In the example of pedestrian dynamics, the latter is more common. On a microscopic scale, we trace the trajectory, i.e., the location x_i as a function of time t, of a single agent i depending e.g. of its velocity v_i and the position of other agents x_j.

Mesoscopic or kinetic models are static representations of a density as a function of the so-called single-particle distribution f representing states of the microscopic particles. Kinetic models are partial differential equations. The best known example of a mesoscopic PDE is the now-called Boltzmann equation, see [27]. Here $f = f(x, v, t)$ is a probability density function defined to represent the number of molecules having momentum v at position x at time t. In the previous context the function $f(x, v, t)$ then gives the probability of finding an agent with property/velocity v at position x at time t. More precisely, $f(x, v, t)dxdv$ gives the average number of pedestrians just mentioned in the reference space $dxdv$.

The macroscopic scale also now represents the density $\rho = \rho(x, t)$ of pedestrians at position x at time t and not any longer distinguishes by e.g. velocity v, detecting just the collective mass. It can be retrieved from a kinetic model via $\rho(x, t) = \int f(x, v, t)dv$.

The particle description is the natural level to describe interactions of pedestrians, bacteria and cells. Nevertheless, difficulties can arise both mathematically and for the applications. For systems of ordinary differential equations a wide theory of existence and regularity was established that also goes back a long way historically. However, this is not true, for example, in the case of cellular automata, which are widely used in pedestrian dynamics. Also, on a microscopic level the long term behaviour often needs to be predicted via simulations. Numerically systems with 50000 agents (evacuation of a soccer stadium) become expensive or even impossible - in the context of gas dynamics, see [63, 178]. The kinetic level considers a multidimensional partial differential equation. This has numerical advantages over the microscopic, but often still involves a high dimensional problem. An approximation of microscopic dynamics only works if the number of particles is large. In a certain way it is still a microscopic description of the system, emergent phenomena often cannot be described by it, see [58, 157]. The macroscopic level carries the least information. However, there is an established theory for long-term- and stability-behaviour. Often faster numerical solvers exist.

Depending on the application, one of the three mentioned scales is more appropriate. But as we will discuss in the context of pedestrian dynamics, even within a scale, different approaches have different advantages and disadvantages, compare [157, 201]. In the following, we present the different scales, their modeling approaches, and the changing of scales. We mention studied and occurring phenomena. We motivate why a change of scale is often helpful in applications or for recreating introduced phenomena.

We begin with a detailed overview of the various microscopic models and phenomena that occur. We present a change of scale on three examples and mention other important techniques. A brief overview of the relevant terms in the context of PDEs is followed by an overview of the applications and the linkage of the different scales.

1.1 Microscopic models

Microscopic modeling is used not only in physics and mathematics but in many sciences. Among other famous examples are economics, traffic flow, biology and medicine [139, 155, 196]. In physics we often speak of particles, in the social sciences of agents and individuals, and in biology of cells or bacteria.

1.1.1 Pedestrian dynamics

The modeling of pedestrian dynamics has gained a lot of attention in recent years. First physics and engineering were interested in those dynamics, now psychology, mathematics and sociology contribute their share, see [227]. Especially due to the catastrophe at the Loveparade festival in Duisburg in 2010, a focus on evacuation scenarios and geometry optimization has emerged, see [107]. This also plays a role in organizing demonstrations or the design of subway stations. Mathematical models have been successfully applied in the pilgrim site of Mecca, where deaths have occurred repeatedly in the past due to large crowds, see [123].

Models for pedestrian dynamics are often defined on a bounded domain $\Omega \subset \mathbb{R}^2$ as in Figure (1.1a). We distinguish in the boundary $\partial\Omega$ between walls Γ_W, obstacles Γ_O and entries and exits Γ_I, Γ_E. These models can be discrete or continuous in space. Depending on the model, the boundary is implemented differently. In evacuation models, the shortest path to a destination, e.g. Γ_E, is an important concept. In a domain Ω the distance of a point x to an exit Γ_E is known to be given via

(a) Exit Γ_E and the wall Γ_W, mathematically seen it is the boundary of Ω.

(b) An obstacle Γ_O in front of the exit Γ_E.

Figure 1.1: The effect of FRO means that the exit time t^* is reduced by the obstacle Γ_O. Thus, obstacles accelerate an evacuation process.

the solution of the (uncoupled) **Eikonal-equation**:

$$\begin{aligned} \|\nabla V(x)\|^2 &= 1, \quad \text{for } x \text{ in } \Omega, \\ V(x) &= 0, \quad \text{on } x \text{ in } \Gamma_E, \end{aligned} \tag{1.1}$$

with homogenous Dirichlet-boundary conditions on the exit Γ_E. Pedestrians generally do not always choose the shortest path to an exit. In [58] the authors discuss among others the shortest, the easiest and the path with minimal angle change. In models that are discrete in space, one usually assumes a quadratic grid, accordingly $\Delta x = \Delta y$. The distance measurement to an output Γ_E is then motivated either by the distance of the field centre point to Γ_E via (1.1) or by the number of fields needed to be passed to reach Γ_E.

Effects and Phenomena

In the microscopic modeling of pedestrians, many effects occur that are not physically motivated but whose cause is sociological; people are individuals who e.g. look out for each other, see [58, 157]. Therefore, an important requirement for modeling is to reflect these phenomena. We present phenomena in pedestrian dynamics as well as modeling approaches in this Subsection. In the modelling of pedestrians, **size-exclusion** is a key-element most approaches satisfy. Depending on the model, this means microscopically that agents do not overlap.

The phenomena of a **fluidizing role of an obstacle** (FRO) is discussed to have physical and sociological reasons, see [83,157]. It means that an object positioned in front of an emergency exit Γ_E as in Figure 1.1 accelerates the total duration of the evacuation process. This is a phenomena which also occurs in real evacuation situations, see [87]. It can be seen as an example of Braess paradox, see [58].

The next phenomena is the so-called **Faster-is-Slower** effect observed with pedestrians in experiments, see [6, 88, 99]. Faster-is-Slower means that evacuation-times may be slower at higher speeds. Therefore it also represents a Braess paradox, see [58]. It not only occurs in humans but also was investigated in mice, ants, see [152,208], and sheep, see [181,238], wherein they also proposed a mechanical model based on rigid grains.

So-called **Stop-and-go** waves occur in traffic and pedestrian flows. It is believed that effects of **inertia** and **delay** play an important role in this. This is being investigated experimentally and in simulations, see [157].

In many models Faster-is-Slower also leads to the following phenomena. It can happen that the particles get stuck and can no longer be loosened. This effect is called **clogging** and a minimal example is visualized in Figure 1.3b. One scenario where clogging occurs are bottlenecks, see [104, 239], which are also investigated in Chapter 2. Clogging leads to high densities ρ and, in the context of pedestrian dynamics, can lead to dangerous situations for individuals, see [6]. Therefore, it is of scientific relevance to identify such situations e.g. via microscopic simulations, see [103]. However, unlike in e.g. granular models, clogs dissolve again in situations with pedestrians.

Another phenomenon of self-organisation of pedestrians is that of **Lane-formations**. Lane-formation occur in bi-directional flows. It is seen as a direct result of minimizing conflicts in the two different streams and was investigated in multiple experiments [109,234]. In bidirectional flow situations, pedestrians self-organize into separate segregated lanes. Unlike in vehicle traffic, lanes form dynamically and naturally in pedestrian dynamics. The mechanisms behind this seemingly organized separation of the crowd are not known for certain and in many cases are random without external synchronization or prior agreement between pedestrians. At the microscopic level, this phenomenon was studied in bi-directional pedestrian walkways, see [25,85].

In the following we discuss different microscopic models for $N+1$ individuals. We restrict the presentation to 1D; its generalization to 2D is not necessarily straight forward.

Follow-The-Leader model

The **Follow-The-Leader** model (FTL) is widely used in traffic dynamics and is also used for pedestrians, see [91, 237]. It is a continuous in space ODE-system. The agents are aligned in a straight line as can be seen in Figure 1.2. The velocity of agent x_i is then given by

$$\frac{d}{dt}x_i(t) = \theta\left(x_{i+1}(t) - x_i(t)\right), \quad 0 \le i \le N-1 \tag{1.2}$$

and depending on x_N it can be a periodic model. We then have $x_N = x_0$. Here θ is a non-negative function, an example of such a function governing the dynamics is

$$\theta(z) = \begin{cases} U(1-\exp(-\frac{z-k}{z_s})), & z \ge k \\ 0, & z < k \end{cases}.$$

Here k denotes the minimal distance and U is the maximum value, therefore the desired speed. The constant z_s represents a typical distance and is for scaling reasons. Common values from the literature are $U = 1.25\frac{m}{s}$, $k = 0.3m$ and $z_s = 0.9m$.

System (1.2) is in Lagrangian coordinates. From a mathematical point of view existence of a solution to this ODE system is granted by Picard-Lindelöf's theorem when θ is Lipschitz, see [213]. While the agents always move forward one can assume that in the long time behaviour distances between agents become constant. Therefore it is common to introduce $\omega_{i+\frac{1}{2}} = \frac{x_{i+1}-x_i}{\Delta s}$, here Δs is a reference distance in Lagrangian coordinates. We then have

$$\frac{d}{dt}\omega_{i+\frac{1}{2}}(t) = \frac{1}{\Delta s}\left(\theta(\omega_{i+\frac{1}{2}}(t)) - \theta(\omega_{i-\frac{1}{2}}(t))\right), \quad 1 \le i \le N-1.$$

Therefore ω is dimensionless. Depending on θ different phenomena can be reproduced. For effects like inertia or delays second-order FTL-models are investigated. For a critical discussion of the FTL model and its extensions we refer to [157], and for its application in evacuation dynamics, see [106].

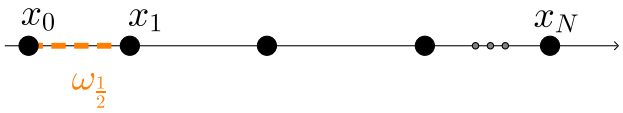

Figure 1.2: $N+1$ agents x_i in the FTL in 1D. For the long-time behaviour we investigate the system in $\omega_{i+\frac{1}{2}}$.

Granular Media

From a physical point of view, when modelling the effect of size-exclusion, one approach is to model it with **granular mechanics** (GM), see [31,156]. It is a continuous in space ODE-system. Here each individual i can be seen as a hard disk with radius r_i whereas there exist a non-overlapping constraint with all neighbours. We reduce ourself to the cases $r_i = r_j$ for all i, j. The non-overlapping assumption reproduces the effect of size-exclusion. This leads to $\vec{x} = (x_0, \dots, x_N)$ belonging to the set of **feasible configurations**

$$K = \{\vec{x} = (x_0, \dots, x_N) \in \mathbb{R}^n, x_{n+1} - x_n \geq 2r, \forall n = 0, \dots, N-1\}.$$

Every agent i has a velocity U_i where $U = (U_0, \dots, U_N)$ can be time-dependent. For stating the dynamics we have to define the set of **feasible velocities**

$$C_x = \{\vec{v} = (v_0, \dots, v_N) \in \mathbb{R}^n, x_{n+1} - x_n = 2r \Rightarrow v_{n+1} - v_n \geq 0\}.$$

The one-dimensional GM model then is given by

$$\frac{d}{dt} x_i(t) = P_{C_x}(U_i)$$

where P_{C_x} represents the Euclidian projection on the closed convex cone C_x. This makes the GM-model a delicate model, especially in 2D, in order to preserve the non-overlapping constraint. We therefore refer to [157] for mathematical details and mention below phenomena of pedestrian dynamics that can be reproduced with the GM.

As mentioned a GM setting automatically fulfills the effect of size-exclusion due the definition of K and C_x. For the question of mathematical well-posedness of some models we refer to [157, 158, 167]. Effective numerical algorithms are discussed in [156]. In general, the topic of granular media in pedestrian dynamics is compared with other models e.g. here [105, 173] and a clear overview is given in [157]. The authors also state a problem in simple GM models, namely the desired velocity field of agent i does not depend on other agents. Therefore, in this form, it primarily provides a basis for modelling collisions of particles. However, through this physical modelling, these basic models already provide common phenomena in pedestrian dynamics. The fluidizing role of an obstacle was investigated in [83, 157] for the GM. A GM also represents Faster-is-Slower due the occurrence of clogs. Collision-free granular models were compared with other models in [232] when investigating lane-formation.

Cellular automata

The just mentioned effect of Faster-is-Slower also occurs in other microscopic models like **Cellular Automaton** (CA). A CA is a in time and in space discrete microscopic model. CAs are widely used

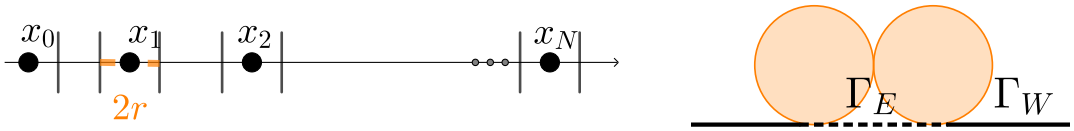

(a) $N+1$ agents (hard discs with radius r) x_i in the context of granular media in 1D.

(b) Two agents are stuck in front of an exit Γ_E.

Figure 1.3: On the left agents in a GM in a feasible configuration. On the right, clogging occurs in 2D since two agents are stuck in front of the exit.

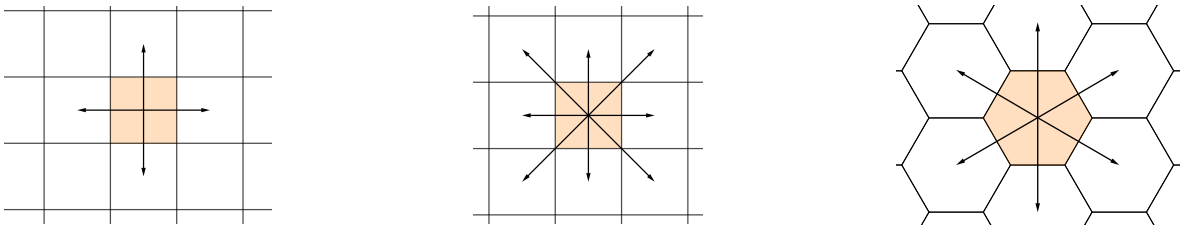

(a) A Moore neighborhood.

(b) A Von Neumann neighborhood.

(c) A hexagon neighborhood.

Figure 1.4: The three common neighborhoods for CAs.

in many sciences. In pedestrian dynamics, many commerce programs exist and their dynamics are easy to visualize and understand, see [58, 201]. Nevertheless from a mathematical point of view e.g. the long-term behaviour is difficult to predict, see [157, 190].

In a CA the domain is split into squares with $\Delta x = \Delta y$; each square can by occupied by one agent or not. Agents can move to neighbouring cells. In a so-called **Von Neumann** environment, as shown in Figure 1.4, there are four possible neighbouring cells to move. A **Moore** environment also allows the diagonal neighbouring cells. Hexagons are also used for more geometric options in complicated domains, see [86, 157].

In CAs, the effect of size-exclusion is generated in the so-called transition-rate $\mathcal{T}$. A maximum of one agent is allowed per field. However, this also does not allow a finer mesh size, because one field must correspond approximately to one pedestrian. Depending on the context, fields with $\Delta x = 0.4m$, corresponding to a maximum density of $\rho_{\max} = 6.25\,\text{pedestrians}/m^2$, are therefore mostly used. Due to calibration reasons, a field size of $0.3m$ is occasionally used as in Chapter 2. This is only a slight deviation from the actual area of pedestrians, see [104]. This constraint on geometries severely limits CAs, see [201]. Geometries like a round obstacle in Figure 1.1b are not possible and must be approximated in those cases.

The numerical implementation allows several approaches. In the simplest approach, which is nevertheless widely used, agents are updated sequentially. There are different update rules. The order is shuffled every time step or remains frozen, see [201]. The effect of size-exclusion is then implemented simply by the fact that an occupied field is not available as a possible option, see [157]. Sequential and parallel updates differ in its behaviour, see [216]. While the latter is mathematically more obvious,

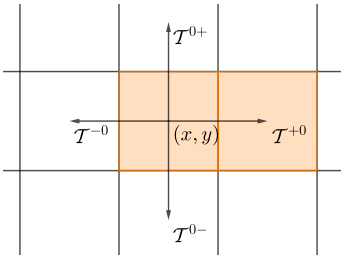

(a) Transition-rates $\mathcal{T}$ in a Von Neumann-neighborhood for an agent in (x, y). The agent is not allowed to jump to the right due to the effect of size-exclusion.

(b) SFF with exit Γ_E corresponding to a Moore neighborhood.

(c) SFF with exit Γ_E corresponding to a Von Neumann neighborhood.

Figure 1.5: Transition-rates $\mathcal{T}$ in a Von Neumann-neighborhood and two different SFFs corresponding to different neighborhoods.

the effect of size-exclusion then leads to possible conflicts, e.g. two agents want to go to a previously unoccupied field in the same time-step. In case of an occurring conflict an algorithm decides if one agent is chosen to move to the field. The agent is e.g. chosen via an uniform probability distribution. Alternatively the respective probabilities of the two agents wanting to move into the field are re-weighted, see [43, 136]. Social mechanisms were also introduced via this conflict resolution such as friction, see [135]. This implementation leads to Faster-is-Slower.

CAs are determined on a mathematical level by a so-called master-equation (ME), see [39, 157, 200]. In one dimension, this is given in the simplest case as follows:

$$\begin{aligned}\rho(x, t + \Delta t) - \rho(x, t) = &- \rho(x, t)\mathcal{T}^{+}(x, t) - \rho(x, t)\mathcal{T}^{-}(x, t) \\ &\rho(x + \Delta x, t)\mathcal{T}^{-}(x + \Delta x, t) + \rho(x - \Delta x, t)\mathcal{T}^{+}(x - \Delta x, t).\end{aligned}$$

It is important to see that the ME does not describe the development for agents i but for the change in density ρ in a field x at time t. Here ρ can only take discrete values $\rho \in \{0, 1\}$.

In the so-called transition-rate $\mathcal{T}$ the dynamics can be incorporated. In the simplest case $\mathcal{T} = const.$ the CA corresponds to a random walk. The effect of size-exclusion is generated by a term $(1 - \rho(x, t))$ in $\mathcal{T}$, see [200]. We visualized this in Figure 1.5a. For more complicated dynamics the so-called **Static Floor Field** (SFF) is embedded in the transition-rate $\mathcal{T}$. It indicates the probability of moving to a field for the agent to reach its goal. It therefore depends, for example, on the distance of the field to the exit Γ_E in evacuation scenarios. Accordingly, it is important whether a Moore or Von Neumann neighborhood is used, we illustrated therefore a SFF in 2D for the two different neighborhoods in Figure 1.5. On a microscopic level, we refer regarding SFF and multiple exits to [116].

While short-distance interactions are introduced in the transition-rate $\mathcal{T}$ via mentioned terms like size-exclusion, more sophisticated long-range interactions can be implemented via a **Dynamic-Floor-Field** (DFF). This makes the CA a kind of mixed-model and enables certain multi-scale approaches, see [58]. Motivated by the wide-spread macroscopic Keller-Segel-model (KSM), see [132], Kirchner et. al used the idea of chemotaxis to model interaction between pedestrians on a microscopic level via a DFF, see [136]. In the context of lane-formation side-stepping was introduced for cellular automatons, see [39]. A CA can reproduce the phenomena of lane-formation, see [174]. More complicated transition-rates $\mathcal{T}$ can, for example, introduce local and global pushing in spite of size-exclusion, see [10, 235].

Force-Based models

The previously mentioned collision-free granular models were compared with an anticipation model in [232]. The latter is a **force-based model**. In them we consider $N+1$ particle systems where the dynamics of each particle is driven by **Newton's laws of motion**. This results in first or second order ODE models. Let in the latter x_i, v_i denote position and velocity of agent i. Then the general form is

$$\begin{aligned} \frac{d}{dt}x_i(t) &= v_i(t), \\ \frac{d}{dt}v_i(t) &= F_i(\vec{x}(t), \vec{v}(t)), \end{aligned} \tag{1.3}$$

with $\vec{x}(t) = (x_0(t), \dots, x_N(t))$, $\vec{v}(t) = (v_0(t), \dots, v_N(t))$. Physically motivated from Coloumb's Law is the **Magnetic Force Model** (MFM) with F_i as the following

$$F_i(t) = \sum_j C q^i q^j \frac{x_i(t) - x_j(t)}{|x_i(t) - x_j(t)|^3}. \tag{1.4}$$

Here C is a constant and q^j can be interpreted as the charge of a pedestrian j at position x_i. Each pedestrian i, obstacles Γ_O and the boundary Γ_W are positive point sources and desired zones as e.g. the exit Γ_E negative. The previously mentioned phenomenon of lane-formation can be reproduced by this model, see [58, 212]. MFM allows overlapping of pedestrians, accordingly it does not fulfill the effect of size-exclusion. The effect of clogging also occurs in force-based models and is a current research topic at the microscopic level, see [233].

The most common force-based model is the so-called **social force model** (SFM), see [108, 112, 175, 212], with F_i as in the following

$$F_i(t) = F_{i,d} + \sum_{j \neq i} F^j_{i,r} + \sum_A F^A_{i,a} + \sum_O F^O_{i,o} + \eta_i.$$

Here $F_{i,d}$ corresponds to the desired velocity of agent i and $F_{i,r}$ represents the repulsive force due to other pedestrians. In some situations, agents group together, for example, due to friendship or in the context of a tourism group. This is modelled by $F_{i,a}$. The last term $F_{i,o}$ is a repulsive force due to obstacles Γ_O and the boundary Γ_W, which usually decreases exponentially fast. The factor η_i models some randomness. For more detailed modelling of the terms in F_i, we refer to [58], Chapter 4.1 or [112]. The SFM model reproduces the effect of Faster-is-Slower. While the individual parameters have a physical meaning, the SFM is not suitable for evacuation situations, see [212]. One disadvantage of ODE models is the oscillation of pedestrians that occurs in numerical simulations, making calibrations difficult as well, see [201]. From the mathematical side, an advantage is the existence and uniqueness of the solution of system (1.3), which can be deduced from Picard-Lindelöf's theorem.

Stochastic differential equations

Other microscopic modelling approaches in pedestrian dynamics that we briefly mention for the sake of completeness include those of **stochastic ODEs** (SDE). In the context of size-exclusion , see [32]. Hereby the evolution of agent i is given by

$$dx_i(t) = v_i(t)dt + \sqrt{2}dW_i(t). \tag{1.5}$$

Here v_i represents the optimal strategy for agent i, see also [190]. Volume exclusion effects can be included in a force f_i, e.g. $v_i = f_i(\vec{x})$, ensuring that the particles keep a certain distance to each other. whereby W_i represents randomness via independent Brownian motion, see Figure 1.6a.

The authors in [31, 32] analyse the so-called **overdamped Langevin** SDEs

$$dx_i(t) = -\nabla V(x_i)dt + \sqrt{2D}dW_i(t) \tag{1.6}$$

where V is an external potential and D a diffusion coefficient. The authors in [31, 190] investigated system (1.6) in the context of lane formation.

Other modelling approaches and comments

In context of size-exclusion the authors in [12] work with a lattice-based model, i.e. discrete in space and continuous in time.

Combining advantages of CA and ODEs, the **optimal-step model** has been introduced in [201]. It is described as combining the merits of a sequential update with simple size-exclusion rules, borrowed from CAs, but at the same time is continuous in space. It is continuous in space and sequentially updated, therefore discrete in time. In the context of infection models, parameters for the repulsion in social distancing-effects have been published, see [160].

In the context of the **COVID-19** pandemic, models related to the SFM were used as the basis for infection models, see [231]. Stochastic agent-based population models were also applied, which had already been developed before COVID, for example, in the context of influenza, see [22, 162]. For a broad overview of microscopic modelling, see [21].

Some of the previously mentioned modelling approaches like the Follow-the-Leader model are based on **traffic simulations**. In traffic simulations fast CAs are used to model real time situations. As previously mentioned a disadvantage of microscopic models is the required computation time when compared with macroscopic models. The authors in [13] present a CA which can simulate 600 vehicles at real-time frame-rates.

1.1.2 Biology

Occuring phenomena

In biology, many effects as e.g. the movement of cells as well as bacteria is modeled microscopically. Here one tries to explain the occurrence of macroscopic structures from microscopic rules of the single individuals similar to pedestrian dynamics. In general we call those phenomenons **emergence**. Self-organization or the emergence of structures occurs in many models, for example flocks of birds, schools of fish or the growth of tissue, see [164, 165].

One effect studied in experiments is the **aggregation** of bacteria. One biological cause of this is **chemotaxis**. Chemotaxis is a biological phenomenon in which cells or bacteria direct their velocity according to the distribution of chemicals in the environment.

Chemotaxis is a reason for **flocking**. Another phenomena believed to cause flocking is **alignment**. **Plithotaxis** can be mentioned as an example of current investigation. In collective cell migration, plithotaxis is the tendency of each individual cell within a monolayer to migrate along the local orientation of maximum principal stress. For a more biological introduction we refer to [219]. The phenomena of alignment leads to **collective motion** and **swarming**.

During the swarming process of bacteria the phenomenon of **rippling** was observed. Rippling is the occurrence of macroscopic propagating waves due aligned bacteria, see [119]. Colliding waves lead to the reversal of the orientation of bacteria as individual bacteria-tracking shows, see [195].

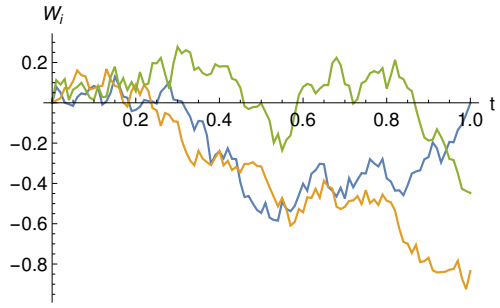

(a) Three evaluations of an independent Wiener Process W_i

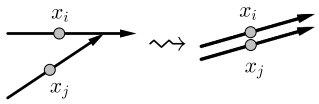

(b) Alignment of bacteria.

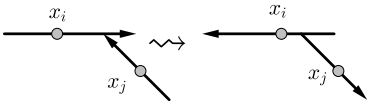

(c) Repulsion of bacteria.

Figure 1.6: On the left a Wiener process occurring in SDEs. It is a continuous in time stochastic process and has normally distributed, independent increases. It represents a mathematical model for Brownian motion, a form of random walk. On the right the two different interactions of colliding Myxobacteria in (1.10), (1.11).

The **pattern formation in bacteria** has also been studied in the context of size-exclusion, an effect already introduced in the context of pedestrians. Since bacteria motion - if surrounded by enough media - is passive, it means that bacteria only repulse each other to avoid overlapping as they grow in length and divide.

Force-based models for pattern-formations

From a mathematical point of view, the phenomenon plitothaxis was investigated numerically with a second order differential equation system in [184,230]. They work with a force-based model comparable to (1.3). Acting forces are the co-attraction, rotational turning, self-propulsion, contact, contact damping and contact repolarization forces.

Repulsion of bacteria and the associated pattern formation can result from size-exclusion. Doumic et al., see [66], work with steric forces as in (1.4) but also with asymmetric friction forces since bacteria are approximated by a spherocylinder described by its centre x_i. The authors therefore replace v_i by φ_i in a second order ODE-system. Here φ is the alignment angle. In this model the length l of bacteria growths exponentially till it splits into two agents. Similar approaches for x_i and φ_i when modelling the motion of bacteria based on over-damped molecular dynamics were used in [73, 236]. Again the dynamics in these works were investigated only numerically.

As already mentioned in the pedestrian dynamics, modelling on microscopic level is often not targeted for a scale change but exclusively for the reproduction of occurring phenomena. The models in [73, 184, 230, 236] are therefore not (yet) suitable for a change of scale. Their analysis often occurs via calibrating and then analysing the numerical simulations. We therefore continue this Section with a model that is 'as simple as possible, as complicated as necessary'.

The Vicsek-model

Perhaps the most famous example introduced in 1995 is the now-called **Vicsek-model**, see [224]. It reproduces **collective motion** and **swarming**. Originally formulated it is discrete in time and it, as being minimal, assumes that flocking results due a combination of **self-propulsion** and **alignment**. The model reads as the following,

$$\begin{aligned} x_i(t+\Delta t) &= x_i(t) + v\Delta t\,(\cos\varphi(t), \sin\varphi(t))\,, \\ \varphi_i(t+\Delta t) &= \langle\varphi_j\rangle_{|x_i-x_j|<r} + \eta_i(t). \end{aligned} \tag{1.7}$$

Here $\langle\varphi_j\rangle_{|x_i-x_j|<r}$ denotes the average position of angles of close agents and η represents uncertainty due to a noise. The system is controlled by the amplitude of η and the ratio between the travel distance v per time-step and the interaction radius r. Model (1.7) shows a **phase transition** from disordered motion to a large-scale ordered motion, see [97]. It was investigated and expanded with effects of **local cohesion** or **accounting the fluid** the particles are in, in [54]. Model (1.7) can be seen as the discretisation of a system of SDEs of the form (1.5). The time-continuous Vicsek model then is a system of stochastic differential equations modelling the collective motion of a swarm of agents.

The Keller-Segel model and chemotaxis

The **Keller-Segel** model (KSM) is one of the best known macroscopic models for bacteria and chemotaxis. We discuss it in Section 1.3. Similar to the heat equation, originally it was derived from macroscopic considerations only, see [82, 132, 172]. Nonetheless, there are microscopic models, related to the KSM via a change of scaling. This can serve both as an approximation of the solution, see [102], but can also be used to better understand the individual effects that occur. A microscopic version of KSM is e.g. given by the system of SDEs, similar to (1.6),

$$dx_i(t) = \frac{\xi}{N-1}\sum_{j\neq i}^{N} F\left(x_i(t) - x_j(t)\right) + \sqrt{2}dW_i(t), \tag{1.8}$$

see [115]. Here ξ is a scaling constant, F models the pairwise interaction between particles i and j and W_i represents again independent Brownian motion as in Figure 1.6a. System (1.8) reproduces aggregation due effects of chemotaxis.

Purposefully away from macroscopic modelling and as a contrast to the well-known Keller-Segel model, a system of SDEs was introduced in [192]. It can reproduce numerically macroscopic colony patterns and mesoscopic collective dynamics. The authors also discuss microscopic advantages over macroscopic models.

Molecular dynamics and Myxobacteria

In mathematical biology, the example of **Myxcobacteria** and pattern-formation due to alignment has also been studied intensively. These bacteria, similar to the previously discussed pedestrians, are a famous example of how interactions at the microscopic level lead to self-organization of the collective, see [113, 129]. What is interesting about this type of bacteria is that they need to touch each other for communication, see [129, 134]. Without going into biological details of this process a modelling from the mathematical side via an approach similar to colliding particles and the ideas of Boltzmann is natural, see [27].

We start with a 2nd-order ODE system similar to (1.3), where the dynamics are interrupted by instantaneous binary collisions. Collisions between particle i and j cause jumps in the velocity v_i, v_j which follow **invertible** collision rules. Now similar to the granular media models in the previous Subsection let K be the state space such that no overlapping between agents occurs. For this we introduce a probability distribution P, with $P((x_0, v_0), \dots, (x_N, v_N), t) \geq 0$. Deriving it with respect to time leads to a **Liouville equation**, see [128]:

$$\frac{d}{dt} P((x_0, v_0), \dots, (x_N, v_N), t) + \sum_{i=0}^{N} v_i \nabla_{x_i} P((x_1, v_1), \dots, (x_N, v_N), t) = 0.$$

In statistical mechanics a Liouville equation describes the time evolution of the phase space distribution function. It was first recognized by Josiah Willard Gibbs as the fundamental equation of statistical mechanics, see [92]. We denote with P_1 the first marginal of P. Assuming the particles-property of **indistinguishability** one can derive for the then one-particle distribution function P_1 the following equation:

$$\partial_t P_1(x, v, t) + v \nabla_x P_1(x, v, t) = Q(P_2). \tag{1.9}$$

Here now Q, depending on the two-particle distribution function P_2, denotes an integral over the boundary of K, where particles overlap due to a collision. It can be shown, that P_2 depends on pre-collision states (x, v) and also post-collision states denoted by (x^*, v^*),

$$\begin{aligned} x_i^* &= g_1(x_i, v_i, x_j, v_j), \quad v_i^* = g_2(x_i, v_i, x_j, v_j), \\ x_j^* &= g_1(x_j, v_j, x_i, v_i), \quad v_j^* = g_2(x_j, v_j, x_i, v_i). \end{aligned}$$

The dependence on pre- and post-collision states makes (1.9) non-closed. One approach is deriving an equation for P_2 depending on P_3 and so on. In continuing this approach one derives a completely coupled system known as the **BBGKY-hierarchy**, see [51]. Solving the BBGKY hierarchy of equations is highly non-trivial and similar to solving the original Liouville equation. However approximations for the BBGKY hierarchy can be made. One of those is the **Boltzmann-Grad** limit, see [50,96]. We sketch details in Section 1.2.

A good overview of the derivation and analysis of these models can be found in [51,183] and especially for Myxobacteria we refer to [128]. Here they have the two update-rules **alignment** and **reversal** of colliding bacteria depending on their angle of collision. We now consider exclusively bacteria with velocity $|v| = 1$ in 2D, then v is given by

$$v_i = (\cos \varphi_i, \sin \varphi_i).$$

We consider as before the system of ODEs

$$\begin{aligned} \frac{d}{dt} x_i &= v_i \\ \frac{d}{dt} \varphi_i &= 0. \end{aligned}$$

If two bacteria i and j collide, the direction of motion and position change depending on the angle of collision. In detail, the update rules are the following: for $\varphi_i \cdot \varphi_j > 0$, **alignment** occurs.

$$\begin{aligned} x_i^* &= \frac{x_i + x_j}{2}, \quad \varphi_i^* = \frac{\varphi_i + \varphi_j}{2}, \\ x_j^* &= \frac{x_i + x_j}{2}, \quad \varphi_j^* = \frac{\varphi_i + \varphi_j}{2}. \end{aligned} \tag{1.10}$$

In the case $\varphi_i \cdot \varphi_j < 0$, bacteria **repel** each other

$$\begin{aligned} x_i^* &= x_i, \quad \varphi_i^* = \varphi_i + \pi, \\ x_j^* &= x_j, \quad \varphi_j^* = \varphi_j + \pi. \end{aligned} \tag{1.11}$$

Collision-rules in (1.10) and (1.11) were modelled motivated by the observation of alignment and repulsion in [119, 195]. We visualized this in Figure 1.6b, 1.6c.

Of course, this approach is highly simplified. On the mathematical level, equation (1.10) has to be regularised, since the collision rules are otherwise not invertible. Non-micro-reversible processes were investigated in [78]. Spontaneous alignments after collisions do not correspond to reality, in [130] first insights into non-spontaneous collisions were investigated. For more details regarding microscopic models and the derivations of kinetic equations we refer on the references therein [51, 128, 178].

1.1.3 Economics and social sciences

Microscopic modelling has application in **economics**, for example, in the stock market, see [151, 196]. The long-term behavior of these models is difficult to predict. Kinetic theory has therefore not only been used successfully in the life sciences, but also in social sciences and economics. In this context collisions correspond to **trading events**, for example goods, opinions, and wealth, [8, 36, 56, 68, 72, 179]. Research on **opinion formation** and **wealth** is a current topic also in the context of the Covid-19 pandemic, see [20, 35].

The ELO rating system is one of the best known rating systems in the world - due to its widespread use in chess. Starting from the Bradley-Terry model - named after R. A. Bradley and M. E. Terry, see [1], who presented it in 1952, see [30], Arpad Elo developed an objective rating system for the US chess federation USCF in 1960. Its basic idea is that in the case of two objects i, j rated λ_i, λ_j, object i is preferred over j with probability $\frac{\lambda_i}{\lambda_i + \lambda_j}$. It was adopted by the world chess federation FIDE at the 1970 congress in Siegen. Elo himself checked his system only with statistical experiments, see [75].

In the context of rating-systems, the **desired emergent behavior** is, for example, the convergence of an agent's rating R against its strength ρ. In opinion formation an emergent behaviour is the alignment of opinions while in the study of wealth distributions an investigated phenomena is the occurrence of Pareto-distributions and their so called Pareto-tails which are introduced in the following.

Wealth distribution

In economics, much goes back to **Vilfredo Pareto**. Pareto studied the income and wealth of European and South American countries, starting in 1906 with the distribution of land ownership in Italy. He found that about 20% of the population owned about 80% of the land. This pattern occurred again and again, to quote him, '*it is a social law,* [...] *in the nature of man*', following [154]. Pareto distributions in the analysis of wealth distribution correspond to the studied phenomena of emergence that occur in biology. A Pareto-distribution has so-called **fat-tails**. Such overpopulated tails are a sign of the existence of an upper class of very rich agents. Therefore an unequal distribution of wealth exists, see [178]. A continuous random variable X is called Pareto distributed $\mathrm{Par}(\alpha, k)$ with parameters $\alpha > 0$ and $k > 0$ if it has probability density f as follows

$$f(x) = \begin{cases} \frac{\alpha x^k}{x^{\alpha+1}}, & x \geq k \\ 0, & x < k \end{cases}. \tag{1.12}$$

We visualized Pareto-distributions in Figure 1.7 for different parameters and in the limiting case $\alpha \to 0$.

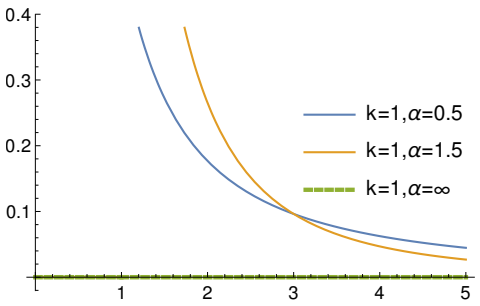

(a) The PDF defined in (1.12) and the limiting case $\alpha \to \infty$.

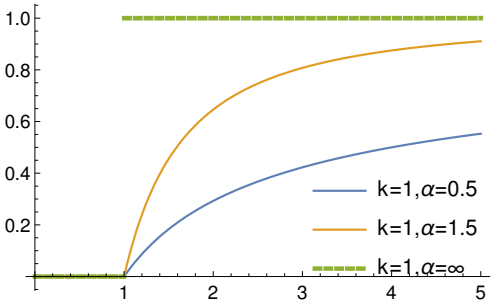

(b) The corresponding CDF.

Figure 1.7: Pareto-distributions and corresponding cumulative distribution function. For $\alpha \to \infty$ the distribution approaches $\delta(x-k)$.

We start with a simple example of economics, the so-called the **winner-takes-it-all**. That is, if two agents i, j with wealth x interact in the market, the winner gets all of it. It follows the **linear exchange rule**

$$\begin{aligned} x_i^* &= x_i + x_j, \\ x_j^* &= 0. \end{aligned} \tag{1.13}$$

This model is **conservative**. Conservative models have the property that the average wealth over time is conversed, that means

$$\frac{d}{dt} \sum_i x_i(t) = 0. \tag{1.14}$$

This idea is the basis for so-called **strictly conservative** exchange models according to [53], in which

$$x_i^* + x_j^* = x_i + x_j$$

holds. Therefore the total wealth in an individual trade stays preserved. This does not hold true for general linear exchange rules

$$\begin{aligned} x_i^* &= p_1 x_i + q_1 x_j, \\ x_j^* &= q_2 x_i + p_2 x_j, \end{aligned} \tag{1.15}$$

where e.g. a difference $(p_1 - q_2)x_i$ is a relative gain or loss of wealth due to market risks.

Microscopic simulations show an aggregation of wealth for model (1.13). This corresponds to the limiting case $\alpha \to \infty$, most wealth is aggregated with few agents. Because of its simplicity, we will revisit the winner-takes-it-all model later again. It can be fully analysed on the macroscopic level via an explicit solution of the corresponding model. For a broader overview of models of economics and stock markets, we refer the reader to [178].

Opinion formation

In **opinion dynamics** x_i corresponds to a continuous variable taking values in the interval $[-1, 1]$. Here the values ± 1 correspond to extreme opinions, e.g. left and right wing political opinions in

politics. The most prominent example was introduced in [214] by Toscani. It is of the following form:

$$\begin{aligned} x_i^* &= x_i - \gamma P(|x_i|)(x_i - x_j) + \eta_i D(|x_i|), \\ x_j^* &= x_j - \gamma P(|x_j|)(x_j - x_i) + \eta_j D(|x_j|), \end{aligned} \tag{1.16}$$

here P models the **local relevance** of compromise; the function D models the **local diffusion** of opinion. It is multiplied by a random variable η with mean 0 and variance σ^2. The compromise constant $\gamma \in (0, 1/2)$ is fixed. One idea modelled in (1.16) is, that extreme options, e.g. $|x|$ close to 1, are difficult to change. Therefore D and P are non-increasing. As a simple case, let us assume that $P = 1$. Then the **total mass** and **momentum** is conserved. The expected outcome of the sum and difference of opinion is given by

$$\begin{aligned} \langle x_i^* + x_j^* \rangle &= 0, \\ \langle x_i^* - x_j^* \rangle &= (1 - 2\gamma)(x_i - x_j). \end{aligned}$$

This confirms that (1.16) is indeed mass conserving. Since $\gamma \in (0, 1/2)$ we see that (1.16) is therefore leading to compromise. EAlready on the microscopic level one can make statements about the long-term behavior for simple models. Alignment of the opinion occurs through averaging of opinions.

Elo

Originally proposed by Elo the binary update rule between players i and j is given by

$$\begin{aligned} R_i^* &= R_i + \gamma(S_{ij} - b(R_i - R_j)), \\ R_j^* &= R_j + \gamma(-S_{ij} - b(R_j - R_i)). \end{aligned} \tag{1.17}$$

Here $S_{ij} \in \{-1, 1\}$ represents the outcome of the game between the players. In the simplest case $S_{ij} \in \{-1, 1\}$ for **win** respective **lose**. The rating of players are represented by R_i, R_j before, and R_i^*, R_j^* after the match. The constant γ is the rate at which ratings are adjusted and usually small compared to R. The function b is bounded and odd. Therefore we have a conservative model, that is

$$R_i^* + R_j^* = R_i + R_j.$$

Here we have ruled out the possibility for a draw. However, as discussed in [121, 141], S_{ij} can even be extended to a metric variable, for example $[-1, 1]$. Not specified in the update rule is the underlying player strength ρ_i, ρ_j. From mathematical considerations the authors in [121] motivate that S_{ij} depends only on this inner playing strength ρ_i, ρ_j, that is

$$\langle S_{ij} \rangle = b(\rho_i - \rho_j).$$

Rating systems are also designed to allow players with similar strength to play against each other with a higher probability. We are introducing a weighting function w for this purpose, here $w(R_i - R_j)$ gives the probability, that i plays against j. This can be seen as the probability of collision via Q in (1.9). If w is chosen constant, everyone happens to play everyone, other choices are e.g.

$$w(R_i - R_j) = (\epsilon - (R_i - R_j))_+, \tag{1.18}$$

therefore players only play against each other when their difference in rating is less than ϵ. Another possibility for w would be a Gaussian.

The first extension of this model was proposed by Krupp in a master thesis, see [141]. She introduced a model where, additionally to (1.17), the initial strength ρ changes according to

$$\begin{aligned} \rho_i^* &= \rho_i + Z_{ij}\tilde{\gamma}, \\ \rho_j^* &= \rho_j + Z_{ji}\tilde{\gamma}, \end{aligned} \tag{1.19}$$

after every game due to the effect of learning. Here $\tilde{\gamma}$ is again a positive constant regulating the rate of learning. The random variable Z_{ij} depends on the outcome S_{ij} and takes values $z_l, z_w \in \mathbb{N}$ depending if the player wins or looses. Therefore your strength increases by $z_{l,w}\tilde{\gamma}$ but always increases. It is a model with linear learning and not conservative in the strength ρ.

A more advanced model was introduced in [71], Wolfram et al. have generalized this approach and introduced a microscopic model where players can learn. The learning effect depends on the strength of the opponent and also underlies fluctuation. They modelled microscopically the following increase in strength

$$\begin{aligned} \rho_i^* &= \rho_i + \gamma h(\rho_j - \rho_i) + \eta_i, \\ \rho_j^* &= \rho_j + \gamma h(\rho_i - \rho_j) + \eta_j. \end{aligned} \tag{1.20}$$

where they have a non-linear learning-function h. It can be split into two components h_1 and h_2. Here h_1 models learning, while h_2 models the loss of confidence due defeats. Additionally there is a factor of randomness via η. Those variables are independent identically distributed (iid.) random variables with mean zero and variance σ which model small fluctuations due to day-linked performance in the mental strength or personal fitness. We refer to Section 1.2 and 1.3 where we discuss the derivation of the corresponding kinetic PDEs and the energy-methods used in its analysis.

Other modelling approaches

Many of the previously presented models serve, in the spirit of this thesis, as a starting point for the derivation of a macroscopic or kinetic model. While the microscopic description allows for a detailed modelling, kinetic and macroscopic models are mathematically amendable. Starting with the goal of moving to a PDE, one often has to enter a trade-off already at the microscopic level with complexity and richness of detail.

Independent of macroscopic mathematics, however, microscopic modelling is found in a variety of fields as mentioned above. We now mention a few more of them.

1.2 From micro- to meso- and macroscopic models

The change of scale from microscopic to macroscopic or mesoscopic level varies depending on the microscopic model. We present briefly some approaches related to later Chapters 2-4. We start with the Boltzmann-Grad limit in the previously mentioned microscopic model in the context of mycobacteria. We obtain a kinetic model as a result. In the context of kinetics, we also list the derived PDEs in the context of the Elo-rating. Using this approach, the investigated model in Chapter 3 was derived. Afterwards we derive the heat-equation formally from a 1D-random walk discrete in time t and space x. This approach serves as an introduction to the derivation of the models that have been carried out in Chapter 2. In preparation for Chapter 4 we therefore also discuss a rigorous limit on a simple periodic problem in 1D. If a rigorous limit is possible, existence results can be transferred from the microscopic scale.

1.2.1 The Boltzmann-Grad limit, deriving a kinetic PDE

We continue how to derive a mesoscopic PDE from the one-particle distribution function, that is (1.9), and let the number of particles go to infinity, $N \to \infty$. At the same time we let the size of the particles go towards 0. Here we let the ratio between the interaction range and the so-called mean free path length (average distance between collisions) remain constant. For the derivation we also need the assumption of **molecular chaos**. This goes back to Maxwell, see [159]. It states that the probability of two particles i and j with given velocities v_i and v_j colliding can be calculated by considering each particle separately. Therefore the velocities of colliding particles are uncorrelated, and independent of position x_i, x_j. Historically we need to mention this leads to Boltzmann's **H-theorem** of 1872, see [28]. Biologically the assumption to neglect correlations between bacteria can be made but in order to show a rigorous limit one has to prove **propagation of chaos**, see [143]. In the context of the Elo-rating, this is a strong simplification. The collision, i.e. the match between two agents, is in general not uncorrelated but depends on the ratings R_i, R_j of the players and is determined by the function w defined in (1.18). For more technical details we refer to [51]. We now perform the formal limit.

We assume that

$$P_1(x_i, v_i, t) \to f(x_i, v_i, t), \qquad P_2(x_i, v_i, x_j, v_j, t) \to f(x_i, v_i, t) f(x_j, v_j, t),$$

This refers to the **indistinguishability** of particles, that means interchanging two individuals i, j, does not effect the dynamics of the system. Then the corresponding kinetic PDE is given by

$$\partial_t f + v \nabla_x f = Q(f, f) \tag{1.21}$$

since the choice of the particle's index, with respect to which we defined the first marginal P_1, is independent. Equation (1.21) states the evolution of the expected particle density function $f(x, v, t)$. The left-hand side describes transport where the right-hand side accounts for interactions between particles. In the following we will describe different kinetic equations with a focus on Q.

We recall that the dynamics of myxobacteria are driven by collision and their angles in pre-collision, leading to alignment or repulsion. This results in a collision operator Q which is the sum of three integral operators. The authors in [113] derive then the following operators:

$$\begin{aligned} Q(f,f) =& 2 \int_{\mathrm{Al}} \left|\sin\left((2\varphi - \varphi') - \varphi'\right)\right| f(x, 2\varphi - \varphi', t) f(x, \varphi', t) d\varphi' \\ &+ \int_{\mathrm{Re}} \left|\sin\left(\varphi - \varphi'\right)\right| f(x, \varphi + \pi, t) f(x, \varphi' + \pi, t) d\varphi' \\ &- \int_{\mathbb{T}} \left|\sin\left(\varphi - \varphi'\right)\right| f(x, \varphi, t) f(x, \varphi', t) d\varphi'. \end{aligned}$$

Here the first integral-operator is a **gain-term** due alignment of two bacteria. They integrate over $\mathrm{Al} = (\varphi - \frac{\pi}{4}, \varphi + \frac{\pi}{4})$, based on (1.10). The second operator is also a **gain-term** due to collision of bacteria and reverting itself to (x, φ), see (1.11). Therefore they integrate over $\mathrm{Re} = (\varphi + \frac{\pi}{2}, \varphi + \frac{3\pi}{2})$. The third integral-operator is a **loss-term**, it represents bacteria colliding or aligning with any other bacteria, therefore integrating over the torus $\mathbb{T}$.

In the context of the Elo-rating, the authors in [121] derived the following kinetic equation

$$\begin{aligned} &\partial_t f(t, \rho, r) = Q(f, f) \\ &\text{with } Q(f,f) = -\partial_r \left(f(r, t, \rho) \int_{\mathbb{R}^2} w(r - r')(b(\rho - \rho') - b(r - r')) f(t, r', \rho') d\rho' dr' \right). \end{aligned} \tag{1.22}$$

Here r and ρ represent rating and strength of players. The function w, as noted before, gives the probability that players with ratings r and r' play against each other. The Elo-rating can be seen as a model without a transport term v, since players who do not play do not change their rating. In the operator Q, gain and loss terms are implemented. The collision corresponds to a match between two players, it leads to a change in rating r, r'.

The linear learning effect was introduced in the work of [141]. This leads to the linear Fokker-Planck equation

$$\begin{aligned}\partial_t f(t,\rho,r) =& Q(f,f)\\ \text{with } Q(f,f) =& -\partial_r\left(f(r,t,\rho)\int_{\mathbb{R}^2} w(r-r')[b(\rho-\rho')-b(r-r')]f(t,\rho',r')d\rho'dr'\right)\\ &-\partial_\rho\left(f(t,\rho,r)\int_{\mathbb{R}^2} w(r-r')[\frac{z_l}{2}(b(\rho-\rho')+1)-\frac{z_w}{2}(b(\rho-\rho')-1)]f(t,\rho',r')d\rho'dr'\right)\end{aligned}$$

based on the microscopic interaction rules (1.19). The extension made by the authors in [71] via (1.20) leads to the following Focker-Planck equation

$$\begin{aligned}\partial_t f(r,\rho,t) =& Q(f,f)\\ \text{with } Q(f,f) =& -\partial_r\left(f(r,t,\rho)\int_{\mathbb{R}^2} w(r-r')[b(\rho-\rho')-b(r-r')]f(t,\rho',r')d\rho'dr'\right)\\ &-\partial_\rho\left(f(t,\rho,r)\int_{\mathbb{R}^2} w(r-r')(\alpha h_1(\rho'-\rho)+\beta h_2(\rho'-\rho))f(\rho',r',t)\,d\rho'dr'\right)\\ &+\frac{\sigma^2}{2}\int_{\mathbb{R}^2} w(r-r')f(\rho',r',t)\,d\rho'dr'\partial_{\rho\rho}f(r,\rho,t).\end{aligned} \tag{1.23}$$

We would like to note for the reader that the derivations of the kinetic PDEs vary technically due to microscopic considerations and the approach presented here corresponds to [71].

1.2.2 From cellular automatons to PDEs

As a simple example we consider a stochastic random walk in 1D without size-exclusion. It is a model discrete in space x and time t with grid-size Δx and time-step Δt. Let ρ denote the probability of finding a particle at position x at time-point t. The evolution of ρ is then determined by the following difference-equation, the so-called master equation:

$$\rho(x,t+\Delta t)-\rho(x,t) = -2\mathcal{T}\rho(x,t)+\mathcal{T}\rho(x+\Delta x,t)+\mathcal{T}\rho(x-\Delta x,t). \tag{1.24}$$

Here $\mathcal{T}$ is the constant jump probability. If one formally assumes that ρ has sufficient regularity, one can replace ρ with its Taylor series,

$$\begin{aligned}\rho(x,t+\Delta t) &= \rho(x,t)+\Delta t\frac{d}{dt}\rho(x,t)+\mathcal{O}(\Delta t)^2\\ \rho(x,t\pm\Delta x) &= \rho(x,t)\pm\Delta x\frac{d}{dx}\rho(x,t)+\frac{1}{2}(\Delta x)^2\frac{d}{dx}^2\rho(x,t)+\mathcal{O}(\Delta x)^3\end{aligned}$$

Replacing these terms in (1.24) and assuming $\frac{\Delta t}{(\Delta x)^2}=const.$, we obtain as $\Delta t\to 0$:

$$\partial_t\rho(x,t)=\mathcal{T}\partial_x^2\rho(x,t). \tag{1.25}$$

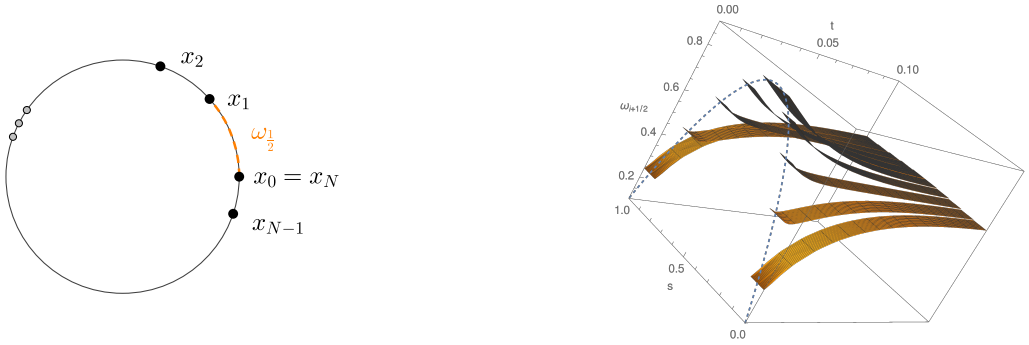

(a) We work with periodic boundary conditions in model (1.26), this can be seen as N agents x_i repelling each other on a circle.

(b) The piecewise defined ω^N visualized. Dashed can be seen the continuous initial data ω_0 and the evolution of the discretization $\omega^N(s,t)$ for $N = 10$.

Figure 1.8: Visualization of the context in the rigorous limit.

The ratio of Δx and Δt determines the different scaling limits leads to different PDE models. The previous ratio corresponds to a so-called **parabolic limit**. If $\Delta t = \Delta x$ the so called **hyperbolic limit** leads to a hyperbolic PDE. Examples for macroscopic models derived this way can be found in [38, 39, 200, 207]. Also the models in Chapter 2 are derived this way. Assuming more complicated master-equations lead to lengthy calculations. This approach can be supported by a CAS-system as discussed in [138].

1.2.3 A rigorous limit from ODEs to a PDE

The formal derivation from macroscopic to microscopic models is not always trivial. Properties of the system at the microscopic level cannot be transferred to the PDE level in a formal limit either. However, in the case of a rigorous limit, this is possible. In the following, we show in the case of a simplified problem how the existence of a solution on the microscopic level can be transferred to the macroscopic level.

For this purpose, we consider a periodic system similar to the FTL-model (1.2) with N agents, a system of ODEs. For reasons of simplicity we choose periodic boundary conditions $x_0 = x_N$, therefore the agents can be seen as particles on a circle as visualized in Figure 1.8a. The particle x_i is moved to the left depending on the distance of x_i to the right particle x_{i+1}, respective to the right depending on x_{i-1}. The function θ controls the repulsion depending on the distance $x_{i+1} - x_i$. The model then reads

$$\begin{aligned} \frac{d}{dt}x_i(t) &= \left(-\theta\left(x_{i+1}(t) - x_i(t)\right) + \theta\left(x_i(t) - x_{i-1}(t)\right)\right), \quad 1 \le i \le N-1, \\ \frac{d}{dt}x_0(t) &= \frac{d}{dt}x_N(t) = \left(-\theta\left(x_1(t) - x_0(t)\right) + \theta\left(x_0(t) - x_N(t)\right)\right), \end{aligned} \tag{1.26}$$

it can be seen as a repulsion-model. Furthermore in the following, all appearing test functions have sufficient regularity to omit technical difficulties. Introducing again $\omega_{i+\frac{1}{2}} = \frac{x_{i+1}-x_i}{\Delta s}$ for $i = 0, \dots, N-1$, Δs being the intrinsic length on our Lagrangian grid, this results in

$$\frac{d}{dt}\omega_{i+\frac{1}{2}}(t) = \frac{1}{\Delta s}\left(\theta(\omega_{i+\frac{3}{2}}(t)) - 2\theta(\omega_{i+\frac{1}{2}}(t)) + \theta(\omega_{i-\frac{1}{2}}(t))\right), \quad 0 \le i \le N-1. \tag{1.27}$$

Now, in the simplest case, we assume that θ is directly proportional to $\omega_{i+\frac{1}{2}}$, so $\theta(z) = \frac{\mathcal{T}}{\Delta s} z$, with $\mathcal{T}$ being the repulsive constant. This changes (1.27) to

$$\frac{d}{dt}\omega_{i+\frac{1}{2}}(t) = \frac{\mathcal{T}}{\Delta s^2}\left(\omega_{i+\frac{3}{2}}(t) - 2\omega_{i+\frac{1}{2}}(t) + \omega_{i-\frac{1}{2}}(t)\right), \quad 0 \le i \le N-1. \tag{1.28}$$

Existence and uniqueness for a finite time T of system (1.27) follows from Picard-Lindelöf. We assume that the number N of agents and Δs are directly proportional, i.e. $N\Delta s = 1$ holds. Formally for $\Delta s \to 0$ resp. $N \to \infty$ equation (1.28) converges to the heat-equation (1.25).

Before we can now proceed with a rigorous limit, we need to consider the weak formulation of the system. Let $\bigcup_0^{N-1}[s_i, s_{i+1})$ be a partition of $[0,1]$ in N equilateral intervals of width Δs. Let therefore $\varphi : [0,1]\times[0,T] \to \mathbb{R}$ be a suitable test-function and φ^N its discretization and let us define the sequence $\{\omega^N(s,t)\}_N$, $s \in [0,1]$, $t \in \mathbb{R}_+$ as

$$\omega^N(s,t) := \sum_{i=0}^{N-1} \omega_{i+\frac{1}{2}}(t) 1_{[s_i, s_{i+1})}(s),$$
$$\varphi^N(s,t) := \sum_{i=0}^{N-1} \varphi_i(t) 1_{[s_i, s_{i+1})}(s).$$

This discretization can be viewed geometrically as a section-by-section alignment of the trajectories of the microscopic system. We visualized this in Figure 1.8b. We denote in the following the discrete weak formulation in s and t,

$$\begin{aligned}\int_0^T \Delta s \sum_{i=0}^{N-1} \dot{\omega}_{i+\frac{1}{2}}\varphi_i dt &= \int_0^T \Delta s \sum_{i=0}^{N-1} \frac{\mathcal{T}}{\Delta s^2}\left(\omega_{i+\frac{3}{2}}(t) - 2\omega_{i+\frac{1}{2}}(t) + \omega_{i-\frac{1}{2}}(t)\right)\varphi_i dt \\ &= \mathcal{T}\int_0^T \Delta s \sum_{i=0}^{N-1} \frac{\varphi_{i-1} - 2\varphi_i + \varphi_{i+1}}{\Delta s^2}\omega_{i+\frac{1}{2}}(t) dt.\end{aligned}$$

Here we omit the dependence of φ on t and have only rearranged within the sum. It is straight-forward to show a Min-Max-principle for (1.27) and obtain boundedness of ω^N for bounded initial data ω_0. Those bounds on ω^N let us conclude that for all $T > 0$ there exists a subsequence, again denoted by $\{\omega^N\}_N$, and $\omega \in L^1([0,1]\times[0,T])$ such that

$$\omega^N \rightharpoonup \omega, \quad \text{as } N \to \infty \text{ in } L^1([0,1]\times[0,T]), \quad \text{for all} \quad T > 0.$$

Integrating now on the left-hand side with respect to time allows us to pass to the limit

$$\begin{aligned}-\int_0^1\int_0^T \omega^N(s,t)\dot{\varphi}^N(s,t)dt + \omega^N(s,T)\varphi^N(s,T) - \omega^N(s,0)\varphi^N(s,0)ds \\ \to -\int_0^1\int_0^T \omega(s,t)\dot{\varphi}(s,t)dtds - \int_0^1 \omega(s,0)\varphi(s,0)ds.\end{aligned}$$

Here we assumed φ vanishes at time T. Similar calculations hold for the right-hand side and we get in the limit, that a subsequence of ω^N converges against a solution of the equation

$$\int_0^1\int_0^T \omega(s,t)\dot{\varphi}(s,t)dtds - \int_0^1 \omega(s,0)\varphi(s,0)ds = \mathcal{T}\int_0^T\int_0^1 \partial_s^2\varphi(s,t)\omega(s,t)dsdt.$$

This is the weak formulation of

$$\partial_t\omega(s,t) = \mathcal{T}\partial_s^2\omega(s,t) \tag{1.29}$$

with periodic boundary-conditions. We can conclude that (1.29) has a weak solution in L^1. Of course, much stronger regularity results exist for the heat conduction equation, see e.g. [46, 77].

1.2.4 Comments

The limit in our example could be performed without technical difficulties because of the linearity of problem (1.28).

The formal derivation presented in Subsection 1.2.2 in the context of size-exclusion was generalized for a multispecies-system in [200]. For the effect of side-stepping a 2-species system of conservation laws was similarly derived in [39]. It is of the form

$$\partial_t \begin{pmatrix} r \\ b \end{pmatrix} = \operatorname{div} \left(D(r,b) \nabla \begin{pmatrix} r \\ b \end{pmatrix} - \nabla V(r,b) \begin{pmatrix} r \\ b \end{pmatrix} \right) \tag{1.30}$$

where $\rho = r + b$ represent the different populations depending on their directions V_b and V_r which are incorporated in V.

Many other limiting processes have been developed. A Boltzmann model in [217] was derived from an FTL-model similar to (1.2). For an overview in the context of the Boltzman equation, we mention the works in [63]. For an introduction to a probabilistic approach in transport processes, we refer to [177].

The presented derivations of the presented Boltzman-Grad limit or derivation of the heat equation are purely **formal limits**. This is the case in many models, often derivations of partial differential equations are only formal. Formal derivations are then compared numerically on microscopic and macroscopic level to see alignment on both scales, see [10, 95, 235]. A numerical comparison between microscopic and macroscopic level is also done in Chapter 3.

A limit **from SDE to PDE** in the briefly mentioned equation (1.6) corresponds to a probability density ρ for one particle being at position x at time-point t. It can be derived using the Ito-formula following [89]. It is of Fokker-Planck-type:

$$\partial_t \rho(x,t) = \operatorname{div} \left(v(x)\rho(x,t) + \nabla(D(\rho(x,t))) \right). \tag{1.31}$$

We now see the following. For a single agent, the probabilistic description at the particle level corresponds exactly to the description of a population at the continuum level. This is not the case for a larger number of particles, which is why additional assumptions about the correlations between the particles must be made in order to derive a low-dimensional PDE. To state one example for models with size-exclusion, the method of matched asymptotics was proposed in [32, 33] and applied in [31].

Boundary conditions on a PDE-level can also be derived via the previous techniques. An overview of how the heat equation with Robin-boundary conditions is derived from four different microscopic models can be found in [76]. We will state some results briefly in the next Section 1.4.

In particular, we see in the context of the three models presented on the Elo-rating only the random process in (1.20) led to a **diffusion** in (1.23). We also want to note the interesting fact, that for different microscopic models, the random walk in (1.24) and the repulsion in (1.26) lead to the same linear diffusion term on the PDE level.

1.3 PDE-Scale

1.3.1 Conservation Laws

In the following we state some typical features of the derived models. Let us first recall the microscopic models. All models have a constant number of agents over time. On a macroscopic level, this means that the derived models should satisfy the **mass conservation principle**. In detail a conservation

law is of the form

$$\partial_t \rho + \operatorname{div} \cdot (\rho v(\rho)) = 0. \tag{1.32}$$

Here $\rho = \rho(x,t)$ is the **particle density** as before and v is a **velocity field**. More general the velocity field v can often be written as

$$v = \nabla(U'(\rho) + V + W * \rho),$$

where U is an **internal energy**, V is an **external** potential, and W is an **interaction-potential**. We already introduced the Eikonal-equation in (1.1) as a possible choice for an external potential in the context of pedestrian dynamics. Thus we rewrite (1.32) as

$$\partial_t \rho + \operatorname{div} \cdot \big(\rho \nabla(U'(\rho) + V + W * \rho)\big) = 0.$$

Setting $V = W = 0$ and $U(\rho) = \rho \log \rho$ results in

$$\partial_t \rho = \partial_x^2 \rho.$$

Therefore the heat equation is a so called **conservation law** which, of course, corresponds to the physical concept of **conservation of energy**.

We see this property also immediately for model (1.31). Here D is diffusion caused by the internal energy and $v = \nabla V$ corresponds to the drift term. In the context of lane-formation equation (1.30) represents a two dimensional drift-diffusion PDE with drift ∇V and diffusion D. This PDE can be seen as a cross-diffusion system. For analytical and numerical approaches of those systems we refer to [31, 38, 127, 148]

Including the effect of size-exclusion, in [200] the authors derived a multi-species conservation law in $\rho = (\rho_1, \dots, \rho_n)$ of the following form

$$\partial_t \rho + \operatorname{div} \cdot (\nabla \rho + (1 - \rho)\rho \nabla V)) = 0.$$

Here on the macroscopic level the effect of size-exclusion leads to degenerate mobilities as the density approaches the maximum density 1.

Conservation of mass can also be shown for the kinetic model (1.21), the model of myxobacteria, after a short calculation. For this one has to introduce via

$$\rho(x,t) := \int_{\mathbb{T}} f(x,\varphi,t) d\varphi, \qquad \rho v := \int_{\mathbb{T}} v(\varphi) f(x,\varphi,t) d\varphi$$

the number of bacteria and the flux.

A formal calculation for the Elo model (1.22) results in

$$\partial_t \int_{\mathbb{R}^2} f(r,\rho,t) dr d\rho = 0.$$

In this case, this means that the number of players remains constant over time. The operator Q in (1.22) can be rewritten as

$$\begin{aligned} Q(f,f) &= -\partial_r (f a[f]), \\ a[f] &= \int_{\mathbb{R}^2} w(r-r')(b(\rho-\rho') - b(r-r')) f(t,r',\rho') d\rho' dr' \end{aligned}$$

Therefore (1.22) can be written in the form of (1.32) with the operator a corresponding to a velocity field.

All presented models in later Chapters 2-4 are conservation laws. No new agents are created on the microscopic level. Conservation of mass is therefore a phenomena, which is supposed to be fulfilled on all scales. Accordingly, in the previous mentioned context of bacterial growth in [66], this is not the case.

1.3.2 Coupled systems

The Keller-Segel model (KSM) is one of the most widely used models of a coupled drift-diffusion PDE for chemotaxis, originally introduced in [132]. It reads as follows

$$\begin{aligned}\partial_t \rho &= \operatorname{div}(\nabla \rho - \rho \nabla c)\\ \epsilon \partial_t c &= \Delta c - \beta c + \rho^\alpha.\end{aligned}$$

In this model, the chemical c affects the drift of the bacteria ρ. At the same time, bacteria ρ and the chemical c diffuse linearly. The chemical decays with constant β. It is produced by bacteria via ρ^α. Linear and nonlinear diffusion D and the influence on volume filling effects, i.e. size-exclusion, for the KSM has been studied for example in [37]. A review of the KSM can be found in [15]. The author in [148] discusses continuous and discrete structure-preserving approximation of chemotaxis and cross-diffusion systems, also the KSM. We will revisit the idea of chemotaxis in the applications in Section 1.4 in the context of pedestrian dynamics.

The previously mentioned Eikonal-equation (1.1) can be embedded in a coupled model. Hughes proposed in [117] a macroscopic approach via the following, now so-called coupled **Hughes-model**:

$$\begin{aligned}\partial_t \rho &= \operatorname{div}\left(\rho f^2(\rho) \nabla V\right),\\ \rho(x,0) &= \rho_0(x),\\ |\nabla V| &= \frac{1}{f(\rho)},\\ V(x) &= 0, \quad \text{on } x \text{ in } \Gamma_E.\end{aligned} \tag{1.33}$$

A microscopic derivation for the coupled eikonal-equation can be found in [157], Chapter 8.2. A common choice for f is $f = 1 - \rho$. However for $\rho \to 1$ this leads to analytical challenges. In 1D this problem was regularised and analysed in [65]. An approach for a regularisation of (1.33) in $\mathbb{R}^2$ is also topic in [111] in the context of optimal control.

1.4 Applications

In the following, we mention applications of a change of scale. We would like to emphasize that benefits of switching scales can occur in both directions, i.e. also from the PDE level to microscopic models. We start with an example of this kind.

1.4.1 New effects on different scales

Motivated by the effect of chemotaxis at the macroscopic level in the KSM, the authors in [43, 137] introduced a **dynamic floor field** V (DFF). It is a virtual trace left by the pedestrians. On a microscopic scale it is governed by the following macroscopic equation

$$\partial_t V = D \Delta V - dV$$

which is discretized in a standard manner. Here D is the diffusion coefficient and d the decay constant.

When working on bounded domains Ω, typical boundary conditions are often imposed on PDEs. Often they can be derived from microscopic models, see [42, 76]. Conservation laws for pedestrian dynamics in evacuation scenarios have so-called **No-Flux** boundary conditions along the wall Γ_W of the domain Ω. Let j be the flux in an abbreviated model

$$\partial_t \rho + \operatorname{div}(\mathbf{j}(\rho)) = 0,$$

then typical derived boundary conditions are given via

$$\begin{aligned} \mathbf{j} \cdot \mathbf{n} &= 0, \quad \text{on } \Gamma_W, \\ \mathbf{j} \cdot \mathbf{n} &= a\rho, \quad \text{on } \Gamma_E. \end{aligned}$$

Here a is a constant, controlling the linear outflow, see [42]. From microscopic considerations an increasing **non-linear outflow** in the context of pushing was presented in [79],

$$\mathbf{j} \cdot \mathbf{n} = a\rho(1 + \mu\rho), \quad \text{on } \Gamma_E.$$

The outflow increases since pedestrians are pushed out of the corridor with a constant μ governing the motivation to push.

In [185] the homogeneous Laplace equation was proposed as an **alternative potential**. This macroscopically motivated potential is a linear problem, consequently has advantages in terms of computation time. It also has, in general, a higher regularity than the solution of the Eikonal-equation.

1.4.2 Analysis, energy methods and long-term behaviour

At the microscopic level, the validity of the Elo ranking was tested by its inventor using statistical methods, see [75]. This method is common in the context of microscopic systems, see [178]. Stochastic fluctuations are averaged out with Monte Carlo repetitions. However, this method allows the relationship between parameters and, for example, the long-time behaviour in a simulation to be proven only empirically. Analytical methods at the macroscopic level can provide information about the long-time behaviour. As an example the authors in [42] analyse the **existence of equilibria** depending on inflow and outflow parameters in the hyperbolic limit for pedestrian models.

In the context of the Elo-rating the authors in [121] introduced the **relative energy**

$$\mathcal{E}(t) = \int_{\mathbb{R}^2} (r - \rho)^2 f(t, \rho, r)\, dr d\rho$$

and showed $\frac{d\mathcal{E}(t)}{dt} < 0$ via a formal calculation, using the short hand notation $f' = f(t, \rho', r')$:

$$\begin{aligned} \frac{d}{dt} \int_{\mathbb{R}^2} (r - \rho)^2 f \, d\rho dr &= - \int_{\mathbb{R}^2} (r - \rho)^2 \frac{d}{dr} (a[f]f)\, d\rho dr d\rho' dr' \\ &= - \int_{\mathbb{R}^4} (r - r') b(r - r') w(r - r') f f' \, d\rho' dr' d\rho dr \\ &\quad - \int_{\mathbb{R}^4} (\rho - \rho') b(\rho - \rho') w(r - r') f f' \, d\rho' dr' d\rho dr < 0. \end{aligned}$$

For $r - r' < 0$ we have $b(r - r') < 0$, while the opposite holds true for $r - r' > 0$. The same applies to ρ. With this energy decay, they were able to show the exponentially fast convergence of the rating r against the strength ρ, but only when w is strictly positive. Thus in some kind they **proved** the **functionality** of the Elo-rating via macroscopic methods on the one hand and underlined the **importance** of the **interaction function** w on the other hand. We visualized alignment of the two scales and convergence in Figure 1.9.

In the context of economics we mentioned on a microscopic level conservation of wealth in (1.14). On a macroscopic level this results in

$$\frac{d}{dt} \int_{\mathbb{R}^+} x f(x, t) dx = 0.$$

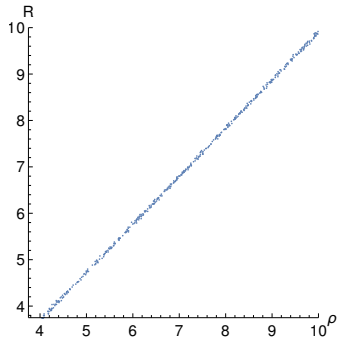

(a) Microscopic dynamics for $N = 200$ agents based on direct Monte Carlo simulation using Bird's scheme, see [178]

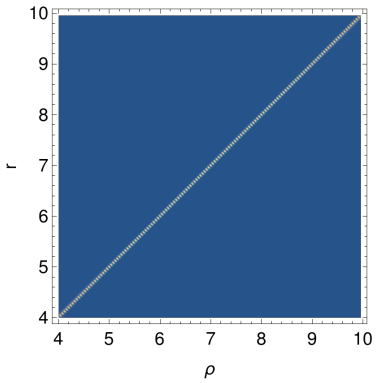

(b) Macroscopic dynamics, the convergence of (1.22) against the diagonal was proven analytically in [121].

Figure 1.9: The microscopic and macroscopic scales align.

One can use the Fourier-transformation for the kinetic model of aforementioned winner-takes-it-all-model (1.13) to derive its explicit solution. It can be used to show that the relative proportion of agents with wealth 0 actually approaches 1, see [178]. Mathematically spoken it is a Dirac delta centred at 0. As mentioned before, a possible question in this field would be if a (microscopic) interaction model has a Pareto distribution as a solution. Pareschi et al. showed in [178] existence and tails of steady states of the corresponding kinetic models for general p, q in the case of linear exchange rules (1.15) in conservative economic models.

In current research, starting from well-known Pareto tails in socio-economic phenomena, kinetic theory is also used to link back to microscopic relationships, as an example, the distribution of populations in towns is discussed in [98].

Due to the strong existence- and uniqueness-theory at the microscopic level resulting from Picard-Lindelöf, for many ODE systems similar to (1.3) with right-hand side being Lipschitz regularity-statements can be made. In performing a rigorous limit those results can be transferred to the macroscopic scale. **Rigorous limits** of this kind have been extensively treated for e.g. the KSM, via propagation of chaos for $N \to \infty$, see [102]. For reviews of the topic on mean field limits we refer to the works [47,122]. For e.g. the continuous version of the Vicsek-model (1.7) a rigorous limit to a PDE was performed in [26] transferring regularity results to the macroscopic level. Therefore mentioned rigorous limits from microscopic to macroscopic scales can serve to extend the theory of existence of solutions at the PDE level, see [64].

1.4.3 Numerical advantages

In previous Subsection 1.4.2 we visualised the alignment between microscopic and kinetic model in Figure 1.9. We mentioned the merits of the analytical proofs in terms of long-term behaviour. The Elo-model is also an example of a saving in computing time. Although the multi-dimensional parabolic equation (1.22) still has to be solved, the computing time is shorter than the microscopic simulations including Monte Carlo runs, see [71].

In the context of pedestrian-dynamics the authors in [95] compare required computation times. Therein the macroscopic model is solved faster by a factor of 6. It should be noted that the computation time increases with an increase of agents N, this is not the case in the macroscopic model.

The Eikonal-equation (1.1) is solved on a squared grid with a **fast sweeping** scheme, see [189].

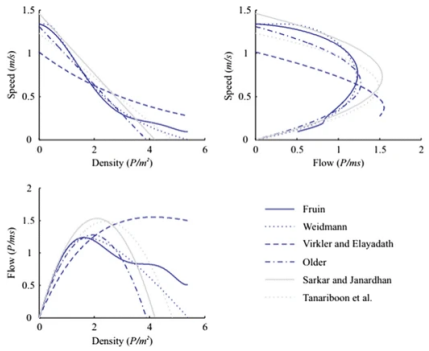

(a) Different Fundamental diagrams of pedestrian flow characteristics. Source: [61]

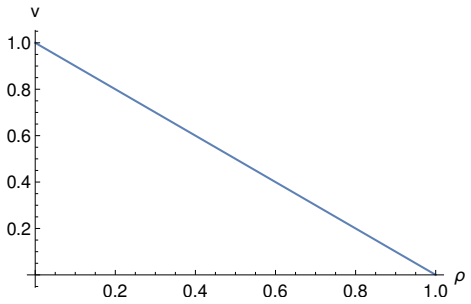

(b) Fundamental diagram for Burgers equation.

Figure 1.10: Fundamental diagrams empirically derived and for a macroscopic PDE.

Alternatively **fast marching** algorithms exist, see [202]. However, both algorithms are costly. Fast marching and fast sweeping have asymptotic complexity of $\mathcal{O}(n \log n)$ and $\mathcal{O}(n)$ where the latter is in praxis often slower due a large number of sweeps required, see [118]. In [57] the **Heat method** was presented. It results in a computational cost of near-linear time. Slight modification of the heat method allows to compute a smoothed distance function. Its idea is based on the heat-equation whose solutions have high regularity. This macroscopic approach can be adapted to general meshes and the microscopic scale.

1.4.4 Mixed models

An important tool in pedestrian dynamics is the so-called fundamental diagram, see [140, 222]. It represents a relationship between density ρ and velocity v. In the hyperbolic limit of a microscopic model this connection is visible, see [42]. Thus conclusions can be made about the microscopic model, too. We visualized fundamental diagrams from the literature and for Burgers equation in Figure 1.10.

As mentioned before, microscopic simulations are not possible for some models due to the high number of agents, here we mention e.g. gas dynamics. In general, as discussed briefly in Subsection 1.4.3, solvers for macroscopic problems are faster because they only have to solve one equation, see [63, 178]. Microscopic models, however, are more accurate as discussed in [192]. One way to combine the advantages of macroscopic PDEs with microscopic models is to consider a mixed model. This is discussed in detail in [58]. They link an ODE-system of i agents of the form

$$\frac{d}{dt}x_i(t) = v_m[\vec{x}](x_i) \tag{1.34}$$

with a PDE

$$\partial_t \rho(x,t) + \operatorname{div}\left(v_M[\rho(t,.)](x)\rho(t,x)\right) = 0. \tag{1.35}$$

This multiscale model is connected via a suitable combination of the two velocity-fields v_m and v_M in a so-called **multiscale velocity field**

$$v[\vec{x},\rho] := l v_m[\vec{x}] + (1-l)v_M[\rho], \qquad l \in [0,1].$$

The velocity-field v then replaces v_m and v_M in (1.34) and (1.35).

In [94] a similar approach was followed for pedestrian dynamics by coupling an SDE with a PDE. They discuss identifiability of the parameters appearing and introduce a Bayesian method to perform the identification. As mentioned in [58], the model of a CA is easily couplable due to an external potential V depending on ρ. In mentioned book they discuss a broad overview of ways to couple the three scales and also point to applications in traffic dynamics and biology, see also [144, 187].

1.5 Main Contributions

In this Section, we have presented the modelling in life- and social sciences at different scales and how these scales are connected. The techniques presented show that this gives advantages both on the mathematical side and in the applications. We conclude the introduction with an overview of how this thesis contributes to the field.

In Chapter 2, we introduce a microscopic model with size-exclusion to model an evacuation situation, based on a Cellular Automata. Due to the fact that this is a discrediting of a real-world experiment, we address the issues in modelling the domain Ω and in particular the exit Γ_E. We analyse problems arising in calibration at the microscopic level in the context of stochastic models and Monte Carlo methods. We discuss different potentials at the macroscopic level and their practical and analytical properties. We derive a macroscopic model for shoving based on microscopic considerations and outline its analysis based on an derived entropy. The model has a formal gradient flow structure with respect to the Wasserstein metric. We compare the model numerically with simulations in the absence of pushing.

In the following Chapter 3 we have extended the work of [71, 121]. We have incorporated at the microscopic level a fluctuation factor σ in the performance-strength ρ. We motivated this in team sports from possible different line-ups in soccer or due to random factors, for example dice rolls. We have shown existence and regularity for the kinetic model, a Fokker-Planck equation. Subsequently, we simplified the model to performance fluctuations in ρ of the same order of magnitude. We compared this reduced kinetic model numerically with the microscopic model and showed strong agreement of the two scales. Subsequently, under the choice of directions parameters depending on σ, we were able to show the convergence of the rating r against the expected value θ of the playing strength ρ.

In Chapter 4 we derive a diffusion term with compact support from microscopic considerations. We show existence and uniqueness for a regularized initial data using the strong theory for the so-called Stefan problem. Using a rigorous limit, we also show the existence of weak solutions in the general case independent of the jump condition occurring in the Stefan problem. Thus we extend the existence theory for this class of PDEs. We emphasize our findings at both scales using numerical simulations.

1.6 Declaration of Authorship

Chapter 2 consists of joint work with Gaspard Jankowiak and Marie-Therese Wolfram and was published in *Networks & Heterogeneous Media*, **15** (2021). Chapter 3 is joint work with Bertram Düring and Marie-Therese Wolfram and was published in *Kinetic and Related Models*, **14** (2021). Chapter 4 contains results of an ongoing collaboration with Laura Kanzler and Christian Schmeiser. All three Chapters are based on discussions and exchange of ideas with mentioned co-authors.

2 Micro-and macroscopic modeling of crowding and pushing in corridors

Michael Fischer, Gaspard Jankowiak, and Marie-Therese Wolfram
Published in *Networks & Heterogeneous Media*, **15** (2020), pp. 405-426.

You just keep pushing. You just keep pushing. I made every mistake that could be made. But I just kept pushing.

Rene Descartes

Contents

Abstract

Experiments with pedestrians revealed that the geometry of the domain, as well as the incentive of pedestrians to reach a target as fast as possible have a strong influence on the overall dynamics. In this

paper, we propose and validate different mathematical models at the micro- and macroscopic levels to study the influence of both effects. We calibrate the models with experimental data and compare the results at the micro- as well as macroscopic levels. Our numerical simulations reproduce qualitative experimental features on both levels, and indicate how geometry and motivation level influence the observed pedestrian density. Furthermore, we discuss the dynamics of solutions for different modeling approaches and comment on the analysis of the respective equations.

2.1 Introduction

In this paper, we develop and analyze mathematical models for crowding and queuing at exits and bottlenecks, which are motivated by experiments conducted at the Forschungszentrum Jülich and the University of Wuppertal, see [6]. In these experiments, student groups of different size were asked to exit through a door as fast as possible. Each run corresponded to different geometries of the domain, ranging from a narrow corridor to an open space, as well as different motivation levels, by giving more or less motivating instructions. The authors observed that

- The narrower the corridor, the more people lined up. This led to a significantly lower pedestrian density in front of the exit.
- A higher motivation level led to an increase of the observed densities. However its impact on the density was smaller than changing the shape of the domain.

Adrian et al. [6] supported their results by a statistical analysis of the observed data as well as computational experiments using a force based model. We follow a different modeling approach in this paper, proposing and analyzing a cellular automaton (CA) model which is motivated by the aforementioned experiments. We see that these minimalistic mathematical models reproduce the observed behavior on the microscopic as well as macroscopic level.

There is a rich literature on mathematical models for pedestrian dynamics. Ranging from microscopic agent or cellular automaton based approaches to the macroscopic description using partial differential equations. The social force model, see [108, 112, 175], is the most prominent individual based model. Here pedestrians are characterized by their position and velocity, which change due to interactions with others and their environment. More recently, the corresponding damped formulation, see [6], has been considered in the literature. In cellular automata (CA), another much used approach, individuals move with given rates from one discrete cell to another. One advantage of CA approaches is that the formal passage from the microscopic to the macroscopic level is rather straight-forward based on a Taylor expansion of the respective transition rates. This can for example be done systematically using tools from symbolic computation, see [138]. CA approaches have been used successfully to describe lane formation, as for example in [174], or evacuation situations, such as in [136]. The dynamics of the respective macroscopic models was investigated in various situations such as uni- and bidirectional flows or cross sections, see for example [39, 42].
Macroscopic models for pedestrian dynamics are usually based on conservation laws, in which the average velocity of the crowd is reduced due to interactions with others, see [185, 221]. In general it is assumed that the average speed changes with the average pedestrian density, a relation known as the fundamental diagram. In this context, finite volume effects, which ensure that the maximum pedestrian density does not exceed a certain physical bound, play an important role. These effects result in nonlinear diffusivities, which saturate as the pedestrian density reaches the maximum density, and cross-diffusion in case of multiple species, see for example [39]. One of the most prominent macroscopic models is the Hughes model, see [65, 117]. It consists of a nonlinear conservation law for

the pedestrian density which is coupled to the eikonal equation to determine the shortest path to a target (weighted by the pedestrian density). We refer to the textbooks by Cristiani et al., see [58] and Maury and Faure, see [157], for a more detailed overview on pedestrian dynamics.

Many PDE models for pedestrian dynamics can be interpreted as formal gradient flows with respect to the Wasserstein distance. In this context, entropy methods have been used successfully to analyze the dynamics of such equations. For example, the boundedness by entropy principle ensures the global in time existence of weak solutions for large classes of nonlinear partial differential equation systems, see [127]. These methods have been proven to be useful also in the case of nonlinear boundary conditions and were also used by Burger and Pietschmann [42] to show existence of stationary solutions to a nonlinear PDE for unidirectional pedestrian flows with nonlinear inflow and outflow conditions. The respective time dependent result was subsequentially presented in [94].

The calibration of microscopic pedestrian models is of particular interest in the engineering community. Different calibration techniques have been used for the social force model, see [124, 170] and CA approaches, see [198, 199]. Nowadays a large amount of data is publicly available - for example the database containing data for a multitude of experimental setups at the Forschungszentrum in Jülich, or data collected in a Dutch railway stations over the course of one year, see [55]. However, many mathematical questions concerning the calibration of macroscopic and mean-field models from individual trajectories are still open.

In this paper, we develop and analyze mathematical models to describe queuing individuals at exits and bottlenecks. Our main contributions are as follows:

- Develop microscopic and macroscopic models to describe pedestrian groups with different motivation levels and analyze their dynamics for various geometries.
- Calibrate and validate the microscopic model with experimental data in various situations.
- Compare the dynamics across scales using computational experiments.
- Present computational results, which reproduce the experimentally observed characteristic behavior.

This paper is organized as follows. We discuss the experimental setup and the proposed CA approach in Section 2.2. In Section 2.3, we present the details of the corresponding CA implementation and use experimental data to calibrate it. Section 2.4 focuses on the description on the macroscopic level by analyzing the solutions to the corresponding formally derived PDE. We conclude by discussing alternative modeling approaches in Section 2.5 and summaries our findings in Section 2.6.

2.2 The experimental setup and the microscopic model

2.2.1 The experimental setup

We start by discussing the experiments, which serve as the motivation for the proposed microscopic model, see [6]. These experiments were conducted at the University of Wuppertal, Germany. The respective data is available online, see [4].
The conducted experiments were designed to obtain a better understanding how social cues and the geometry of the domain influence individual behavior. For this purpose runs with five different corridor widths, varying from 1.2 to 5.6 meters, were conducted over the course of several days. For each corridor, a group of students was instructed to reach a target. These runs were then repeated with

varying instructions, for example suggesting that queuing is known to be more efficient or suggesting to go as fast as possible. The instructions were given to vary the motivation level and see their effect on the crowd dynamics. The number of students in the different runs (which corresponded to the different corridor width) varied from 20 to 75. The trajectory of each individual was recorded and used to compute the average density with the software package JuPedSim, available at [5]. The post-processed data showed that the average pedestrian density becomes particularly high in a 0.8×0.8 meter area, 0.5 meters in front of the exit, highlighted in Figure 2.1. Within this area, average densities up to 10 p/m^2 (pedestrians per square meter) were observed. The densities varied significantly for the different runs - they were much lower for narrow, corridor-like domains and increased with the motivation level. Further details on the experimental setup can be found in [6].

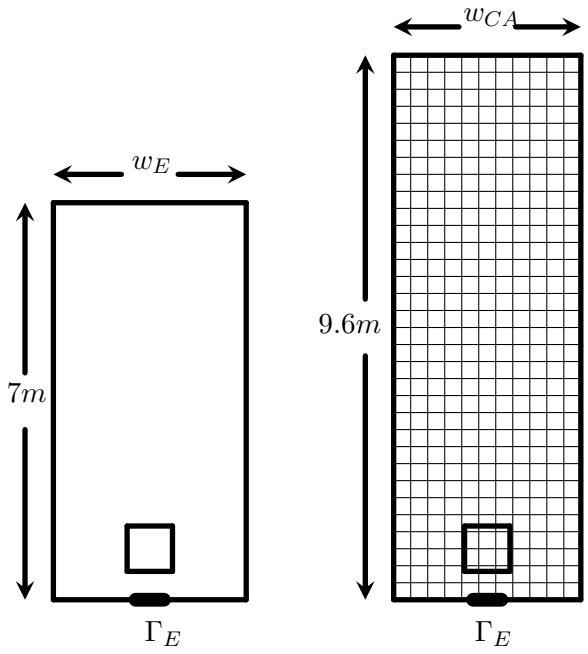

Figure 2.1: Left: Sketch of experimental setup at the University of Wuppertal, showing the corridor width w_E in the experiments, the exit Γ_E and the measurement area. Right: computational domain with adapted width w_{CA} to ensure a consistent discretization of the exit and an increased length $l_{CA} = 9.6m$.

2.2.2 The cellular automaton approach

In the following, we introduce a cellular automaton approach to describe the dynamics of agents queuing in front of the bottleneck. The dynamics of agents is determined by transition rates, which depend on the individual motivation level and the distance to the target.
We split the domain into squares with sides of length $\Delta x = 0.3$m. This discretization corresponds to a maximum packing density of 11.11 p/m^2. Cell-sizes of 0.09m^2 have a comparable area to ellipses with semi-axes $a = 0.23$m and $b = 0.12$m - a reference measure for pedestrians commonly used in agent based simulations, see [104]. The cellular automaton is implemented on a Moore neighborhood, see Figure 2.2a. Agents are allowed to move into the eight neighboring sites. Their transition rates depend on the availability of a site – a site can only be occupied by a single agent at a time – the potential φ, which corresponds to the minimal distance to the exit, as well as the individual motivation level. The

positions of all agents are updated simultaneously, which is known as a parallel update. To do so, we calculate the transition rates for every agent and resolve possible conflicts. In case of a conflict, the respective probabilities of the two agents wanting to move into the site are re-weighted, and one of them is selected. This solution has been proposed by [43, 136] and is illustrated in Figure 2.2b.
Particular care has to be taken when modeling the exit. In doing so, we consider the special Markov-process, where a single agent is located at distance Δx to the exit, see Figure 2.3a. We see that the exit can stretch over two or three cells. However, each setting has different exit probabilities and influences the exit rate. Figure 2.3b illustrates the different exit rates for the two situations in case of a single agent. We observe that the exit rate is higher if the exit is discretized using two cells. To ensure a consistent discretization of the exit for all corridor widths, we choose a discretization using three cells for all corridors. Therefore, we changed the respective corridor widths in the presented computational experiments from 1.2m, 3.4m and 5.6m to 0.9m, 3.3m and 5.7m, as illustrated in Figure 2.1. Furthermore, we extended the corridor to 9.6m to ensure sufficient space for all agents in case of larger groups. Note that in the actual experiments individuals were waiting behind the corridor entrance.

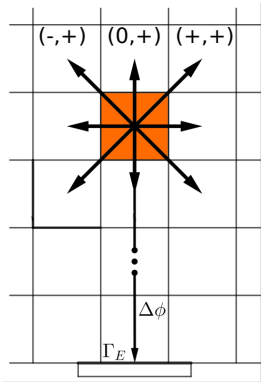

(a) Moore neighborhood and selected elements of I; the potential φ corresponds to the distance to the exit.

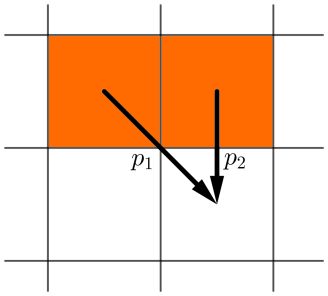

(b) Conflict: Agent 1 wins with probability $\tilde{p}_1 = p_1/(p_1 + p_2)$, agent 2 with probability $1 - \tilde{p}_1$.

Figure 2.2: Cellular automaton: transition rules.

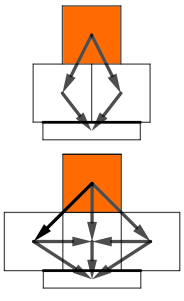

(a) Two vs. three cells.

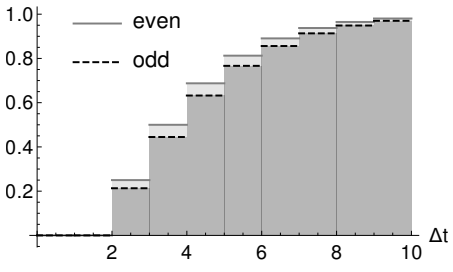

(b) Two vs. three: comparison of the exit rate as a function of time.

Figure 2.3: Discretization of the exit. In the case of an even number of cells, a central positioned agent will leave the corridor faster than in the case of three cells.

Transition-rates and the master equation

The transition rates are based on the following assumptions, which are motivated by the previously detailed experiments:

- Individuals want to reach a target as fast as possible.
- They can only move into a neighboring site if it is not occupied.
- The higher the motivation level, the larger the transition rate.

Let $\rho = \rho(x, y, t)$ denote the probability of finding an individual at site (x, y) at time t and let μ denote the motivation level. We will use the following abbreviation to state the master equation in 2D. Let I denote the Moore neighbourhood of the cell (x, y); then the neighboring cells are indexed using the signs $I := \{-, 0, +\}^2 \setminus \{(0, 0)\}$, see Figure 2.2a. The transition rate is given by

$$\mathcal{T}^{ij}(x, y) = \frac{1}{8(3-\mu)} \exp\left(\beta(\varphi(x, y) - \varphi(x + i\Delta x, y + j\Delta x))\right). \tag{2.1}$$

The prefactor $\frac{1}{8}$ is a scaling constant such that

$$\sum_{(i,j)\in I\cup\{(0,0)\}} \mathcal{T}^{ij}(x, y) = 1 + \mathcal{O}((\Delta x)^2)$$

holds. The parameter β plays an important role to weigh the transition rates to the neighboring sites. For $\beta = 0$, the transition rates are equidistributed over the neighboring cells and therefore the dynamics would correspond to a random walk. In the limit $\beta \to \infty$, individuals will move in direction of the steepest descent of φ, and the dynamics become deterministic. Since the potential φ corresponds to the distance to the target, the parameter β has to scale as m^{-1}. Maury suggests in [157] that it should be proportional to the characteristic distance Δx^{-1}, which would correspond to the value 3.33 in our setting. The prefactor $(3 - \mu)^{-1}$ changes the transition rates depending on the motivation level $\mu \in (-\infty, 1)$. The smaller μ, the less likely an agent is to move, see Remark 2.2.2. Additionally we consider size-exclusion, which corresponds to the prefactor $(1 - \rho(x + \Delta x, y, t))$ in the following master-equation. It ensures that the target site is not already occupied. Then the probability that a site (x, y) is occupied at time $t + \Delta t$, is given by

$$\begin{aligned}\rho(x, y, t + \Delta t) =& \rho(t, x, y) - \rho(x, y, t) \sum_{(i,j)\in I} \mathcal{T}^{ij}(x, y)(1 - \rho(x + i\Delta x, y + j\Delta x, t)) \\ &+ \sum_{(i,j)\in I} \rho(x + i\Delta x, y + j\Delta x, t)\mathcal{T}^{ij}(x + i\Delta x, y + j\Delta x)(1 - \rho(x, y)).\end{aligned} \tag{2.2}$$

In short, the first sum corresponds to all possible moves of an agent in (x, y) to neighboring sites. The second sum all possible moves from neighboring agents into that site.

We recall that agents can leave the domain from all three fields in front of the exit. In a possible conflict situation, that is two or three agents located in the exit cells want to leave simultaneously, the conflict situation is resolved and the winner exists with probability p_{ex}.

Remark 2.2.1. The choice of a Moore neighborhood instead of a Neumann neighborhood (as in [174, 228]), is based on the experimental observations (individuals make diagonal moves to get closer to the target). However, the choice of the neighborhood does not change the structure of the limiting partial differential equation.

Remark 2.2.2. Note that for the largest motivation level, that is $\mu = 1$ the probability of staying is given by

$$\mathcal{T}^{00}(x,y) = 1 - \sum_{(i,j)\in I} \mathcal{T}^{ij}(x,y) = \frac{2-\mu}{3-\mu} = \frac{1}{2}.$$

Such agents will move every second time-step. We see that the motivation μ has a direct influence on the desired maximum velocity v_{max} on a microscopic level. It also ensures that it is very unlikely that individuals step back in the case of a high number of agents between the agent and its target Γ_E.

2.3 Validation and calibration of the CA model

2.3.1 Implementation of the CA approach

We start by briefly discussing the implementation of the CA, which will be used for the calibration in the subsequent section. A CA simulation returns the average exit time (that is the time when the last agent leaves the corridor) depending on the number of agents n, the corridor-width $w \in \{0.9, 3.3, 5.7\}$, the motivation μ, the length of a time-step Δt and the parameter β. Each CA simulation is initialized with a random uniform distribution of agents. For given parameters the returned average exit time $\bar{T}$ and maximum observed density is estimated by averaging over 5000 CA simulations. Note that we calculate this density in the area highlighted in Figure 2.1.
We check the consistency of the estimated average exit time by varying the number of Monte-Carlo simulations. We observe that the distribution of the exit time converges to a unimodal curve, see Figure 2.4c. Similar results are obtained across a large range of parameter combinations.

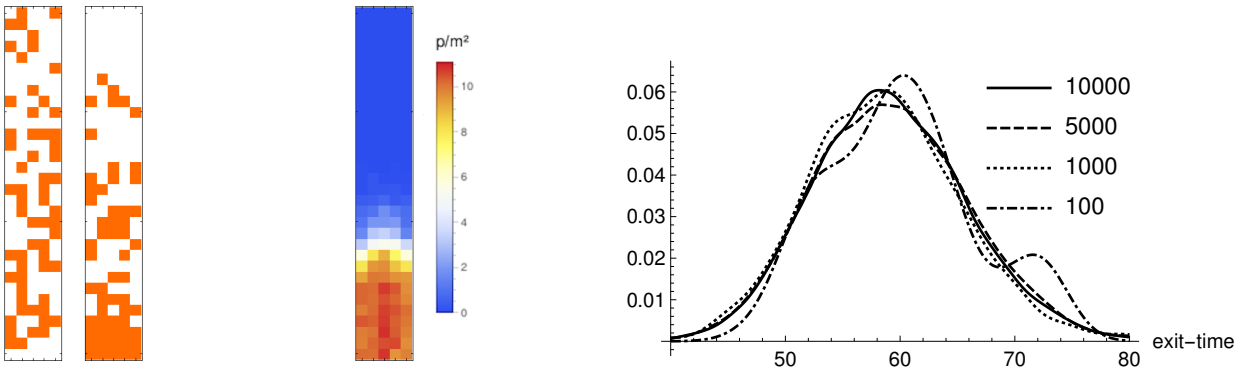

(a) Distribution of $n = 40$ agents at time $t = 0$ and $t = 16\Delta t$.

(b) The simulated density.

(c) Densities of exit times when increasing the number of Monte-Carlo runs.

Figure 2.4: Solutions of the CA approach.

2.3.2 Calibration

In this section, we discuss a possible calibration of the developed CA approach using the experimental data available, see [4]. We wish to identify the parameter scaling parameter β, the timestep Δt and the exit rate p_{ex}. To do so, we make the following assumptions:

- The outflow rate p_{ex} does not depend on the motivation level and the corridor width.
- There is a one-to-one relation between the parameter β and the time step Δt.

We start by considering the dynamics of a single agent in the corridor. These dynamics, although not including any interactions, give first insights and provide reference values for the calibration. Velocities of pedestrians are often assumed to be Gaussian distributed. Different values for the mean and variance can be found in the literature, see for example [67, 226]. We set the desired maximum velocity of a single agent to $v_{max} = 1.2\frac{m}{s}$, as for example in [67]. Hence a single motivated agent, having motivation level $\mu = 1$, needs approximately 8 seconds to travel the 9.6m long corridor.

Let $\bar{N}$ denote the average number of time steps to the exit. We will see in the following that there is a one to one relationship between the scaling parameter β and the exit time, which allows us to estimate the time step Δt.
Figure 2.5a illustrates the dynamics of this single agent for different values of β – we see that the larger β, the straighter the path to the exit. We observe that the average number of time steps $\bar{N}$ to the exit of an agent starting at the same position converges as β increases, see Figure 2.5b. The observed

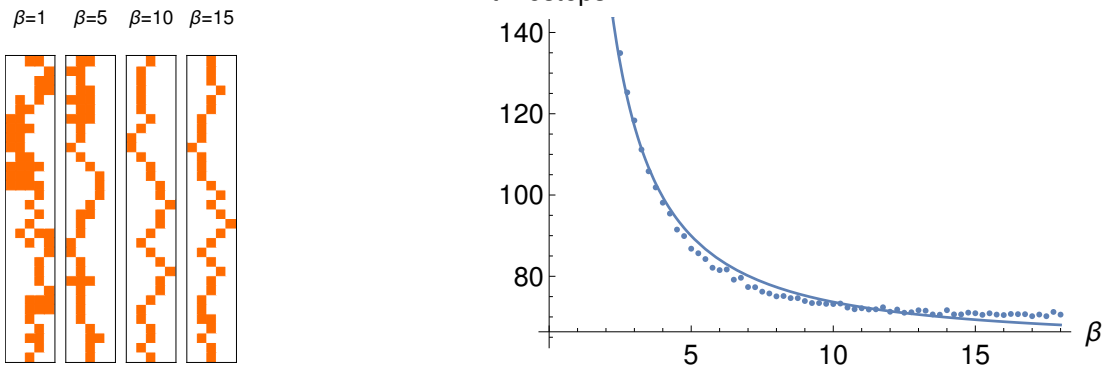

(a) Trajectories for different β - increasing β reduces the randomness of the walk.

(b) $\bar{N}$ for different values of β. The dots mark experimental data, the curve is that of the relation (2.3).

Figure 2.5: Influence of the scaling parameter β on individual dynamics.

relation between the exit time and the value of β in Figure 2.5b can be estimated by a function of the form

$$\bar{N}(\beta, p_{ex} = 1.1) = 63.528 + \frac{244.082}{\beta^{1.38148}}, \tag{2.3}$$

which was computed using a least square-approach for $a + \frac{b}{\beta^c}$. The functional relation captures the asymptotic behavior correctly (converging to the minimum number of steps going straight to the exit) and the sharp increase for small β.
This asymptotic relation allows us to estimate the time steps Δt for a given value of β in case of a single agent. Since a motivated agent moves on average every second step, it needs approximately 64 steps to exit the corridor, which corresponds to 32 vertical fields. A somehow similar approach was proposed in [228], where the position of agents was updated according to the individual velocity.
We will now estimate the missing two parameters β and p_{ex} using three different data sets, see Table 2.1. We restrict ourselves to these three datasets, since the number of individuals in each

Run	$\mu = 1$	μ_0
01, $n = 1$	$8s$	
02, $n = 63, w = 1.2m$	$53s$	$64s$
03, $n = 67, w = 3.4m$	$60s$	$68s$
04, $n = 57, w = 5.6m$	$55s$	$57s$

Table 2.1: exit times for different runs and different motivations from [6]. Run 01 is used to set the desired maximum velocity v_{max}.

run is similar and their initial distribution is close to uniform, fitting the initial conditions of the CA simulations best. For each run, we use the respective modified corridor width w, to ensure a consistent discretization of the exit and the number of agents n as detailed in Table 2.1.

Reference values: We use the experimental data to obtain reference values for β and p_{ex}. For p_{ex}, we use all data sets available, that is a total number of 980 trajectories recorded for corridors of different widths and consider the respective exit times. This gives a first approximation $p_{ex} = 1.1\frac{p}{s}$, which we use as a reference value for the calibration later on. A similar value for p_{ex} was reported in [104]. We will allow for estimates within a 50% deviation from that value. Furthermore, we restrict β to $[0.5, 10]$ (motivated by the observations in Figure 2.5a).

The calibration is then based on minimizing the difference between the observed exit time and the computed average exit time $\bar{T}$. We define the the average exit time

$$\bar{T} = \bar{T}(\beta, p_{ex}, \Delta t, \mu, n, w) : [0, \infty) \times \mathbb{R}^+ \times \mathbb{R}^+ \times (-\infty, 1] \times \mathbb{N} \times \{0.9, 3.3, 5.7\} \to \mathbb{R}^+ ,$$

that is the time needed for the last agent to leave the domain, for n individuals in a corridor of width w and parameters β, p_{ex}, Δt and μ. The calibration is then based on minimizing the functional

$$\begin{aligned} \mathcal{Z} = \Big(&(\bar{T}(\beta, p_{ex}, 63, \Delta t, 0.9) - 53)^2 + (\bar{T}(\beta, p_{ex}, 67, \Delta t, 3.3) - 60)^2 \\ &+ (\bar{T}(\beta, p_{ex}, 57, \Delta t, 5.7) - 55)^2 \Big)^{0.5} , \end{aligned} \tag{2.4}$$

using the data stated in Table 2.1. The functional $\mathcal{Z}$ is not differentiable, hence we used derivative free methods to find a minimum. We first used a parallel Nelder-Mead, which did not converge. We believe that this is caused by the stochasticity of the problem (since we average over 5000 Monte-Carlo runs to compute the average exit time) as well as the form of the functional itself. Similar problems were reported in [194]. Systematic computational experiments show that the parameter β has a small influence on the exit time. In narrow corridors, increasing the value of β does not improve the exit time, since the geometry restricts the range of jumps. In wider corridors, β plays a more important role. However, we have seen that the exit time for a single agent converges as β increases. Therefore, we can not expect a unique single optimal value. Furthermore, we believe that the parameter β has a smaller influence the more agents are in the corridor.
Finally, we estimate the two parameters β and p_{ex} using a discrete search in the range $[0.5, 10] \times [0.55, 1.65]$. In doing so, we see that the outflow parameter p_{ex} can be clearly estimated for a fixed value of β, see Figure 2.6b. However, the parameter β is much more difficult to determine, as Figure 2.6a shows. Using the three data sets stated in Table 2.1 we obtain the best fit using

$$(\beta^{\min}, p_{ex}^{\min}) \simeq (3.84, 1.15) ,$$

which leads to a deviation of 1.04 seconds in Equation (2.4). With a similar approach we then estimate the parameter $\mu_0 \simeq -1.22$ for less motivated agents according to Table 2.1. This results in a speed of $0.57\frac{m}{s}$.

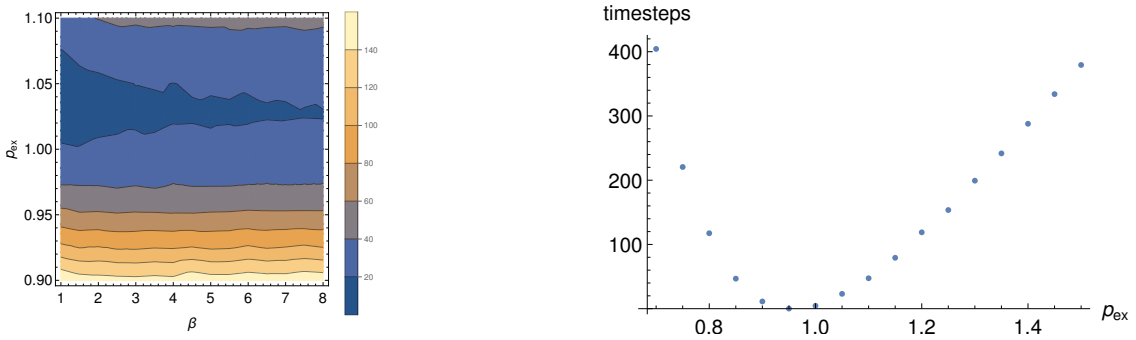

(a) The average exit time for a discrete set of β/p_{ex}-combinations.

(b) $\bar{T}$ as a function of p_{ex} for a fixed value of β.

Figure 2.6: Average exit time as a function of β and p_{ex}, or p_{ex} only.

Remark 2.3.1. At first glance, the value $\beta = 3.84$ may seem too small given the simulation results shown in Figure 2.5a. However, Maury suggests a similar value in [157] - in particular $\beta \approx 1/(\Delta x)$ where Δx is the cell size. In our setting this would correspond to the value 3.33, which is close to the value obtained through from the calibration. This can be explained by the fact that the effect of β is smaller in crowded rooms.

2.3.3 Microscopic simulations

We conclude this section by presenting calibrated CA simulations, that are consistent with the experimental data. We observe that wider corridors lead to a higher maximum density in front of the exit for different motivation levels, see Figure 3.2. Note that this also the case when changing the outflow rate p_{ex}. Higher motivation levels μ lead to higher densities in front of the exit as can be seen in Figure 2.8b. A similar behavior was observed in the experimental results as well as the computational experiments discussed in [6, 104].

Remark 2.3.2. Note that we observe similar results if we replace the exponential function in (2.1) by $\max(0, \varphi(x, y) - \varphi(x + \Delta x, y))$. However, this function does not satisfy the necessary regularity to at least formally derive the corresponding macroscopic PDE model.

2.4 The macroscopic model

In this section, we derive and study the corresponding macroscopic PDE model, in particular existence of solutions as well as different options to calculate the path to the exit.
The corresponding macroscopic PDE can be formally derived from the cellular automaton approach discussed in Section 2.2.2. Here we use a Taylor expansion to develop the transition rates and functions in $x \pm \Delta x$ and $y \pm \Delta x$. This rather tedious calculation can be done in a systematic manner using a similar approach as discussed in [138].

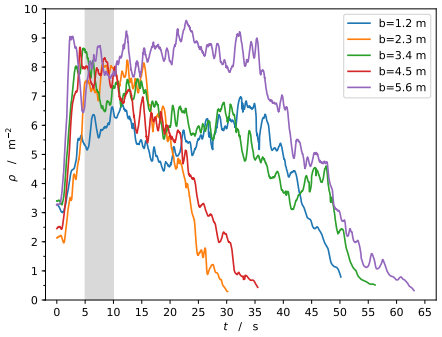

(a) Experimental results, reproduced with permission from [6].

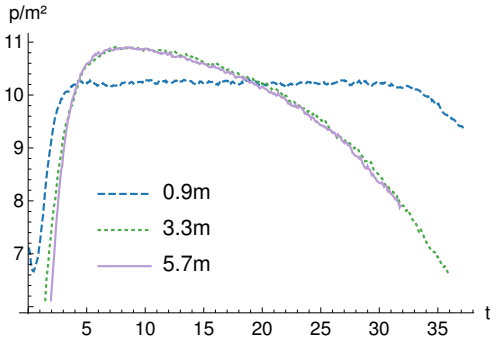

(b) Microscopic simulations for the densities for $n = 60$ and $\mu = 1$.

Figure 2.7: Impact of the corridor width on the maximum density. The CA approach yields comparable results for high density regimes and low motivation level.

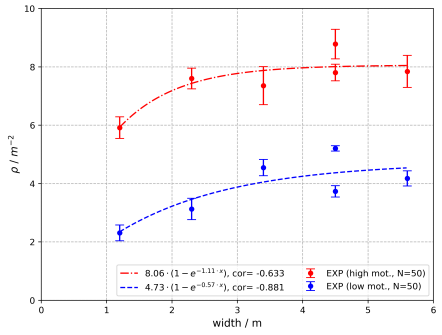

(a) Experimental results (with permission from [104])

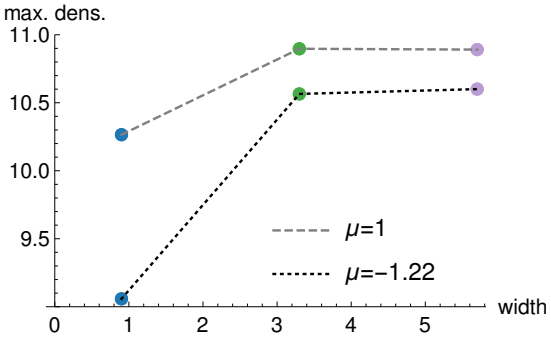

(b) Maximum agent density using the CA model with $n = 60$.

Figure 2.8: Impact of the motivation level on the maximum pedestrian density: experimental (left) vs. microscopic simulations (right).

2.4.1 The PDE and its analysis

We recall that $\rho = \rho(x, y, t)$ denotes the density of pedestrians at position (x, y) and time t and $\varphi = \varphi(x, y)$ is the potential leading towards the exit Γ_E. Let $\Omega \subset \mathbb{R}^2$ denote the domain, Γ_W the walls and Γ_E the exit with $\Gamma_W \cup \Gamma_E = \partial\Omega$ and $\Gamma_W \cap \Gamma_E = \emptyset$.
Then the pedestrian density $\rho = \rho(x, y, t)$ satisfies a nonlinear Fokker-Planck equation for all $(x, y) \in \Omega$:

$$\begin{aligned} \partial_t \rho(x, y, t) &= \alpha_\mu \operatorname{div} \left(\nabla \rho(x, y, t) + 2\beta \rho(x, y, t)(1 - \rho(x, y, t))\nabla \varphi(x, y)\right) \\ \rho(x, y, 0) &= \rho_0(x, y). \end{aligned}$$

The parameter

$$\alpha_\mu := \frac{1}{8(3 - \mu)} \tag{2.5a}$$

depends on the motivation μ, while β corresponds to the ratio between the drift and diffusion. The function $\rho_0 = \rho_0(x, y)$ is the initial distribution of agents. Equation (2.5) is supplemented with the following boundary conditions

$$\begin{aligned} \mathbf{j} \cdot \mathbf{n} &= 0, \qquad && \text{on } \Gamma_W, \\ \mathbf{j} \cdot \mathbf{n} &= p_{ex}\rho, && \text{on } \Gamma_E, \end{aligned} \tag{2.5b}$$

where $\mathbf{j} = \nabla\rho + 2\beta\rho(1-\rho)\nabla\varphi$ and $\mathbf{n}$ is the unit outer normal vector. We recall that the parameter p_{ex} is the outflow rate at the exit Γ_E.

Remark 2.4.1. Note that the motivation parameter μ enters the PDE via α_μ only. It corresponds to a rescaling in time, accelerating or decelerating the dynamics.

First we discuss existence and uniqueness of solutions to (2.5). Stationary solutions of a similar model were recently investigated by Burger and Pietschmann, see [42]. The existence of the respective transient solutions was then shown in [94]. It is guaranteed under the following assumptions:

(A1) Let $\Omega \subset \mathbb{R}^2$ with boundary $\partial\Omega$ in C^2.

(A2) Let p_{ex} be in $[0, 1]$.

(A3) Let φ be in $H^1(\Omega)$.

Note that assumption (A1) is not satisfied in the case of a corridor. However, as pointed out in [42], this condition could be relaxed to Lipschitz boundaries with some technical effort.

Theorem 2.1. *(Existence of weak solutions) Let assumptions (A1)-(A3) be satisfied. Let* $\mathcal{S} = \{\rho \in L^2(\Omega) : 0 \le \rho \le 1\}$ *and the initial datum* $\rho_0 : \Omega \to \mathcal{S}^o$ *be a measurable function such that* $E(\rho_0) < \infty$*, where entropy* E *is defined by*

$$E(\rho) = \int_\Omega \left[\rho \log \rho + (1-\rho)\log(1-\rho) + 2\beta\rho\varphi\right] dx\,.$$

Then there exists a weak solution to system (2.5) in the sense of

$$\int_0^T \Big[\langle \partial_t \rho, \varphi \rangle_{H^{-1}, H^1} ds \; - \\ \alpha_\mu \int_\Omega ((2\beta\rho(1-\rho)\nabla\varphi + \nabla\rho))\nabla\varphi dx + p_{ex} \int_{\Gamma_E} \rho\varphi ds \Big] dt = 0,$$

for test functions $\varphi \in H^1(\Omega)$*. Furthermore*

$$\begin{aligned} &\partial_t \rho \in L^2(0, T; H(\Omega)^{-1}), \\ &\rho \in L^2(0, T; H^1(\Omega)). \end{aligned}$$

The existence proof is based on the formulation of the equation in entropy variables, that is

$$\partial_t \rho(x, t) = \operatorname{div}(m(\rho)\nabla u(x, t)),$$

where $m(\rho) = \rho(1-\rho)$ is the mobility function and $u = \frac{\delta E}{\delta \rho} = (\log\rho - \log(1-\rho) + 2\beta\varphi)$ the so-called entropy variable. Note that the proof is a straightforward adaptation of the one presented in [94], hence we omit its details in the following.

2.4.2 Moving towards the exit

In the following we discuss different possible choices for the potential φ.

The eikonal equation

The shortest path to a target, such as the exit Γ_E can be computed by solving the eikonal equation, see [58]:

$$\begin{aligned} \|\nabla \varphi_E(x,y)\|^2 &= 1, && \text{for } (x,y) \text{ in } \Omega, \\ \varphi_E(x,y) &= 0, && \text{on } (x,y) \text{ in } \Gamma_E. \end{aligned} \tag{2.6}$$

Solutions to (2.6) are in general bounded and continuous, but not differentiable, see [16]. However, in case of the considered corridor geometry we have the following improved regularity result.

Theorem 2.2. *(Regularity of φ_E) Let $\Omega \subset \mathbb{R}^2$ be a rectangular domain and $\Gamma_E \subset \partial\Omega$ be a line segment in one of the four edges. Then there exists a solution $\varphi_E \in H^1(\Omega)$ to (2.6).*

The proof can be found in the Appendix and is based on [16], Proposition 2.13.

The Laplace equation

Alternatively we consider an idea proposed by Piccoli and Tosin in [185]. Let $\varphi_L = \varphi(x,y)$ denote the solution of the Laplace equation on $\Omega \subset \mathbb{R}^2$:

$$\begin{aligned} \Delta \varphi_L(x,y) &= 0, && \text{for } (x,y) \text{ in } \Omega, \\ \varphi_L(x,y) &= d(x,y), && \text{for } (x,y) \text{ on } \partial\Omega, \end{aligned} \tag{2.7}$$

where $d = d(x,y)$ corresponds to the Euclidean distance of the boundary points to the exit Γ_E. Note that in this case of the corridor the function d is not differentiable at the corners but Lipschitz continuous. Hence standard methods for elliptic equations yield the following regularity result.

Theorem 2.3. *(Regularity of φ_L) Let $d \in C(\partial\Omega)$ defined as above, $\Omega \subset \mathbb{R}^2$ be bounded. Then there exists a unique solution $\varphi_L \in H^1(\Omega)$ to (2.7).*

The proof can be found in [142], Section 5.
In the following we discuss the similarities and difference of the potentials φ_E and φ_L. In case of a 1D corridor with a single exit, that is a line with a single exit on one of the two endpoints, the potentials are identical. However in the case of two exits at the respective endpoints, the Laplace equation gives $\varphi_L \equiv 0$, which does not provide a sensible potential.
Figures 2.9 and 2.10 illustrate the differences between φ_L and φ_E in 2D. Note that we choose homogeneous Neumann boundary conditions at the obstacle walls when solving the Laplace equation (2.7). We observe good agreement in case of convex obstacles, see Figure 2.9. In case of non-convex obstacles, such as the U-shaped obstacle in Figure 2.10, individuals would first get trapped inside the U using the Laplace equation. Solving the eikonal equation (2.6) is in general computationally more expensive than the Laplace equation (2.7). However, these costs are negligible since the potential is stationary and computed only once.

(a) Eikonal equation.

(b) Laplace equation (with Neumann bc at the obstacle).

Figure 2.9: Comparison of the potentials φ_E and φ_L for a convex obstacle.

(a) Eikonal equation.

(b) Laplace equation (with Neumann bc at the obstacle).

Figure 2.10: Comparison of the potentials φ_E and φ_L for a non-convex obstacle.

2.4.3 Characteristic calculus

We now consider the corresponding inviscid macroscopic model, which can be derived using a different scaling limit from the CA approach. We focus on the one dimensional case only as we can calculate solutions explicitly. A similar problem (with different boundary conditions) was partially analyzed in [65].

The inviscid PDE reduces to a scalar conservation law, posed on $\mathbb{R}_+$ of the form

$$\partial_t \rho + \partial_x j(\rho) = 0\,, \tag{2.8}$$

where the flux function is $j(\rho) = -\rho(1-\rho)$. Note that this flux corresponds to the potential $\varphi(x) = x$, hence individuals move to the left. We consider the initial condition

$$\rho(x,0) = \rho_0\, \chi_{[0,L]}\,,$$

for some positive L, where χ denotes the characteristic function. At the origin, we wish to enforce a similar outflow condition as in the viscid case and set $j(0,t) = p_{ex}\,\rho,\ t > 0$. This is equivalent to the Dirichlet boundary condition $\rho(0,t) = 1 - p_{ex}$ for all times $t > 0$, where we recall that $0 < p_{ex} \leq 1$. This is an ill-posed problem in general [149], and the boundary condition must be relaxed.

Away from discontinuities, the speed of characteristics is given by

$$j'(\rho) = -(1 - 2\rho)\,.$$

We see that they either point in- or outside of the domain, depending on the magnitude of ρ. Recall that for a shock located at $s(t)$, the Rankine-Hugoniot condition reads $[\![j'(\rho)]\!] = \dot{s}(t)[\![\rho]\!]$, where $[\![f]\!] = f^- - f^+$, with $f^\pm(x) = f(x \pm 0)$. For our choice for ρ_0, there is an initial shock at $x_r = L$, which is moving (left) at a speed of

$$\dot{x}_r = -(1 - \rho_0)\,.$$

The larger the initial pedestrian density, the slower the shock moves or the people get closer to the exit. One can easily check that such a profile satisfies the so-called *Lax entropy condition*, since

$$-1 = j'(0) \le \dot{x}_r \le j'(\rho_0)\,,$$

is it therefore admissible.
Next we discuss the behavior of solutions at the exit $x = 0$. The proper way to enforce the Dirichlet boundary condition is derived in [145, 146], and reads as follows:

$$\rho^+(0) \in \mathcal{E}[1 - p_{ex}] := \begin{cases} [0, p_{ex}] \cup \{1 - p_{ex}\} & \text{if } p_{ex} < \frac{1}{2}\,, \\ [0, \frac{1}{2}] & \text{if } p_{ex} \ge \frac{1}{2}\,. \end{cases} \tag{2.9}$$

Depending on the slope of the characteristics as well as the value of the outflow rate p_{ex}, we observe three different cases, which are detailed below and illustrated in Figure 2.11.

- *A constant profile* for $\rho_0 \le p_{ex} < \frac{1}{2}$ or $\rho_0 \le \frac{1}{2} \le p_{ex}$. In this case the characteristics have a negative slope and ρ_0 is an admissible boundary value. The function ρ vanishes when the shock originating at $x = L$ reaches the origin at time $t = \frac{L}{1-\rho_0}$. The situation is similar in the case $\frac{1}{2} < \rho_0 = 1 - p_{ex}$, for which characteristics are going inwards but where $\rho_0 \in \mathcal{E}[1 - p_{ex}]$. This case is illustrated on the lower right in Figure 2.11.

- *A shock originating at* $x = 0$ for $p_{ex} < \frac{1}{2}$ and $p_{ex} < \rho_0 < 1 - p_{ex}$. In this case $\rho_0 \notin \mathcal{E}[1 - p_{ex}]$, but $1 - p_{ex} \in \mathcal{E}[1 - p_{ex}]$ which we therefore set as a boundary value. This causes a shock at the origin, which travels to the right with speed

  $$\dot{x}_l = \frac{-p_{ex}\,(1 - p_{ex}) + \rho_0\,(1 - \rho_0)}{1 - p_{ex} - \rho_0}\,,$$

  until it collides with the back-shock. The collision time and position, $t = t_1^*$ and $x = x_1^*$ respectively, can be calculated from $x_1^* = \dot{x}_l t_1^* = L + \dot{x}_r t_1^*$. We obtain

  $$t_1^* = \frac{L}{1 - p_{ex}}\,, \quad \text{and} \quad x_1^* = \left(1 - \frac{1 - \rho_0}{1 - p_{ex}}\right) L\,.$$

  The resulting shock will then move to the left again, with speed $-p_{ex}$ and reaches the origin at time $t = \frac{\rho_0\, L}{p_{ex}(1-p_{ex})}$. This situation is shown in the center left part of Figure 2.11.

- *A rarefaction wave originating at* $x = 0$ for $\rho_0 > \frac{1}{2}$ or $\rho_0 > 1 - p_{ex}$. In this case a rarefaction wave will connect the value at the boundary, that is $\bar{\rho} = \frac{1}{2} \vee 1 - p_{ex}$, with the state ρ_0. The rarefaction

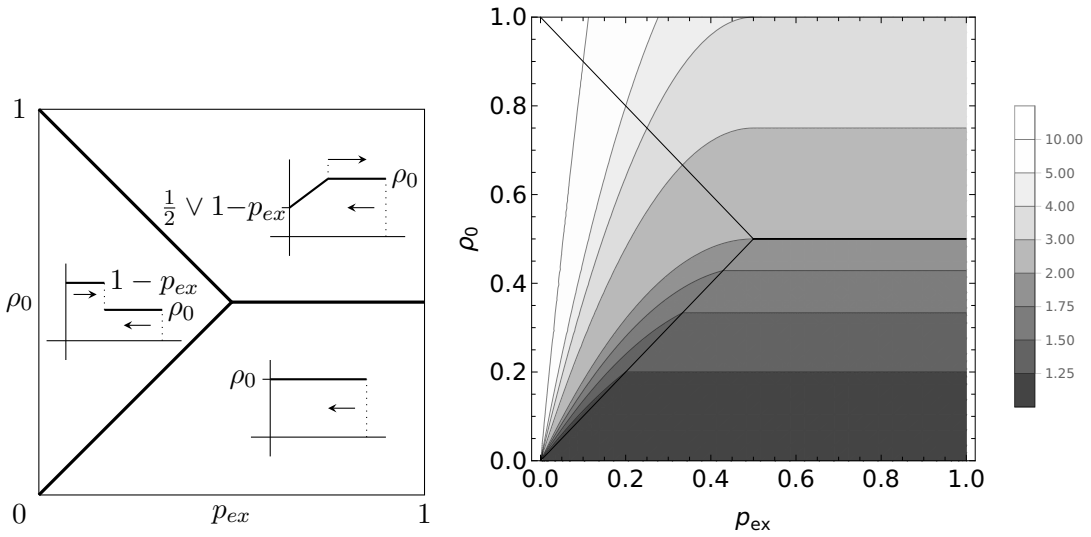

Figure 2.11: Left: Bifurcation diagram detailing the behavior of the solution to (2.8)-(2.9). The behavior along the interface lines is identical as in the bottom right corner. Right: exit time corresponding to $L = 1$.

wave is of the form $\rho(x,t) = \frac{x+t}{2t}$. More precisely we have for any $x > 0$:

$$\rho(x,t) = \begin{cases} \bar{\rho} & \text{if } \frac{x}{t} \leq (2\bar{\rho} - 1) \ , \\ \frac{x+t}{2t} & \text{if } (2\bar{\rho} - 1) < \frac{x}{t} < (2\rho_0 - 1) \ , \\ \rho_0 & \text{if } \frac{x}{t} \geq (2\rho_0 - 1) \ . \end{cases} \tag{2.10}$$

Note that for $1 - p_{ex} > \frac{1}{2}$, the constant value $\bar{\rho} = 1 - p_{ex}$ is transported into the domain at speed $2\bar{\rho} - 1$. The crest the rarefaction wave travels at speed $2\rho_0 - 1$ until it hits the back-shock at time $t_2^* = \frac{L}{\rho_0}$, for $x_2^* = \left(\frac{2\rho_0 - 1}{\rho_0}\right) L$. This results at a new shock, which originates at position x_s and with velocity $\dot{x}_s = -(1 - \rho(x_s))$. From (2.10) we also have $\rho(x_s) = \frac{x_s+t}{2t}$. Solving the resulting equation with initial condition $x_s(t_2^*) = x_2^*$ yields

$$x_s(t) = 2\sqrt{L\,\rho_0}\sqrt{t} - t \, .$$

If $1 - p_{ex} < \frac{1}{2}$, this new shock reaches 0 at time $t_3^* = 4\rho_0 L$. Otherwise, the back-shock will meet the constant state $1 - p_{ex}$ at time $t_4^* = \frac{L\rho_0}{(1-p_{ex})^2}$, for $x_4^* = \frac{L(1-2p_{ex})\rho_0}{(1-p_{ex})^2}$, resulting in a single constant state $\rho(x, t_4^*) = (1 - p_{ex})\chi_{[0,x_4^*]}$. This constant profile then moves with speed $-p_{ex}$, and reaches the origin at time $t = \frac{\rho_0 \, L}{p_{ex}(1-p_{ex})}$, see upper right corner of Figure 2.11.

Figure 2.11 illustrates how the exit time changes with the initial pedestrian density and the outflow rate. We see that for an outflow rate $p_{ex} \gtrsim \frac{1}{2}$, the initial density ρ_0 has a much stronger influence on the exit time compared to the value of p_{ex}. The situation is somehow reversed for small p_{ex}.

2.4.4 Numerical results

We conclude by presenting computational results on the macroscopic level. All simulations use the finite element library Netgen/NgSolve.

We consider a rectangular domain with a single exit as shown in Figure 2.1 and discretize it using a triangular mesh of maximum size $h = 0.1$. The potential φ is calculated in a preliminary step, by either solving the eikonal equation (2.6) or the Laplace equation (2.7). We use a fast sweeping scheme for the eikonal equation, as it can be generalized to triangular meshes, see [189]. The discretization of the nonlinear Fokker-Planck equation (2.5) is based on a 4^{th} order Runge-Kutta method in time and a hybrid discontinuous Galerkin method in space, see [147].
We choose a constant initial datum ρ_0, taken such that $\int_\Omega \rho_0 dx = \frac{n}{\rho_s}$. We recall that ρ_s corresponds to the typical pedestrian density $\rho_s = 11.11 \frac{p}{m^2}$ and n to the number of individuals. The simulation parameters are set to

$$\beta = 3.84,\ p_{ex} = 1.15,\ \Delta t = 10^{-5},\ \text{and}\ \alpha_\mu = \frac{1}{16}$$

We calculate the densities in the rectangular area highlighted in Figure 2.1. The macroscopic simulations confirm the microscopic results. Again higher densities for wider corridors are observed, see Figure 2.12.

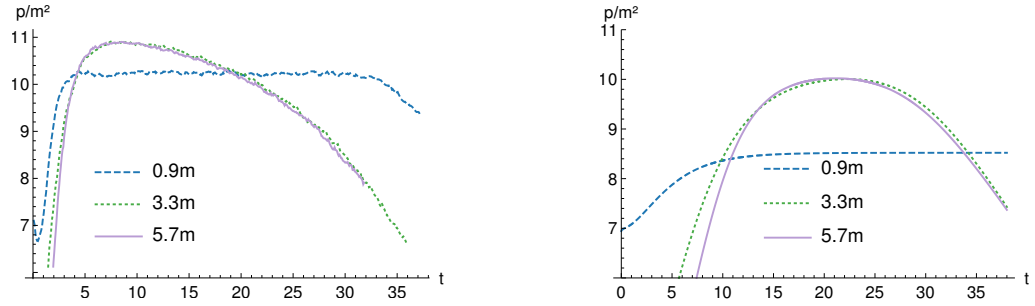

(a) Microscopic simulations.

(b) Macroscopic simulations.

Figure 2.12: Simulations for $n = 60$, $\beta = 3.84$, $\mu = 1$. We observe a good agreement between the CA (microscopic) and PDE (macroscopic) solutions. The effect of higher densities for wider corridors also occur on a macroscopic scale. There is a clear difference in behavior between narrow and wide corridors

2.5 Alternative modeling approaches

We have seen that the proposed CA approach proposed in Section 2.2.2 reproduces some features of the observed dynamics on the microscopic as well as on the macroscopic level. In the following, we discuss possible alternatives and generalizations, which we expect to result in even more realistic results.

2.5.1 Density dependent cost

Hughes [117] proposed that the cost of moving should be proportional to the local pedestrian density. In particular, moving through regions of high density is more expensive and therefore less preferential. This corresponds to a density dependent (hence time dependent) right-hand side in (2.6). In particular,

Hughes proposed a coupling via

$$\begin{aligned} \|\nabla\varphi(x,y,t)\| &= \frac{1}{1-\rho(x,y,t)}, \qquad \text{for } (x,y) \text{ in } \Omega \\ \varphi(x,y) &= 0, \qquad\qquad\qquad\quad \text{for } (x,y) \text{ in } \Gamma_E. \end{aligned} \tag{2.11}$$

We see that the right hand side, which corresponds to the cost of moving, becomes unbounded as ρ approaches the scaled maximum density 1. Such density dependent cost should lead to more realistic dynamics. However the analysis of the coupled problem (2.5)-(2.11) is open. Solutions to (2.11) have a much lower regularity than required in Theorem 2.2. We expect this to lead to similar analytic challenges as reported in [65].

2.5.2 Alternative ways to model motivation

In the following, we discuss different possibilities to include the influence of the motivation level on the dynamics. First by modifying the transition rates and second by changing the transition mechanism, allowing for shoving.

Alternative transition rates

In the transition rate (2.1), the motivation relates to the probability of jumping as detailed in Remark 2.2.2. It is therefore directly correlated to the agent's velocity on a microscopic level. However, one could assume that the motivation increases the probability to move along the shortest path. This could be modeled by transition rates of the form

$$\mathcal{T}^{ij}(x,y) = \frac{1}{8}\exp(\mu\beta(\varphi(x,y) - \varphi(x+i\Delta x, y+j\Delta x))).$$

Then the corresponding macroscopic model reads

$$\partial_t\rho(x,y,t) = \frac{1}{8}\operatorname{div}\left(\nabla\rho(x,y,t) + 2\mu\beta\rho(x,y,t)(1-\rho(x,y,t))\nabla\varphi(x,y)\right).$$

We see that the motivation level μ enters only in the convective term. Hence higher motivation is directly correlated to a higher average velocity of the crowd on a macroscopic level.

2.5.3 Pushing and shoving

Microscopic modeling

In the previously proposed model, the transition rates depended on the availability of a site and the motivation level. Another possibility to include the latter is by allowing individuals to push. Different pushing mechanisms have been proposed in the literature. In local pushing models, individuals are only able to push one neighbor into an adjacent vacant site, while in global pushing individuals can push a given number of neighbors into a direction. However, since individuals can induce movements of other individuals in some distance (and not only the neighboring sites), an implementation on bounded domains is not straight forward. In particular, it is not clear how to adapt boundary conditions in case of global pushing, as considered in [10]. In contrast, local pushing mechanisms, can be translated one-to-one on bounded domains, see [235].
We will discuss the underlying CA approach for the sake of readability in 1D only, since its generalization to 2D is obvious. We assume that individuals agents can move to a neighboring occupied cell with

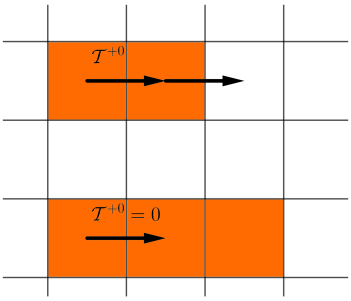

(a) Local pushing mechanism. Top: pushing is possible since the cell on the third column in free. Bottom: pushing is forbidden since the next site is occupied.

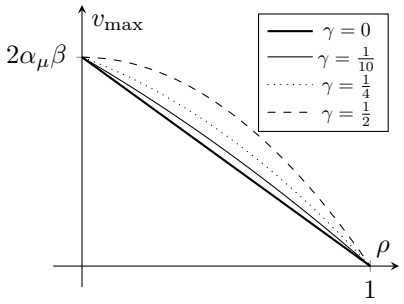

(b) Impact of pushing on the average velocity. Pushing leads to larger and increasingly concave velocities.

Figure 2.13: Effects of pushing

a given probability, by pushing the neighbor one cell further, provided that it is free. Otherwise, such a move is forbidden. This mechanism is illustrated in Figure 2.13a. In 1D, the previously introduced transition rates are given by

$$\mathcal{T}^i(x) = \alpha_\mu \exp(\beta(\varphi(x) - \varphi(x + i\Delta x))).$$

Since individuals can move to the right and left only, we will replace the superscript i by $\pm$ indicating a jump to the respective neighboring sites. Then the master equation in 1D is given by (ignoring constants):

$$\begin{aligned}
\rho(x, t+\Delta t) - \rho(x,t) = &- \rho(x)\mathcal{T}^+(x)\left((1-\rho(x+\Delta x)) + \gamma_\mu \rho(x+\Delta x)(1-\rho(x+2\Delta x))\right) \\
&- \rho(x)\mathcal{T}^-(x)\left((1-\rho(x-\Delta x)) + \gamma_\mu \rho(x-\Delta x)(1-\rho(x-2\Delta x))\right) \\
&+ \rho(x+\Delta x)\mathcal{T}^-(x+\Delta x)(1-\rho(x)) \\
&+ \gamma_\mu \rho(x+\Delta x)\rho(x+2\Delta x)\mathcal{T}^-(x+2\Delta x)(1-\rho(x)) \\
&+ \rho(x-\Delta x)\mathcal{T}^+(x-\Delta x)(1-\rho(x)) \\
&+ \gamma_\mu \rho(x-\Delta x)\rho(x-2\Delta x)\mathcal{T}^+(x-2\Delta x)(1-\rho(x))\,,
\end{aligned}$$

in which we omit t for the sake of readability. Here $\gamma_\mu = \gamma(\mu) \in [0,1]$ denotes an increasing function and corresponds to the probability of an agent pushing. Note that we obtain the original master equation (2.2) for $\gamma_\mu = 0$.

Mean-field limit

Using a formal Taylor expansion, we derive the limiting mean-field PDE where we generalized to 2D the approach mentioned previously:

$$\begin{aligned}
\partial_t \rho(x,y,t) &= \alpha_\mu \operatorname{div}((1+4\gamma_\mu\rho)\nabla\rho + 2\beta\rho(1-\rho)(1+2\gamma_\mu\rho)\nabla\varphi) \\
\rho(0,x) &= \rho_0(x,y).
\end{aligned} \tag{2.12}$$

Equation (2.12) is supplemented with no-flux and outflow conditions of type (2.5b) for a modified flux $\mathbf{j} = (1+4\gamma_\mu\rho)\nabla\rho + 2\beta\rho(1-\rho)(1+2\gamma_\mu\rho)\nabla\varphi$ and α_μ given by (2.5a).

This equation has again a formal gradient flow structure with respect to the Wasserstein metric. The respective mobility and entropy are given by

$$m(\rho) = \alpha_\mu \rho(1-\rho)(1+2\gamma_\mu \rho),$$

and

$$E(\rho) = \int_\Omega \Big[\frac{4\gamma+1}{2\gamma+1}(1-\rho)\log(1-\rho) + \rho\log\rho + \frac{2\gamma\rho+1}{2\gamma+1}\log(2\gamma\rho+1) + 2\beta\rho\varphi \Big]\, dx\,.$$

We observe that the local pushing increases the mobility and the average velocity, see Figure 2.13b. Furthermore, the velocity decreases less in low density regimes and for higher motivation levels. Note that in case of pushing, the average velocity always larger.
The local pushing weighs the $(1-\rho)\log(1-\rho)$ term and subsequently the finite volume effects much more. Furthermore, it increases the entropy by an additional strictly positive term. Hence we expect a faster equilibration speed compared to the model of Section 2.4.1. The expected behavior is confirmed by macroscopic simulations, see Figure 2.14. We consider a corridor filled with 60 people, and where we set $\beta = 3.8$. We observe that the individuals move faster towards the exit and that the congested area in front of the exit builds up faster.
Again, we recover the original PDE model by setting $\gamma_\mu = 0$. The proof of global existence to (2.12)

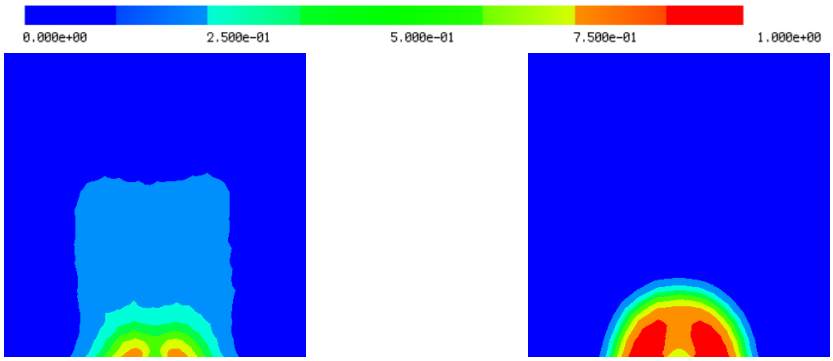

(a) $t = 5s$, $\gamma = 0$, no pushing (b) $t = 15s$, $\gamma = 0$, no pushing

(c) $t = 5s$, $\gamma = 1$, pushing (d) $t = 15s$, $\gamma = 1$, pushing

Figure 2.14: Comparison of the congestion at the exit in case of pushing (bottom row) and no-pushing (top row) for 60 individuals: We observe that people move faster towards the exit and the formation of a larger congested area in front of it.

follows arguments similar as for the original PDE model (2.5), since the pushing corresponds to a

multiplicative prefactor in the mobility and a positive term in the entropy (which can be bounded).

2.6 Conclusion

In this paper, we discussed micro- and macroscopic models for crowding and queuing at exits and bottlenecks, which were motivated by experiments conducted at the University in Wuppertal. These experiments indicated that the geometry, ranging from corridors to open rooms, as well as the motivation level, such as a higher incentive to get to the exit due to rewards, changes the overall dynamics significantly.
We propose a cellular automaton approach, in which the individual transition rates increase with the motivation level, and derive the corresponding continuum description using a formal Taylor expansion. We use experimental data to calibrate the model and to understand the influence of parameters and geometry on the overall dynamics. Both the micro- and the macroscopic description reproduce the experimental behavior correctly. In particular we observe that corridors lead to lower densities and that the geometry has a stronger effect than the motivation level. We plan to investigate the analysis of the coupled Hughes type models as well as the dynamics in case of pushing in more detail in the future.

Acknowledgments

The authors would like to thank Christoph Koutschan for the helpful discussions and input concerning the derivation of the respective mean field models using symbolic techniques. Furthermore we would like to thank the team at the Forschungszentrum Jülich and the University of Wuppertal, in particular Armin Seyfried and Ben Hein, for providing the data and patiently answering all our questions.
All authors acknowledges partial support from the Austrian Academy of Sciences via the New Frontier's grant NST 0001 and the EPSRC by the grant EP/P01240X/1.

2.7 Appendix

Proof 1 of Theorem 2.2

We start by a recalling a standard existence and regularity result from the literature, see [16] and [45]. Solutions to the eikonal equation (2.6) in $\mathbb{R}^2 \setminus \Gamma_E$ are given by the distance function

$$d(x, \Gamma_E) = \inf_{b \in \Gamma_E} |x - b|.$$

Hence we discuss the regularity of d in the following only. We define the set

$$M(x) = \arg\min_{b \in \Gamma_E} d(x, \Gamma_E).$$

If Γ_E is a straight, bounded line, the M is nonempty and consists of a single point for every $x \in \mathbb{R}^2$. Since $|(\cdot - b)|$ is uniformly differentiable in b, and $b \mapsto D_x|x - b|$ is continuous, we can deduce that the set Y

$$Y(x) := \{D_x|x - b| \colon b \in M(x)\}$$

is a singleton too. We now can apply Proposition 2.13 in [16] which states that d is differentiable at x if and only if $Y(x)$ is a singleton. Thus d is differentiable for $\mathbb{R}^2 \setminus \Gamma_E$, to be more precisely, we have $d \in C^1(\mathbb{R}^2 \setminus \Gamma_E) \cap C(\mathbb{R}^2)$.
Next we restrict d to the corridor $\Omega \subset \mathbb{R}^2$ (being an open and bounded subset of Ω).

Hence, $\varphi_E \in C(\bar{\Omega}) \cap C^1(\Omega)$. Since the L^2-norm of the first derivative of φ_E is bounded by the equation (2.6) itself, we can deduce that $\varphi_E \in H^1(\Omega)$ since

$$\|\varphi_E\|_{H^1(\Omega)} = \int_\Omega \varphi_E^2 dx + \int_\Omega (D\varphi_E)^2 dx \leq |\Omega|(\max \varphi_E + 1).$$

3 An Elo-type rating model for players and teams of variable strength

Bertram Düring, Michael Fischer, and Marie-Therese Wolfram
Published in *Kinetic and Related Models*, **14** (2021), pp. 1-24.

The process of rating players can be compared to the measurement of the position of a cork bobbing up and down on the surface of agitated water with a yard stick tied to a rope and which is swaying in the wind.

Arpad Elo

Contents

Abstract

The Elo rating system, which was originally proposed by Arpad Elo for chess, has become one of the most important rating systems in sports, economics and gaming nowadays. Its original formulation is based on two-player zero-sum games, but it has been adapted for team sports and other settings. In 2015, Junca and Jabin proposed a kinetic version of the Elo model, and showed that under certain assumptions the ratings do converge towards the players' strength. In this paper we generalise their model to account for variable performance of individual players or teams. We discuss the underlying

modelling assumptions, derive the respective formal mean-field model and illustrate the dynamics with computational results.

3.1 Introduction

Rating systems have become an indispensable tool to rank unobservable quantities, such as a players' strength based on observations, for example outcomes of games. Rating models were originally developed for sports; but are nowadays also used in gaming and financial markets. The Elo-rating system [75] is one of the most prominent rating systems – it is used in chess and other two-player zero sum games. Versions of the Elo-rating have been adopted for many other sports, for example basketball and football, see [188, 204]. Other prominent rating systems include the Glicko rating system or Trueskill, see [93, 110]. Elo and Glicko are based on two-player zero sum games (here a player can be a single individual or an entire team), while Trueskill is used in multi-player situations, as for example in online gaming, see [110, 163].

Elo himself tried to confirm the validity of the proposed rating system using statistical experiments [75]. It was not until 2014 that Jabin and and Junca [121] showed the convergence of ratings towards the players' strength for a continuous kinetic version of the model. Junca [125] later analysed the convergence of discrete ratings in Robin-round tournament, in which players compete against all others in a round and discrete ratings are updated after each such round. However, in this model the players' strength did not change in time. Düring et al. proposed a generalisation in [71], in which players improve and loose skills based on the outcome of games as well as daily performance fluctuations. A simpler but related learning mechanism was proposed by Krupp in [141].

Kinetic models have been used very successfully to describe the behaviour of large interacting agent systems in economics and social sciences. In all these applications interactions between agents – such as encounters in games, the trading of goods or the exchange of opinions – are modelled via binary 'collisions'. Toscani [215] was the first to introduce kinetic models in the context of opinion formation. His ideas were later generalised for more complex opinion dynamics [7, 9, 29, 59, 68, 69, 72, 180], or in the context of wealth distribution [70, 179] or knowledge growth in societies [40, 41]. For a general overview on interacting multi-agent systems and kinetic equations we refer to the book of Pareschi and Toscani [178].

The kinetic formulation of the Elo-model by Jabin and Junca assumes that each player is characterised by a constant strength ρ (being an unobservable quantity) and a rating R, which changes based on the outcome of games. After each match between player i and j their respective ratings R_i and R_j are updated as follows

$$\begin{aligned} R_i^* &= R_i + \gamma(S_{ij} - b(R_i - R_j)), \\ R_j^* &= R_j + \gamma(-S_{ij} - b(R_j - R_i)). \end{aligned} \tag{3.1}$$

Here b is an odd, monotone, increasing function, usually chosen as $b(z) = \tanh(\nu z)$ with a scaling constant $\nu \in \mathbb{R}^+$. The parameter γ controls the speed of adjustment. The outcome of the game is given by the random variable S_{ij}, which takes the values $\{-1, 1\}$, corresponding to a win or loss (other, more fine grained outcomes like a tie can be added in a natural way). It is assumed to equal the expectation of $b(\rho_i - \rho_j)$, that is

$$\langle S_{ij} \rangle = \langle b(\rho_i - \rho_j) \rangle,$$

where ρ_i, ρ_j are the underlying unobservable players' strength. Note that the interactions (3.1) are invariant with respect to translations and both the rating update (3.1) and the expected game outcome S_{ij} depend only on the difference in ρ and R, respectively, so these variables are defined on $\mathbb{R}$.

Jabin and Junca then derived the corresponding macroscopic model for the distribution of players $f(t, r, \rho)$ with respect to their rating r and their strength ρ:

$$\frac{\partial}{\partial t} f(t, \rho, r) + \frac{\partial}{\partial r}(a[f] f(t, \rho, r)) = 0 \tag{3.2}$$

with

$$a[f] = \int_{\mathbb{R}^3} w(r - r')(b(\rho - \rho') - b(r - r')) f(t, \rho', r') d\rho' dr'$$

and initial condition $f(0, \rho, r) = f^0(\rho, r)$. Here, the even probability distribution w was introduced, to account for ranking dependent pairings in tournaments. If $w \equiv 1$ we consider a so-called *all-play-all* game. If w has compact support only teams with close ratings compete. Possible choices for w are

$$w(r - r') = e^{\frac{\log 2}{1+(r-r')^2}} - 1 \quad \text{or} \quad w(r - r') = \chi_{\{|r-r'| \leq c\}}.$$

where χ denotes the indicator function (or smoothed variants thereof) and $c > 0$ is the maximal rating difference between paired competitors. If $w > 0$ Jabin and Junca [121] showed that solutions to (3.2) concentrate on the diagonal, providing the proof that the ratings indeed converge to the underlying strength.

In this work we propose a generalisation of the Elo-model for teams of players with fluctuating strengths. Our main contributions are the following

- We propose and analyse an Elo-rating for teams, which includes stochastic variations in the team strength due to changes in the player setup.
- We formally derive the respective Fokker-Planck equations and analyse their behaviour for long times.
- We investigate the behaviour of solutions in the special case of competing teams whose players' strengths are distributed with a similar variance.
- We illustrate the behaviour of the micro- and macroscopic models with computational experiments, consolidating and extending the analytical results.

This work is organised as follows: we propose a microscopic generalisation of the well-known Elo-rating to teams of players and illustrate the behaviour with microscopic simulations in Section 3.2. Section 3.3 focuses on the corresponding formally derived macroscopic model and its analysis. Next we investigate the model in the case of homogeneous teams in Section 3.4 and report results of computational experiments. Section 3.5 concludes.

3.2 A microscopic Elo-type rating for teams

We start by proposing a microscopic version of the Elo-rating for players with variable strength, which can also be used in the context of teams.

3.2.1 Performance variations in teams and individual players

In the following we consider a microscopic model, which accounts for performance fluctuations in teams as well as individuals. These fluctuations may be caused by varying individual or team performance (due to different line-ups) or for example by card luck. We recall that small performance fluctuations in the individual strength ρ were modelled in [71] by stochastic fluctuations in the strength. We will follow a different approach and replace the constant strength ρ by a random variable λ_ρ defined on

a set of possible outcomes Ω_ρ, which can be a finite set as well as an interval. This then allows us to define the stochastic process $\{\lambda_\rho(t)\}_{t\in\mathbb{R}^+}$, whose expected value and variance will be denoted by $\theta := \langle\lambda_\rho\rangle$, and $\sigma^2 := \mathrm{Var}[\lambda_\rho]$, respectively.

We consider competing teams T_i, T_j instead of individual players. The corresponding expected value θ can be interpreted as the mean strength of the team with a chosen line-up, i.e. a subset of the team's players who will be playing in a particular game. We assume similar as in [121], that the expected outcome of the game between T_i, T_j depends on the difference of teams' strengths through b:

$$\langle S_{ij}\rangle = \langle b(\lambda_{\rho_i} - \lambda_{\rho_j})\rangle. \tag{3.3}$$

If two teams T_i and T_j with ratings R_i and R_j meet, their ratings and strength after the game can be updated using again (3.1) where γ is a scaling constant controlling the speed of adjustment. It is usually chosen much smaller than the rating scores, in the hope that a player's rating slowly converges to its underlying strength. As discussed in the introduction we make the following assumption on b:

(B) The function b is $C^3(\mathbb{R})$, monotonically increasing, bounded, odd and Lipschitz.

Since b is non-linear the expected value and b cannot be interchanged. To calculate the expected value of S_{ij} in (3.3) we use the *Law of the unconscious statistician* [24], e.g. in the discrete case we obtain

$$\langle S_{ij}\rangle = \sum_{x_i\in\Omega_{\rho_i}}\sum_{x_j\in\Omega_{\rho_j}} b(x_i - x_j)\tilde{p}(x_i, x_j) = \sum_{x_i\in\Omega_{\rho_i}}\sum_{x_j\in\Omega_{\rho_j}} b(x_i - x_j)p(x_i)p(x_j), \tag{3.4}$$

where $\tilde{p}$ denotes the probability of a possible line up x_i playing against a line up x_j and the second equality holds if this happens independently of each other. In the following we always assume this independence of the stochastic processes for team T_i and T_j.

We can Taylor-expand $\langle S_{ij}\rangle$ in (3.4) as described, for example, in [18]. Since we have $\langle\lambda_{\rho_i} - \lambda_{\rho_j}\rangle = \theta_i - \theta_j$ and $\mathrm{Var}[\lambda_{\rho_i} - \lambda_{\rho_j}] = {\sigma_i}^2 + {\sigma_j}^2$, it follows:

$$\begin{aligned}\langle S_{ij}\rangle = \langle b(\lambda_{\rho_i} - \lambda_{\rho_j})\rangle &\approx b(\theta_i - \theta_j) + \frac{1}{2}b''(\theta_i - \theta_j)({\sigma_i}^2 + {\sigma_j}^2)\\ &=: b(\theta_i - \theta_j) + K(\theta_i - \theta_j, \sigma_i, \sigma_j).\end{aligned} \tag{3.5}$$

Note that the function K is odd in the first argument and even in the other two. Similarly, the following holds for the variance

$$\mathrm{Var}[S_{ij}] \approx (b'(\theta_i - \theta_j))^2({\sigma_i}^2 + {\sigma_j}^2). \tag{3.6}$$

3.2.2 Microscopic simulations

In the following we will illustrate the behaviour of the microscopic model with various simulations. We consider N teams $T_1 \dots T_N$; each team has M players with strengths ρ_{i_k} from which $m < M$ distinct players are selected as line-up for each match. Let $\vec{\rho}_i = (\rho_{i_1}, \dots, \rho_{i_M})$ denote the vector of all players in a team T_i. We assume without loss of generality that the vector $\vec{\rho}_i$ is ordered.

Let us consider first the case that the m players for the line-up are chosen from the set of M players uniformly. This can be done by generating $\binom{M}{m}$ normalised vectors $\vec{\lambda}_{i_k} \in \{0,1\}^M$ with $|\vec{\lambda}_{i_k}| = 1$. Then the stochastic process λ^t selects each vector $\vec{\lambda}_{i_k}$ with equal probability and we have

$$P(S_{ij} = 1) = b(\vec{\lambda}_{i_k}\cdot\vec{\rho}_i - \vec{\lambda}_{j_k}\cdot\vec{\rho}_j),$$

for a match between T_i and T_j. More realistic line-up selection would choose players directly proportional to their strength. We recall that the Elo-rating is translation invariant, hence we shift the expected values θ to the interval $[0, 10]$ in the following.

As a first example consider the following football-inspired situation of $N = 200$ teams with $M = 23$ players each from which $m = 11$ players are selected per match. For any team T_i we then have $\theta_i = \frac{11}{23}\sum \rho_{i_k}$. We investigate two different initial setups for the teams:

($R1$) For every team T_i, $i = 1, \dots N$, the players' strengths ρ_{i_k}, $k = 1, \dots 23$, is chosen randomly from the interval $\frac{1}{11}[5 - \frac{5}{200}(i-1), 5 + \frac{5}{200}(i-1)]$. That is $\rho_{1_1} = \dots \rho_{1_{23}} = \frac{1}{11}5$ and $\rho_{200_k} \in \frac{1}{11}[0, 10]$ for every k. In other words all teams have an approximate team strength of $\theta_i \approx 5$ with increasing variance σ_i^2 as can be seen in Figure 3.1a.

($R2$) For every team T_i, $i = 1, \dots N$, the players' strengths ρ_{i_k} are given by

$$\frac{1}{11}(4 + \frac{6(i-1)}{197} + \eta_{i_k}), \quad k \in \{1, \dots, 23\}, \quad \eta_{i_k} \in \mathcal{N}(0, 1).$$

The mean team strength of the first 198 teams is increasing from values around 4 to values around 10 and the variances σ_i^2 are of the same order. In addition we consider two teams, Germany ($i = 199$) and Brazil ($i = 200$), whose mean value and variance are motivated by the 2014 FIFA World Cup results, see [2]. We scale those values to $\theta_{\text{Ger}} = 10$ as well as $\theta_{\text{Bra}} = 9$. However, we do not scale the variance - it is signficantly higher in the generated data set, as can be seen in Figure 3.1b.

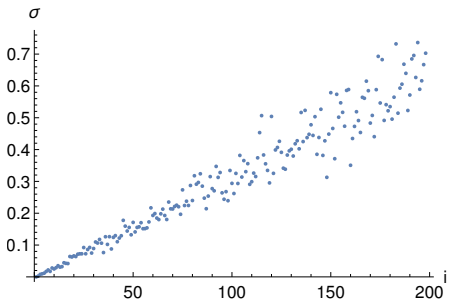

(a) The standard deviation σ for every team T_i based on rule ($R1$).

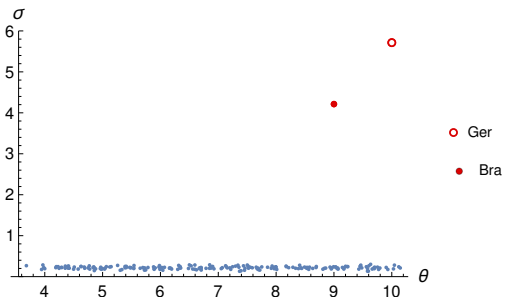

(b) The standard deviation σ regarding θ based on rule ($R2$).

Figure 3.1: The standard deviation of the two setups visualised, both calculated over 10^4 Monte Carlo experiments per team.

We carry out direct Monte Carlo simulation using Bird's scheme, see [178], for these two initial setups. We choose time steps of $\Delta t = 0.1$ and perform 25 matches per time step. The results were then averaged over 50 realisations after $2 \cdot 10^6$ time-steps. Figure 3.2 shows the final distribution of teams for the two different initial setups. In Figure 3.2a we see clustering around the point $(\theta, R) = (5, 5)$ as expected for setup ($R1$). However, an interesting phenomenon is that teams with $\theta < 5$ consistently under-perform and conversely $\theta > 5$ over-perform, as they lie above and below the line $\theta = R$, respectively. In Figure 3.2b, we see convergence towards a steady state for the 198 teams created using the rule ($R2$). However, this straight line has a steeper slope than $\theta = R$. Furthermore, the German and Brazilian team are clear outliers, both are under-performing relative to their strengths.

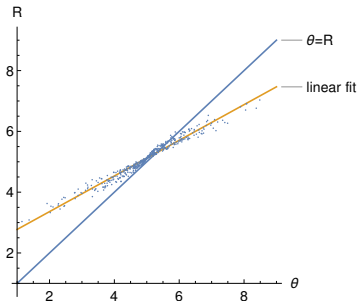

(a) Setup (R1) with increasing variance in the team performance.

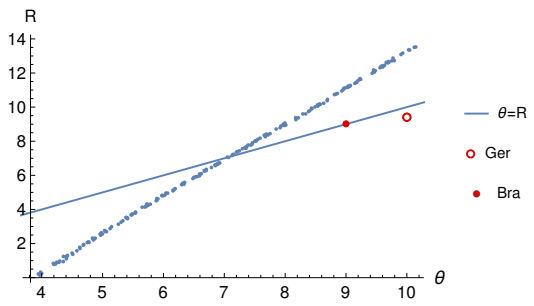

(b) Setup (R2) with constant variance $\sigma = 1$ in the team performance.

Figure 3.2: Stationary team distribution for setup (R1) and (R2).

3.3 A macroscopic Elo-model for teams

In general, the expected value θ and variance σ^2 of the microscopic model (3.1) are finite since they result from discrete, finite random processes. Compared to the formal derivation of the macroscopic model in previous works [121, 141], we need additional assumptions on the moments of σ because of the unboundedness of K in (3.5) in the 2nd and 3rd argument when passing from micro to macro.

Let $f(t, \theta, \sigma, r)$ be the distribution of teams at time t with expected team performance θ, variance σ^2 and rating r. The derivation of the macroscopic model (3.7) below is based on the following assumptions:

(A1) Let $f^0 \in H^1(\mathbb{R}^3)$ with $f^0 \geq 0$ and having compact support. Furthermore, we assume:

$$\int_{\mathbb{R}^3} f^0(\theta,\sigma,r)d\theta d\sigma dr = 1, \quad \int_{\mathbb{R}^3} Rf^0(\theta,\sigma,r)d\theta d\sigma dr = 0, \quad \int_{\mathbb{R}^3} \theta f^0(\theta,\sigma,r)d\theta d\sigma dr = 0,$$
$$\int_{\mathbb{R}^3} \sigma f^0(\theta,\sigma,r)d\theta d\sigma dr = 1, \quad \int_{\mathbb{R}^3} \sigma^2 f^0(\theta,\sigma,r)d\theta d\sigma dr = C_{\sigma^2}.$$

(A2) Let the interaction rate function $w \geq 0$ be an even function with $w \in C^2(\mathbb{R}^3) \cap L^\infty(\mathbb{R}^3)$.

In Appendix 3.6 we derive the following macroscopic Fokker-Planck equation for the distribution of teams $f = f(t, r, \theta, \sigma)$:

$$\begin{aligned} \frac{\partial}{\partial t} f(t,\theta,\sigma,r) + \frac{\partial}{\partial r}(a[f]f(t,\theta,\sigma,r)) &= 0, \qquad \text{in } [0,T) \times \mathbb{R}^3, \\ f(t=0,\theta,\sigma,r) &= f^0(\theta,\sigma,r), \qquad \text{in } \mathbb{R}^3, \end{aligned} \tag{3.7}$$

with

$$a[f] = \int_{\mathbb{R}^3} w(r-r')(b(\theta-\theta') + \frac{1}{2}b''(\theta-\theta')(\sigma^2+\sigma'^2) - b(r-r'))f(t,\theta',\sigma',r')\,d\theta' d\sigma' dr'.$$

Here b'' is the second derivative introduced in (3.5). We note that the operator $a[\cdot]$ includes an additional correction term resulting from the variance of the distribution of strengths. This term's sign depends on the sign of $\theta - \theta'$, either decreasing or increasing the adjustment of ratings. This is consistent with the under- and over-performance of teams observed in the microscopic simulations in Section 3.2.3.2.2.

3.3.1 Analysis of the Fokker-Planck equation

Since b and b'' are odd, the total mass is conserved as

$$\frac{\partial}{\partial t}\int_{\mathbb{R}^3} f(t,\theta,\sigma,r)\,d\theta d\sigma dr = 0.$$

and therefore $\int_{\mathbb{R}^3} f(t,\theta,\sigma,r)\,d\theta d\sigma dr = \int_{\mathbb{R}^3} f^0(\theta,\sigma,r)\,d\theta d\sigma dr = 1$ for all times $t > 0$.

Next, we show the existence of a classical solution to (3.7) following arguments from [19, 203].

Theorem 3.1. *Assume that the initial datum f^0*

1. *is compactly supported in the phase space, i.e. $\operatorname{supp}_{(r,\theta,\sigma)} f^0$ is bounded,*
2. *is C^1-regular and bounded:*

$$\sum_{0\le|\alpha|\le 1} \left\|\nabla_r^\alpha f^0\right\|_{L^\infty} < \infty.$$

Then, for any $t \in (0,\infty)$, there exists a unique classical solution $f \in C^1([0,t)\times\mathbb{R}^3)$ to (3.7).

Proof. In the following we consider the 'all play all' setting, that is $w \equiv 1$; our arguments can, however, be generalised for interaction functions w satisfying *(A2)*. We start by showing that the solution cannot blow up in finite time. Next we prove local in time existence based on a priori estimates and a fixed point argument. Global existence follows from a continuation argument using energy estimates.

First we show that the local solution f remains uniformly bounded. We rewrite (3.7) in a non-conservative form,

$$\frac{\partial}{\partial t}f(t,\theta,\sigma,r) + a[f]\frac{\partial}{\partial r}f(t,\theta,\sigma,r) = -f(t,\theta,\sigma,r)\frac{\partial}{\partial r}a[f],$$

where we have

$$-f(t,\theta,\sigma,r)\frac{\partial}{\partial r}a[f] = f(t,\theta,\sigma,r)\int_{\mathbb{R}^3} b'(r-r')f(t,\theta',\sigma',r')\,d\theta' d\sigma' dr',$$

which yields

$$\left\|\frac{\partial}{\partial r}a[f]\right\|_{L^\infty} \le L,$$

where L is the Lipschitz constant of b and we used that the total mass equals one. Next we consider a trajectory starting at time $\tau_0 \in \mathbb{R}^+$ in (r_0,θ_0,σ_0), then the characteristics are given by

$$\frac{\partial}{\partial t}r(t) = a[f], \qquad \frac{\partial}{\partial t}\theta(t) = \frac{\partial}{\partial t}\sigma(t) = 0.$$

Therefore,

$$\frac{\partial}{\partial t}f(t,\theta,\sigma,r) \le Lf(t,\theta,\sigma,r),$$

and Gronwall's lemma gives

$$\|f(t)\|_{L^\infty} \le e^{Lt}\left\|f^0\right\|_{L^\infty}.$$

Hence, the solution cannot blow up in finite time.

We continue with the existence of a local solution following Theorem 3.1 in [19]. To this end we investigate the non-linear transport operator $\mathcal{H}$:

$$\mathcal{H}(f) = -f(t,\theta,\sigma,r)\frac{\partial}{\partial r}a[f], \qquad \text{with } \mathcal{H} := \frac{\partial}{\partial t} + a[f]\frac{\partial}{\partial r},$$

in the following. There exist positive constants C_1, C_2 such that

$$\begin{aligned} &|\mathcal{H}(f)| \leq \left\|b'\right\|_{L^\infty} |f| = C_1|f|, \\ &|\mathcal{H}(\frac{\partial}{\partial r}f)| \leq |f|\left\|b''\right\|_{L^\infty} + \left|\frac{\partial}{\partial r}f\right| \left\|b'\right\|_{L^\infty} = C_2(|f| + \left|\frac{\partial}{\partial r}f\right|), \end{aligned} \tag{3.8}$$

because of b being Lipschitz and therefore we have L_∞ bounds for its derivatives. Moreover, the map H defined by

$$H : C^1([0,t)\times\mathbb{R}^3) \to C^1([0,t)\times\mathbb{R}^3), \quad f \mapsto (\mathcal{H})^{-1}(-f\frac{\partial}{\partial r}a[f])$$

is bounded since we can use the estimates (3.8) together with the bounded inverse theorem. Next we consider the solution along the trajectories $(\theta(t),\sigma(t),r(t))$

$$f(t,\theta(t),\sigma(t),r(t)) = f(0,\theta_0,\sigma_0,r_0) + \int_0^t \frac{\partial}{\partial r}\Big(a[f(t,\theta(t),\sigma(t),r(t))]f(t,\theta(t),\sigma(t),r(t))\Big)dt.$$

We can then use the previous estimates to choose a $t > 0$ such that H is a contraction. Using Banach's fixed point theorem we obtain a unique local solution $f \in C^1([0,t]\times\mathbb{R}^3)$. Let $\mathcal{F}$ be the $W^{1,\infty}$-norm of $f(t)$,

$$\mathcal{F}(t) = \sum_{0\leq|\alpha|\leq 1} \left\|\nabla_r^\alpha f(t)\right\|_{L^\infty}.$$

Using (3.8) and again Gronwall's lemma we get

$$\frac{\partial}{\partial t}\mathcal{F}(t) \leq C_3\mathcal{F}(t)$$

and therefore we have the upper bound

$$\mathcal{F}(t) \leq \mathcal{F}(0)e^{C_3 t}, \qquad \forall t\in[0,T).$$

The energy bound in $W^{1,\infty}$ allows us to use the standard continuation principle, giving the global extension of the local solution. □

We continue by analysing the behaviour of the moments of f. We define the s-th moment for $s\in\mathbb{N}$ with respect to r (and similar the moments with respect to θ,σ),

$$m_{s,r}(t) = \int_{\mathbb{R}^3} r^s f\, d\theta dr d\sigma.$$

The evolution with respect to σ and θ is trivial, as the function does not change with respect to these variables. The evolution of the second moment w.r.t. to r satisfies:

$$\begin{aligned}
&\frac{d}{dt}\int_{\mathbb{R}^3} r^2 f\, d\theta dr d\sigma = -\int_{\mathbb{R}^3} r^2 \frac{d}{dr}(a[f]f)\, d\theta dr d\sigma \\
&= 2\int_{\mathbb{R}^6} rw(r-r')\Big(b(\theta-\theta') + \frac{\sigma^2+\sigma'^2}{2}b''(\theta-\theta') - b(r-r')\Big) f f'\, d\theta' dr' d\sigma' d\theta dr d\sigma \\
&= -\int_{\mathbb{R}^6} rb(r-r')w(r-r')f' f\, d\theta' dr' d\sigma' d\theta dr d\sigma - \int_{\mathbb{R}^6} r'b(r'-r)w(r'-r)f' f\, d\theta' dr' d\sigma' d\theta dr d\sigma \\
&\quad + 2\int_{\mathbb{R}^6} rw(r-r')(b(\theta-\theta') + \frac{\sigma^2+\sigma'^2}{2}b''(\theta-\theta'))f f'\, d\theta' dr' d\sigma' d\theta dr d\sigma \\
&= -\int_{\mathbb{R}^6} (r-r')b(r-r')w(r-r')f f'\, d\theta' dr' d\sigma' d\theta dr d\sigma \\
&< 0.
\end{aligned} \tag{3.9}$$

Here, we used the short-hand notation $f' = f(t,\theta',\sigma',r')$. Furthermore, we used that for $r - r' < 0$ the function $b(r-r') < 0$ is negative, since b is odd and monotonically increasing. The latter does not hold in general for $b + b''$, however, the second integral vanishes since the integrand is still odd in θ and r. Therefore, the second moment in r decreases over time and we expect convergence towards a stationary state. Our computational experiments confirm this expected convergence. However, we are not able to compute these stationary states explicitly as it was done in [121].

3.3.2 Numerical results for the macroscopic model

We perform several computational experiments illustrating the dynamics of (3.7) using a finite difference scheme. It is based on the generalisation of a finite difference scheme for conservation laws with discontinuous flux presented by Towers in [218]. This generalisation is straight-forward, as (3.7) has only transport in r direction. Let $f^n_{j,l,m}$ denote the solution at the discrete points $(j\Delta r, l\Delta\theta, m\Delta\sigma)$, $j,l,m \in \mathbb{N}$, and time $t^n = n\Delta t$, $n \in \mathbb{N}$, with discrete positive increments $\Delta r, \Delta\theta$, $\Delta\sigma$ and Δt. Then the explicit scheme reads as follows:

$$f^{n+1}_{j,l,m} = f^n_{j,l,m} - \frac{\Delta t}{\Delta r}(a^n_{j+1/2,l,m}h^n_{j+1/2,l,m} - a^n_{j-1/2,l,m}h^n_{j-1/2,l,m}),$$

with cell averages $a^n_{j+1/2,l,m} = \frac{1}{\Delta r}\int_j^{j+1} a[f^n(r, l\Delta\theta, m\Delta\sigma)]\, dr$. The function h is chosen depending on the sign of the averaged flux (as in the usual Godunov scheme) that is

$$h^n_{j+1/2,l,m} = \begin{cases} f^n_{j,l,m}, & a^n_{j+1/2,l,m} \geq 0, \\ f^n_{j+1,l,m}, & a^n_{j+1/2,l,m} < 0. \end{cases}$$

In Figure 3.3 we visualise the first marginals $\int_{\mathbb{R}} f(t,r,\theta,\sigma)\, d\sigma$ and $\int_{\mathbb{R}} f(t,r,\theta,\sigma)\, d\theta$ of the team distribution at time $t = 5$ using timesteps of size $\Delta t = 10^{-5}$ and $\nu = 1$. The computational domain is $\Omega = [0,10]\times[0,10]\times[0,1]$ and the spatial discretisation was set to $\Delta r = \Delta\theta = \Delta\sigma = 5\cdot 10^{-2}$, the initial distribution of teams uniform and normalised. The left plot in Figure 3.3 shows that ratings converge towards the mean strength for $\theta \in [6,8]$, but are blurred for smaller and larger means. We observe a similar over- and under-performance as in the microscopic simulations in Figure 3.2b. The right plot illustrates the decrease of $m_{2,r}$ in the direction θ. The larger the uncertainty σ, the less accurate the ratings as all teams get a similar rating (around 7).

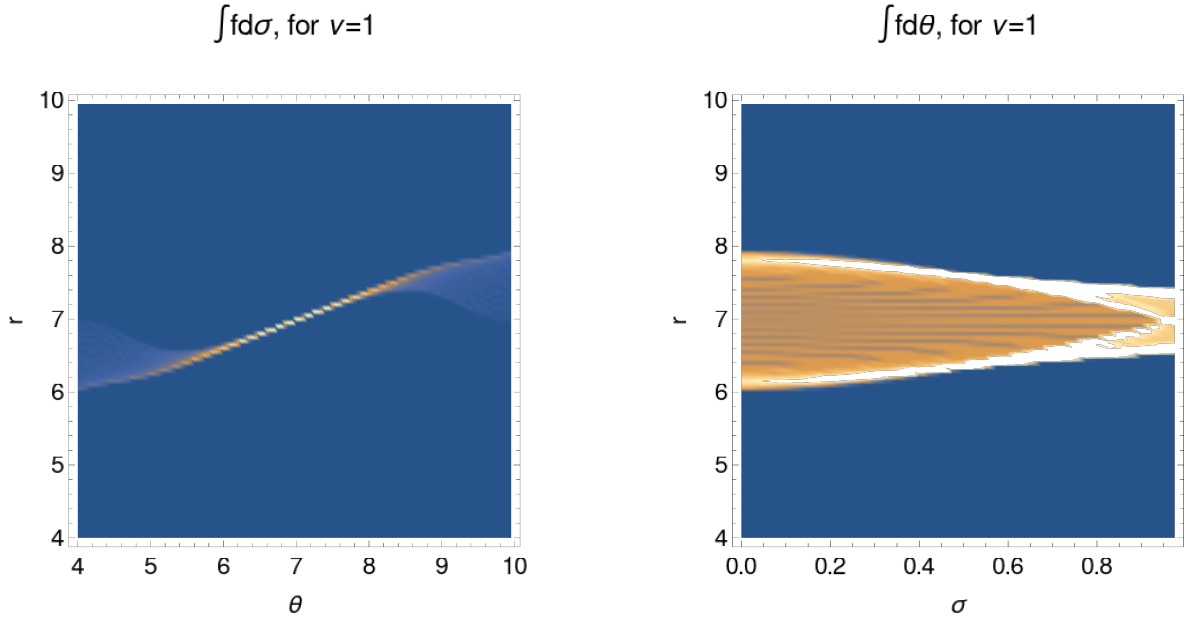

Figure 3.3: Second and third marginal of the team distribution f at time $t = 5$ for $f^0 = 1$.

3.4 Special scaling limits and homogeneous player distributions

Our microscopic computational results suggest that if all teams have the same player variance, then the ratings converge to the underlying mean team strength. In this case, however, the integral over σ can be seen as a point evaluation and we can simplify (3.7) for constant $\sigma \in \mathbb{R}_0^+$:

$$\begin{aligned} \frac{\partial}{\partial t} f(t,\theta,r) + \frac{\partial}{\partial r}(a[f]f(t,\theta,r)) &= 0 \\ f(t=0,\theta,r) &= f^0(\theta,r), \end{aligned} \tag{3.10}$$

with a changed to

$$a[f] = \int_{\mathbb{R}^2} w(r-r')(b(\theta-\theta') + \sigma^2 b''(\theta-\theta') - b(r-r'))f(t,\theta',r')dr'd\theta'.$$

We discuss the existence of a unique solution and the analysis of the moments. Furthermore we consider the relative energy to prove convergence of the team strengths to ratings. The existence of a classical solution itself follows from the same arguments as in Theorem 4.10.

Theorem 3.2. *Assume that the initial datum f^0*

1. *is compactly supported in the phase space, i.e. $\operatorname{supp}_{(r,\theta)} f^0$ is bounded*
2. *is C^1-regular and bounded:*

$$\sum_{0\le|\alpha|\le 1} \left\| \nabla_r^\alpha f^0 \right\|_{L^\infty} < \infty.$$

Then, for any $T \in (0,\infty)$, there exists a unique classical solution $f \in C^1([0,T)\times\mathbb{R}^2)$ to (3.10).

The proof of Theorem 4.11 can be easily adapted from the proof of Theorem 4.10 and is omitted here. Equation (3.10) is conservative, hence the total mass is preserved, and the moments with respect to θ is zero. Again, the second moment w.r.t. to r is decreasing (using similar arguments as in (3.9)):

$$\begin{aligned}\frac{d}{dt}\int_{\mathbb{R}^2} r^2 f\, d\theta dr &= -\int_{\mathbb{R}^2} r^2 \frac{d}{dr}(a[f]f)\, d\theta dr d\theta' dr' \\ &= -\int_{\mathbb{R}^4} (r-r')(b(\theta-\theta')+\sigma^2 b''(\theta-\theta'))w(r-r')ff'\, d\theta' dr' d\theta dr < 0,\end{aligned}$$

using the short hand notation $f' = f(t,\theta',r')$.

The ratio of ν and σ is important in order to be able to show the convergence of the team ratings to the average strength. This is the case under following assumption:

(B') $b+\sigma^2 b''$ is monotonically increasing.

Note that (B') holds for example for $b(z) = \tanh(\nu z)$ if $1+\nu^2\sigma^2(4-6\,\mathrm{sech}(z\nu)^2) > 0$. Then we can use similar arguments as Jabin and Junca [121], who considered the relative energy

$$\mathcal{E}(t) = \int_{\mathbb{R}^2} (r-\theta)^2 f(t,\theta,r)\, dr d\theta.$$

In the following we will show that

$$\frac{d\mathcal{E}(t)}{dt} < 0.$$

We calculate:

$$\begin{aligned}\frac{d}{dt}\int_{\mathbb{R}^2} (r-\theta)^2 f\, d\theta dr &= -\int_{\mathbb{R}^2} (r-\theta)^2 \frac{d}{dr}(a[f]f)\, d\theta dr d\theta' dr' \\ &= -\int_{\mathbb{R}^4} (r-r')b(r-r')w(r-r')ff'\, d\theta' dr' d\theta dr \\ &\quad -\int_{\mathbb{R}^4} (\theta-\theta')(b(\theta-\theta')+\sigma^2 b''(\theta-\theta'))w(r-r')ff'\, d\theta' dr' d\theta dr < 0.\end{aligned}$$

For $r-r' < 0$ we have $b(r-r') < 0$, while the opposite holds true for $(r-r') > 0$. Because of (B') the second term is positive, yielding the stated energy decay.

Assumption (B) together with (B') gives us bounds for b''', whereas we can deduce b'' being Lipschitz, too, with constant L_2. Following the arguments in Jabin and Junca, [121], we obtain:

Theorem 3.3. *Let f^0 be as in Theorem 4.11 and $w \geq w_{min} > 0$ on $\mathrm{supp} f^0$. Then*

$$\mathcal{E}(t) \leq \mathcal{E}(0)\exp(-2w_{min}(L+\sigma^2 L_2)t),$$

where L, L_2 depend on b, b'' (and therefore ν) and on $\mathrm{supp} f^0$.

Proof. The proof is along the lines of [121, 141], adapted for the additional term related to b''. We define

$$\mathcal{D}(f(t)) := \int_{\mathbb{R}^4} (r - r' - \theta + \theta') w(r - r')[b(\theta - \theta') + \sigma^2 b''(\theta - \theta') - b(r - r')] f f' \, dr' d\theta' dr d\theta,$$

and by our previous calculations we have that $-\mathcal{D}(f(t)) = \frac{d\mathcal{E}(t)}{dt} \leqslant 0$. Using similar symmetry arguments as before we deduce that

$$-\int_{\mathbb{R}^4} (r - r') w_{min} \sigma^2 b''(r - r') f f' \, d\theta' dr' d\theta dr < 0.$$

We now split the integrands of $\mathcal{D}$ to obtain

$$\begin{aligned}\mathcal{D}(f(t)) \geq & \int_{\mathbb{R}^4} (r - r' - \theta + \theta') w_{min}[b(\theta - \theta') - b(r - r')] f f' \, dr' d\theta' dr d\theta \\ & + \int_{\mathbb{R}^4} (r - r' - \theta + \theta') w_{min} \sigma^2 [b''(\theta - \theta') - b''(r - r')] f f' \, dr' d\theta' dr d\theta.\end{aligned}$$

Using that b, b'' are Lipschitz and odd we have

$$\begin{aligned}(r - r' - \theta + \theta') w_{min}[b(\theta - \theta') - b(r - r')] &\geq L w_{min} |r - r' - \theta + \theta'|^2 \\ (r - r' - \theta + \theta') w_{min} \sigma^2 [b''(\theta - \theta') - b''(r - r')] &\geq \sigma^2 L_2 w_{min} |r - r' - \theta + \theta'|^2.\end{aligned}$$

Therefore, it follows that

$$\mathcal{D}(f) \geqslant \int_{\mathbb{R}^4} (L + \sigma^2 L_2) w_{min} |r - r' - \theta + \theta'|^2 f' f \, dr' d\theta' dr d\theta.$$

We assume w.l.o.g. (due to the translation invariance of the model)

$$\int_{\mathbb{R}^2} r f(t, r, \theta) \, dr \, d\theta = \int_{\mathbb{R}^2} \theta f(t, r, \theta) \, dr d\theta = 0$$

which gives

$$\int_{\mathbb{R}^4} (r - \theta)(r' - \theta') \, f' f \, dr' dr d\theta' d\theta = 0.$$

Then we can deduce

$$\mathcal{D}(f) \geqslant 2(L + \sigma^2 L_2) w_{min} \int_{\mathbb{R}^2} |r - \theta|^2 \, f dr \, d\theta$$

and altogether

$$-\mathcal{D}(f) = \frac{d\mathcal{E}(t)}{dt} \leqslant -2 L w_{min} \int_{\mathbb{R}^2} |r - \theta|^2 \, f \, dr \, d\theta = -2 w_{min}(L + \sigma^2 L_2) \mathcal{E}(t).$$

Using Gronwall's lemma we conclude the proof as in [121, 141]. □

We conclude by underpinning our analytical results with numerical simulations.

Micro- and macroscopic simulations. For the microscopic simulation we consider $N = 500$ players with fixed mean strengths θ_n, chosen uniformly distributed in $[4, 10]$. In every time-step we then choose $\mathcal{N}(\theta_n, \sigma)$ distributed values for the evaluation of S_{ij}. We set $\nu = 0.5$ and simulate 10^6 time-steps of $\Delta t = 0.1$ and 25 collisions per time-step over 50 realisations as in the previous simulations described in Section 3.23.2.2. On a macroscopic level, we use the algorithm presented in Section 3.33.3.2 reduced by the dimension in σ.

We see a great agreement between the two models in Figure 3.4 and 3.5. In addition, we clearly see the influence of σ on the ranking as discussed in Figure 3.3. If the variance σ is large, all teams are rated equally, in particular the ratings converge to 7 for all values of θ. Or expressed differently: in expectation weaker teams are over-performing and stronger teams under-performing. We see a similar effect already in our first microscopic simulations in Figure 3.2.
Moreover, the numerical simulations show that ν can be used to balance the variance σ^2 and obtain the desired convergence of ratings to the teams' average strength as discussed in the previous subsection. If assumption (B') holds the long-term behaviour of (3.10) will be similar to the original Elo model (3.2) in [121]. This effect can also be observed on a microscopic level, see Figure 3.6, where we compare the long-term behaviour for $\sigma = 2$ and different values of $\nu \in \{1, 0.1, 0.01\}$. For $\nu = 1$ all expected values $\theta \in [4, 10]$ converge to 7 and we get an almost horizontal line in the long-term run. If we choose $\nu = 0.1$ we get the desired diagonal $\theta = r$ as time increases, as in the case $\nu = 0.01$. However, the smaller value of ν corresponds to a slower convergence towards the stationary state, as can be seen in Figure 3.6, bottom right.

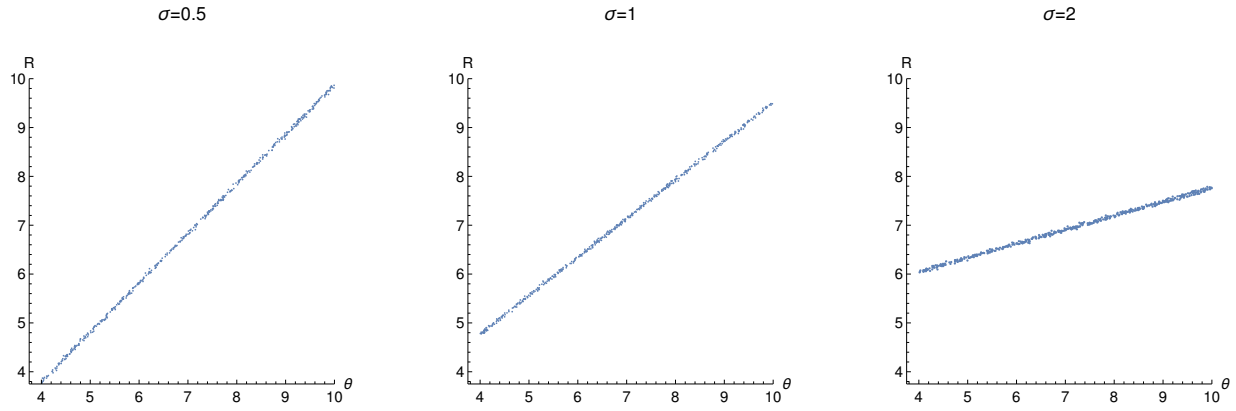

Figure 3.4: Microscopic team distributions for $\nu = 0.5$ and different values of σ.

3.5 Conclusion

In this paper we proposed a generalisation of the Elo-rating model for teams of players with varying strengths, which includes fluctuations in the performance to account for example for variable line-ups in team sports. Based on the microscopic interaction rules we then derived the corresponding kinetic model, proved existence of a solution and analysed different moments of its solution. These analytical insights indicate the formation of non-trivial steady states – a hypothesis that is supported by our numerical results. Furthermore, we considered the special case of similar variance σ^2, which allowed to formally derive a lower dimensional equation. Under further smallness assumptions we could then use techniques from Junca and Jabin, see [121], to show convergence of the rating r to the expected

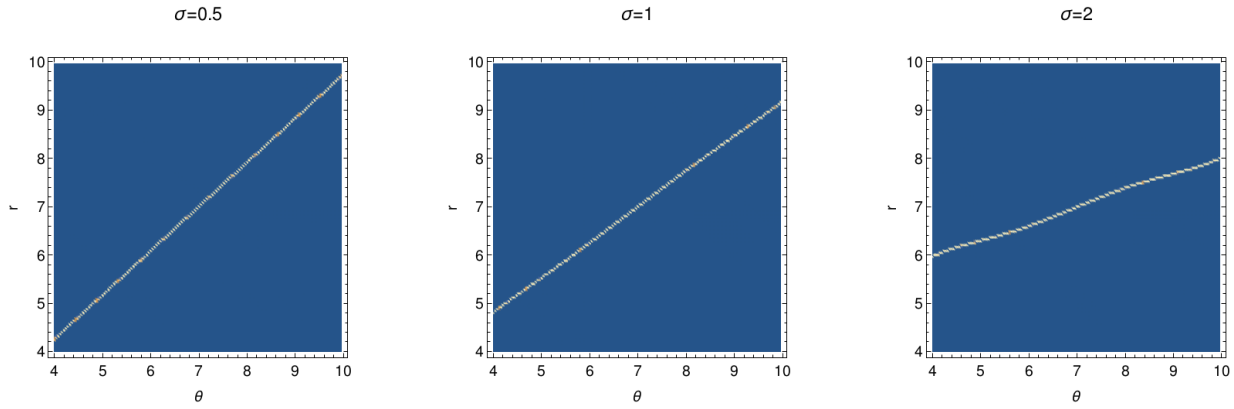

Figure 3.5: Macroscopic results for $\Omega = [4, 10] \times [4, 10]$ for different values of σ and $\nu = 0.5$.

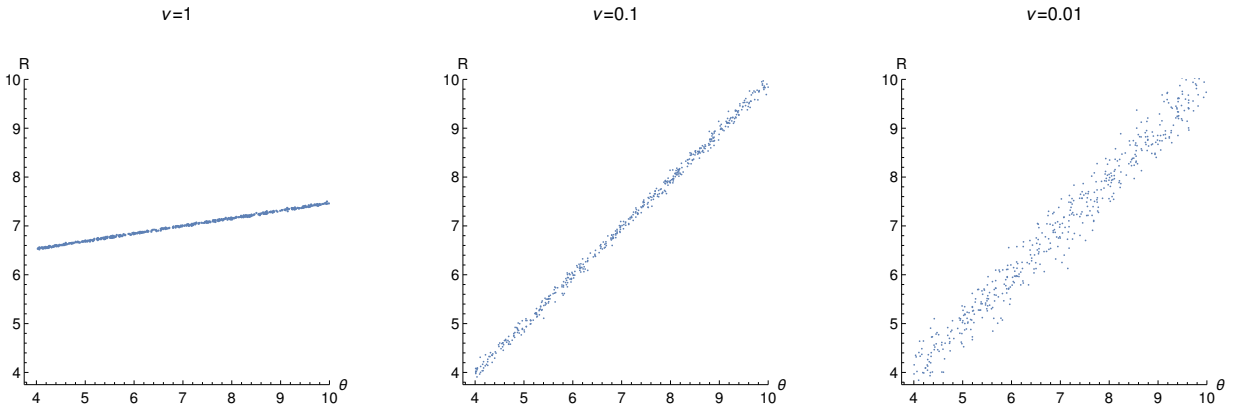

Figure 3.6: A smaller value of ν leads to slower convergence, however, we can retrieve the desired convergence of R to the expected value θ by choosing ν sufficiently small. In all simulations we set $\sigma = 2$.

value θ. The smallness assumption relates to practically relevant parameter values. For example, in chess the scaling parameter ν in b is usually quite small, around $\frac{1}{400}$, as reported in [74, 75, 100]. We were able to show numerically, both at the microscopic and kinetic level, that a large ν leads to the loss of convergence of $r \to \theta$. Choosing ν according to (B'), we obtain the desired convergence and were able to proof this analytically. This effect also occurs at the microscopic level.

Nevertheless, the microscopic simulations showed that a large σ has a strong impact on the ratings. The question therefore remains whether fluctuations in the underlying strength should be included in ρ, see [71], or incorporated in the outcome of the game S_{ij} (as proposed in this paper). Following [71], performance fluctuations could also be included via an additional random term in the microscopic interactions. This leads to a PDE with a diffusive term which is of the following form:

$$\frac{\partial f(r,\theta,t)}{\partial t} = -\frac{\partial}{\partial r}\left(a[f]f(\theta,R,t)\right) + \frac{\sigma^2}{2}d[f]\frac{\partial^2}{\partial \theta^2}f(\theta,r,t),$$

with

$$a[f] = a[f](r,\theta,t) = \int_{\mathbb{R}^2} w(r-r')(b(\theta-\theta') - b(r-r'))f(\theta',r',t)\,d\theta' dr',$$
$$d[f] = d[f](r,\theta,t) = \int_{\mathbb{R}^2} w(r-r')f(r',\theta',t)\,d\theta' dr'$$

where the influence of diffusion is determined by the maximum variance σ^2 of the team strengths.

Accounting for uncertainty in ratings through an additional functional dependence and not via diffusion also happens in the Glicko rating [93], an extension of the Elo rating. However, here the variable σ is the uncertainty of the rating. It is assumed that σ increases if players do not compete and decreases if they participate in tournaments. This microscopic model could similarly be used to derive a continuous kinetic rating model. Another interesting direction of future research is the combination of performance fluctuations with learning effects, as considered in [71, 141].

Contributions and Acknowledgments

The paper has been conceived and is based on work from all three authors. MF obtained the analytical results under guidance from BD and MTW. MF carried out the numerical experiments with support from MTW. All authors worked on and approved the manuscript.

MF acknowledges partial support via the Austrian Science Fund (FWF) project F65. MTW acknowledges partial support via the New Frontier's Project NST-0001 of the Austrian Academy of Sciences ÖAW.

3.6 Appendix

3.6.1 Derivation of the Boltzmann-type equation

We follow the derivation of [71] for the corresponding PDE of Fokker-Planck type to study the dynamics of the corresponding model. We start with the evolution equation for the distribution of teams $f_\gamma = f_\gamma(\theta,\sigma,R,t)$ with respect to their rating R, intrinsic team-strength ρ and the variance σ_i. For a fixed number of teams, N, the interactions (3.1) induce a discrete-time Markov process with N-particle joint probability distribution $P_N(\theta_1,\sigma_1,R_1,\theta_2,R_2,\dots,\theta_N,\sigma_N,R_N,\tau)$. Then we can state the evolution of the first marginal from

$$P_1(\theta,\sigma,R,\tau) = \int P_N(\theta,\sigma,R,\theta_2,\sigma_2,R_2,\dots,\theta_N,\sigma_N,R_N,\tau)d\theta_2 d\sigma_2 dR_2\cdots d\theta_N d\sigma_N dR_N,$$

where τ is the discrete time step using only the one- and two-particle distribution functions [50, 51] in a single time step,

$$\begin{aligned}
&P_1(\theta,\sigma,R,\tau+1) - P_1(\theta,\sigma,R,\tau) = \\
&\left\langle \frac{1}{N}\left[\int_{\mathbb{R}^6} P_2(\theta_i,\sigma_i,R_i,\theta_j,\sigma_j,R_j,\tau)w(R_i-R_j)(\delta_0(\theta-\theta_i{}^*,R-R_i^*)+\delta_0(\rho-\rho_j^*,R-R_j^*))\cdot\right.\right. \\
&\left.\left.\cdot\, d\theta_i d\sigma_i dR_i d\theta_j d\sigma_j dR_j - 2P_1(\theta,\sigma,R,\tau)\right]\right\rangle.
\end{aligned}$$

Here, $\langle\cdot\rangle$ denotes the mean operator with respect to the random variables S_{ij} and the function $w(\cdot)$ corresponds to the interaction rate function which depends on the difference of the ratings. This yields

a hierarchy of equations, the so-called BBGKY-hierarchy, see [50, 51], describing the dynamics of the system of a large number of interacting agents.

A standard approximation is to neglect correlations and assume that

$$P_2(\theta_i, \sigma_i, R_i, \theta_j, \sigma_j, R_j, \tau) = P_1(\theta_i, \sigma_i, R_i, \tau) P_1(\theta_j, \sigma_j, R_j, \tau),$$

By scaling time as $t = 2\tau/N$ and performing the thermodynamical limit $N \to \infty$, we can use standard methods of kinetic theory [50,51] to show that the time-evolution of the one-agent distribution function f_γ (corresponding to P_1 and $f_\gamma f_\gamma$ to P_2) is governed by the following Boltzmann-type equation:

$$\begin{aligned} &\frac{d}{dt}\int_\Omega \varphi(\theta,\sigma,r) f_\gamma(\theta,\sigma,r,t) d\theta d\sigma dr = \\ &\frac{1}{2}\Bigg\langle \int_\Omega\int_\Omega \Big(\varphi(\theta,\sigma,r^*) + \varphi(\theta',\sigma',r'^*) - \varphi(\theta,\sigma,r) - \varphi(\theta',\sigma',r')\Big)\cdot \\ &\cdot w(r-r') f_\gamma(\theta,\sigma,r,t) f_\gamma(\theta',\sigma',r',t) d\theta' d\sigma' dr' d\theta d\sigma dr \Bigg\rangle, \end{aligned} \tag{3.11}$$

where $\varphi(\cdot)$ is a (smooth) test function, with support $\mathrm{supp}(\varphi) \subseteq \Omega$.

3.6.2 Analysis of the Boltzmann-type equation

Conservation of mass

Setting $\varphi(\theta, \sigma, r) = 1$ in equation (3.11) we have

$$\frac{d}{dt}\int_{\mathbb{R}^3} f_\gamma(\theta,\sigma,r,t) d\theta d\sigma dr = 0.$$

Therefore, the total mass is conserved, that is

$$\int_{\mathbb{R}^3} f_\gamma(\theta,\sigma,r,t) d\theta d\sigma dr = 1, \quad \text{for all times } t \geq 0.$$

Moments with respect to the rating

We define the s-th moment for $s \in \mathbb{N}$ with respect to r

$$m_{s,r}(t) = \int_{\mathbb{R}^3} r^s f_\gamma(\theta,\sigma,r,t) d\theta d\sigma dr. \tag{3.12}$$

Now choose $\varphi(\theta, \sigma, r) = r$. Due to (B), $(A1)$ and the symmetry of $b(\cdot)$ and $b''(\cdot)$ we obtain

$$\begin{aligned} \frac{d}{dt} m_{1,r}(t) =& \frac{1}{2}\gamma \int_{\mathbb{R}^6} f_\gamma(\theta,\sigma,r,t) f_\gamma(\theta',\sigma',r',t) w(r-r') \cdot \\ &\cdot \Big(b(\theta-\theta') - \frac{1}{2} b''(\theta-\theta')(\sigma^2 + \sigma'^2) - b(r-r') + \\ &+ b(\theta'-\theta) + \frac{1}{2} b''(\theta'-\theta)(\sigma^2+\sigma'^2) - b(r'-r)\Big) d\theta' d\sigma' dr' d\theta d\sigma dr = 0. \end{aligned} \tag{3.13}$$

Hence the mean value w.r.t. the rating is preserved in time and therefore $m_{1,r} = 0$ for all times $t \geq 0$.

Moments with respect to the variance and expected value

We define $m_{s,\theta}$ and m_{s,σ^2} similar to (3.12) and also need the boundedness of the second moment m_{2,σ^2}.

$$\frac{d}{dt}m_{2,\sigma^2}(t) = 0 \tag{3.14}$$

which follows directly from (3.11) when testing with $\varphi(\theta,\sigma,r) = \sigma^2$. Analogue we get

$$\frac{d}{dt}m_{1,\theta}(t) = \frac{d}{dt}m_{2,\theta}(t) = 0. \tag{3.15}$$

3.6.3 Derivation of the Fokker-Planck equation

We now derive the limiting Fokker-Planck equation in the case $\gamma \to 0$. Based on the interaction rules (3.1), which define the outcome of a game, we compute the expected values of the following quantities:

$$\begin{aligned}
&\langle r^* - r\rangle = \gamma(\langle S\rangle - b(r-r'))\\
&\mathrm{Var}[r^* - r] = \gamma^2\mathrm{Var}[S_{ij}]\\
&\langle (r^*-r)^2\rangle = \gamma^2(\langle S\rangle - b(r-r'))^2 + \mathrm{Var}[r^*-r] = \gamma^2(\langle S\rangle - b(r-r'))^2 + \mathrm{Var}[S])
\end{aligned}$$

with S analogue to (3.5) where we used $\langle X^2\rangle = \langle X\rangle^2 + \mathrm{Cov}[X,X] = \langle X\rangle^2 + \mathrm{Var}[X]$. Using Taylor expansion of $\varphi(\theta,\sigma,r^*)$ up to order two around (θ,σ,r), we obtain

$$\begin{aligned}
\langle \varphi(\theta,\sigma,r^*) - \varphi(\theta,\sigma,r)\rangle =& \langle r^*-r\rangle\frac{\partial}{\partial r}\varphi(\theta,\sigma,r) + \frac{1}{2}\langle (r^*-r)^2\rangle\frac{\partial}{\partial r^2}\varphi(\theta,\sigma,r) +\\
&+ \langle \mathcal{R}_\gamma(\varphi,\theta,\sigma,r,\tau)\rangle,
\end{aligned}$$

where the remainder term $\mathcal{R}_\gamma$ is given in the Peano-representation of Taylor's formula via

$$\begin{aligned}
\langle \mathcal{R}_\gamma(\varphi,\theta,\sigma,r,\tau)\rangle &= \frac{1}{2}\langle (r^*-r)^2\rangle\frac{\partial}{\partial r^2}(\varphi(\theta,\sigma,\bar r) - \varphi(\theta,\sigma,r))\\
&= \frac{1}{2}\gamma^2(\langle S\rangle - b(r-r'))^2 + \mathrm{Var}[S])\frac{\partial}{\partial r^2}(\varphi(\theta,\sigma,\bar r) - \varphi(\theta,\sigma,r))
\end{aligned}$$

for some $0 \le c \le 1$ with $\bar r$ defined as

$$\bar r = cr + (1-c)r^*.$$

Next we rescale time as $\tau = \gamma t$ and insert the expansion in (3.11). This yields

$$\begin{aligned}
&\frac{d}{d\tau}\int_{\mathbb{R}^3}\varphi(\theta,\sigma,r)f_\gamma(\theta,\sigma,r,\tau)d\theta d\sigma dr = \frac{1}{2\gamma}\int_{\mathbb{R}^3}\tilde{\mathcal{R}}_\gamma(\varphi,\theta,\sigma,r,\tau)f_\gamma(\theta,\sigma,r,\tau)d\theta d\sigma dr +\\
&+\int_{\mathbb{R}^6}\Big(\frac{\partial}{\partial r}\varphi(\theta,\sigma,r)(b(\theta-\theta') + K(\theta-\theta',\sigma,\sigma') - b(r-r'))\cdot\\
&\qquad\cdot w(r-r')f_\gamma(\theta,\sigma,r,\tau)f_\gamma(\theta',\sigma',r',\tau)\Big)d\theta' d\sigma' dr' d\theta d\sigma r
\end{aligned}$$

whereas the remainder $\tilde{\mathcal{R}}_\gamma$ is given by

$$\begin{aligned}
\tilde{\mathcal{R}}_\gamma(\varphi,\theta,\sigma,r,\tau) =& \int_{\mathbb{R}^3}\langle \mathcal{R}_\gamma(\varphi,r'^*,\theta',\sigma',r',\tau)\rangle w(r'-r)f_\gamma(\theta',\sigma',r',\tau)d\theta' d\sigma' dr'\\
&+\gamma^2\int_{\mathbb{R}^3}\frac{\partial^2}{\partial r'^2}\varphi(\theta',\sigma',r')\Big((\langle S\rangle - b(r'-r))^2 + \mathrm{Var}[S]\Big)\cdot\\
&\qquad\cdot w(r-r')f_\gamma(\theta',\sigma',r',\tau)d\theta' d\sigma' dr'.
\end{aligned}$$

All summands will vanish for $\gamma \to 0$ with similar arguments as in [71]. Let us assume that $\varphi(\theta, \sigma, r)$ belongs to the space $\mathcal{C}_{2+\delta}(\mathbb{R}^3) = \{h : \mathbb{R}^3 \to \mathbb{R},\ \|D^\zeta h\|_\delta < +\infty\}$, where $0 < \delta \leq 1$, ζ is a multi-index with $|\zeta| \leq 2$ and the seminorm $\|\cdot\|_\delta$ is the usual Hölder seminorm

$$\|f\|_\delta = \sup_{x,y \in \mathbb{R}^3} \frac{|f(x) - f(y)|}{|x - y|^\delta}.$$

Equations (3.5),(3.6) together with conservation laws (3.14) and (3.15) guarantee the boundedness of both expectation $\langle S \rangle$ and variance $\mathrm{Var}[S]$. Then with this choice of $\varphi(\theta, \sigma, r)$, both summands containing $\frac{\partial}{\partial r^2}\varphi$ vanish using the same arguments as in [56, 215].
Therefore, the density $f_\gamma(\theta, \sigma, r, \tau)$ converges to $f(\theta, \sigma, r, \tau)$ which solves

$$\begin{aligned} \frac{d}{d\tau}\int_{\mathbb{R}^3} \varphi(\theta,\sigma,r) f(\theta,\sigma,r,\tau) d\theta d\sigma dr &= \int_{\mathbb{R}^3} f(\theta,\sigma,r,\tau) \frac{\partial}{\partial r}\varphi(\theta,\sigma,r) \cdot \\ &\cdot \Bigg[\int_{\mathbb{R}^3} w(r-r')(b(\theta-\theta') + K(\theta-\theta',\sigma,\sigma') - b(r-r')) f(\theta',\sigma',r',\tau) \\ &\qquad d\theta' d\sigma' dr' \Bigg] d\theta d\sigma dr \end{aligned} \tag{3.16}$$

It remains to show that for suitable boundary conditions equation (3.16) gives the desired weak formulation of the Fokker-Planck equation. We calculate

$$\begin{aligned} \int_{\mathbb{R}} \Bigg(& f(\theta,\sigma,r,\tau)\varphi(\theta,\sigma,r)\Big(\int_{\mathbb{R}^3} w(r-r') \cdot \\ & \cdot (b(\theta-\theta') + K(\theta-\theta',\sigma,\sigma') - b(r-r')) f(\theta',\sigma',r',\tau) d\theta' d\sigma' dr' \Big) \Bigg|_{r=-\infty}^{r=+\infty} dr d\sigma \end{aligned}$$

This term is zero, if

$$\lim_{|r| \to +\infty} f(\theta, \sigma, r, \tau) = 0$$

These boundary condition are guaranteed for the Boltzmann equation $f_\gamma(\theta, \sigma, r, \tau)$ by mass conservation and preservation of the first moment $m_{1,r}$, see (3.13). Then (3.16) is the weak form of the Fokker-Planck equation

$$\begin{aligned} & \frac{d}{d\tau}\int_{\mathbb{R}^3} \varphi(\theta,\sigma,r) f(\theta,\sigma,r,\tau) d\theta d\sigma dr = \\ & -\int_{\mathbb{R}^3} \varphi(\theta,\sigma,r) \frac{\partial}{\partial r} \Bigg[f(\theta,\sigma,r,\tau) \int_{\mathbb{R}^3} w(r-r') \cdot \\ & \qquad \cdot (b(\theta-\theta') + K(\theta-\theta',\sigma,\sigma') - b(r-r')) f(\theta',\sigma',r') d\theta' d\sigma' dr' \Bigg] d\theta d\sigma dr. \end{aligned}$$

4 Repulsive Particles, a new diffusive term

This chapter contains results of an ongoing collaboration with Laura Kanzler and Christian Schmeiser which is close to submission.

That's it. Evasion is key.

Stefan Zweig in The Royal Game

Contents

Abstract

Repulsion within a finite radius is encountered in countless applications and is therefore highly relevant. Examples for applications include cell exclusion, i.e. an overlap of particles to be avoided, or microscopic pedestrian models. At the microscopic level, we define these particle dynamics in 1D. We perform a rigorous limit from the microscopic to the macroscopic scale. At both scaling levels numerical simulations are presented to underline the analytical results. We discuss the possible applications of this new diffusion term.

4.1 Introduction

In this paper, we aim to develop and analyze mathematical models on the microscopic and macroscopic scale encoding repulsive effects between particles. We start at the individual based setting with an ensemble of agents, each determined by its position x_i, which are undergoing repulsive interactions only occurring within a certain radius R. We work at the microscopic level in 1D with Lagrangian coordinates. Therefore, our agents have ordered labels given by the index i and only neighbouring individuals can interact via this repulsion. A sketch of these dynamics can be found in Figure 4.1.

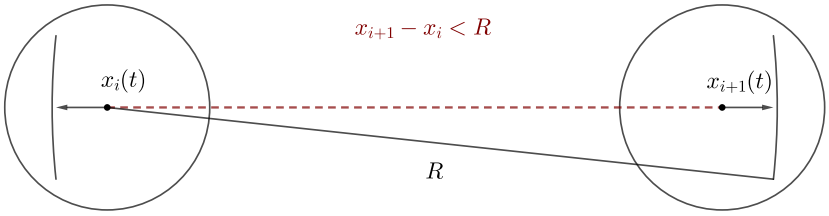

Figure 4.1: The two agents are within the interaction radius R, they are pushed away from each other.

Repulsive effects with a finite radius are often used in microscopic particle systems and their corresponding kinetic and macroscopic models. In flocking models, most important the Cucker-Smale- and the Vicsek-model, see [60,224], they appear as part of an interaction between attraction and repulsion. Example occur in the modelling of sheep, fish and birds, [48,49,186]. In our setting, only neighbouring particles interact, therefore we have a mixture between a metric interaction radius and a topological one as used in [101] or [23] in a kinetic context. A deterministic, Lagrangian many-particle system was also investigated in [64].

This repulsion can also be used to model size exclusion effects. On the microscopic level, this has been studied for the pattern formation in bacteria in [66, 73, 236]. In general, this new term of size exclusion is a macroscopic alternative to models based on e.g. cellular automata, compare [200], or microscopic asymmetric exclusion process, see [42], in which size exclusion has no influence on the diffusive term, typically a linear diffusive-term is derived.

This diffusive term can be microscopically interpreted as particles trying to reach a desired density. The desired density is similar to the desired velocity an important topic in pedestrian dynamics, see [6, 94], gaining new focus in the context of social distancing [160], and cannot be calibrated in other macroscopic models, see [94].

On a macroscopic level this diffusion on a compact support leads to a so called moving boundary problem. It is closely related to the so-called Stefan-problem, see [11, 46] or the classical books [161,193]. Analytically exact solutions are an ongoing topic, see [52,81] and also numerically challenges occur e.g. also in cancer research, see [120,211]. On a agent-based level, cancer growth was investigated in [169].

Rigorous limits from microscopic to macroscopic scales can serve to extend the theory of existence of solutions at the PDE level, see [64]. For e.g. the continuos version of the Vicsek-model a rigorous limit to a PDE was performed in [26], transferring regularity results to the macroscopic level. A bounded total variation is a common tool in numerical analysis to show convergence of a discretisation against the solution of a model, see [17, 114, 182, 220].

The modelled repulsion can also be seen as a cut-off potential. On a microscopic level this is often used for better computational speed and e.g. steadier movement of pedestrians as in the optimal-step-

model, see [201].

Our main contributions are as follows:

- We develop a microscopic model in order to describe repulsion with a finite radius R.
- We formally derive corresponding macroscopic models.
- We present analytical investigations on both levels and compare dynamics across scales.
- We present existence results for the macroscopic model both with classical theory on regularised initial data and via the rigorous limit from a special case on the microscopic level.
- We underlie our results with computational experiments.

This work is built up as follows. In the second section we introduce the microscopic system for the positions x_i and derive the corresponding system for ω_i which can be interpreted as the discrete derivate in Lagrangian coordinates s. The corresponding system can be seen as a discretization of the heat-equation with a cut-off-effect. Based on this we introduce the discrete density $\rho = 1/\omega$ and analyse the different systems and underlie our findings with numerical simulations. In the third section we formally introduce the corresponding macroscopic PDEs both in Eulerian and Lagrangian coordinates. We derive jump-conditions for the moving boundary present and present a global existence- and uniqueness-theory for regularised initial data based on the theory for the mentioned Stefan-problem. We show via a bounded total variation the rigorous limit in the general case. We present a stable discretization of our problem and show simulations also having the correct shock-speed. We make the formal limit in a special case rigorous. In the last section, we first address possible applications of this newly derived diffusion. Subsequently, we address open problems and give ideas for solutions. Finally, we summarize our findings.

4.2 The microscopic model, individual based dynamics in 1D

We aim to model an ensemble of particles distributed on the real line, where each individual interacts with each closest two neighbors following a **repulsive potential** as sketched in Figure 4.1. More precisely, we assume a number of $N+1$ particles with position $x_i(t) \in \mathbb{R}, i \in \{0, \dots, N\}$, where the numbering was chosen such that $x_{i+1}(t) > x_i(t)$ for all $i \in \{0, \dots, N-1\}$. The particle i interacts with its direct neighbors $i-1$ and $i+1$, which additionally have to be within the interaction radius R. Therefore particle i and $i+2$ do not interact even when $x_{i+2}(t) - x_i(t) < R$ holds. The repulsion function then is assumed to be directly proportional to the difference of the distance between the two particles and the interaction radius. This leads to the following ODE-system

$$\begin{aligned} \dot{x}_i &= \frac{1}{\tau}\left[-\left(R-(x_{i+1}-x_i)\right)_+ + \left(R-(x_i-x_{i-1})\right)_+\right], \qquad i \in \{1,\dots,N-1\}, \\ \dot{x}_0 &= -\frac{1}{\tau}\left(R-(x_1-x_0)\right)_+, \\ \dot{x}_N &= \frac{1}{\tau}\left(R-(x_N-x_{N-1})\right)_+, \end{aligned} \tag{4.1}$$

where $(z)_+$ stands for $\max(0,z)$. Here τ describes a characteristic time of system (4.1). We further introduce an equidistant reference grid on the real line with grid points $s_i := i\Delta s$, such that $x_i = x(s_i)$. With $x_0 = x(s_0)$ we encode the leftest particle, similar x_N is the rightist agent and we denote via L a characteristic macroscopic length of system (4.1), $L := x_N(0) - x_0(0)$. In the following we assume

that the interaction radius R is small in comparison to the intrinsic space scale L. After performing the macroscopic scaling

$$x \to Lx, \quad t \to \frac{\tau}{\Delta s^2} t,$$

we obtain the following individual based model for repulsive particles on the real line

$$\begin{aligned}
\dot{x}_i &= \frac{1}{\Delta s}\left[-\left(1-\frac{x_{i+1}-x_i}{\Delta s}\right)_+ + \left(1-\frac{x_i-x_{i-1}}{\Delta s}\right)_+\right], \qquad i \in \{1,\dots,N-1\},\\
\dot{x}_0 &= -\frac{1}{\Delta s}\left(1-\frac{x_1-x_0}{\Delta s}\right)_+,\\
\dot{x}_N &= \frac{1}{\Delta s}\left(1-\frac{x_N-x_{N-1}}{\Delta s}\right)_+.
\end{aligned} \tag{4.2}$$

We assume throughout the paper that $\Delta s N = const.$ and set this constant C.

4.2.1 Different notations and perspectives

With notation ω we now introduce the **scaled distance** between two neighbored points. It is given via

$$\omega_{i+\frac{1}{2}} := \frac{x_{i+1}-x_i}{\Delta s}, \quad i \in \{0,\dots,N-1\}. \tag{4.3}$$

We notice that the assumption of strict ordered positions of particles implies $\omega_{i+\frac{1}{2}} > 0$ and if x_i and x_{i+1} lie within the interaction radius, i.e. $x_{i+1} - x_i < \Delta s$ after rescaling, we have $\omega_{i+\frac{1}{2}} \leq 1$. Equation (4.3) leads to the definition of the so called **discrete density** ρ, which is known e.g. from the Follow-the-Leader model, see [91]:

$$\rho_{i+\frac{1}{2}} := \frac{1}{\omega_{i+\frac{1}{2}}}, \quad i \in \{0,\dots,N-1\}. \tag{4.4}$$

Now let us consider the ODE systems associated with (4.3) and (4.4). For the dynamics of ω we obtain from (4.2) the following system of N equations

$$\begin{aligned}
\dot{\omega}_{i+\frac{1}{2}} &= \frac{1}{\Delta s^2}\left[2\left(1-\omega_{i+\frac{1}{2}}\right)_+ - \left(1-\omega_{i-\frac{1}{2}}\right)_+ - \left(1-\omega_{i+\frac{3}{2}}\right)_+\right], i \in \{1,\dots,N-2\},\\
\dot{\omega}_{\frac{1}{2}} &= \frac{1}{\Delta s^2}\left[2\left(1-\omega_{\frac{1}{2}}\right)_+ - \left(1-\omega_{\frac{3}{2}}\right)_+\right],\\
\dot{\omega}_{N-\frac{1}{2}} &= \frac{1}{\Delta s^2}\left[2\left(1-\omega_{N-\frac{1}{2}}\right)_+ - \left(1-\omega_{N-\frac{3}{2}}\right)_+\right].
\end{aligned} \tag{4.5}$$

From (4.5) we can further deduce an ODE system for the masses $\rho_{i+\frac{1}{2}}$ since we have

$$\dot{\rho}_{i+\frac{1}{2}} = -\rho_{i+\frac{1}{2}}^2 \dot{\omega}_{i+\frac{1}{2}},$$

by differentiation of (4.4) with respect to t.

$$\begin{aligned}
\dot{\rho}_{i+\frac{1}{2}} &= -\frac{1}{\Delta s^2}\rho_{i+\frac{1}{2}}^2\left[2\left(1-\frac{1}{\rho_{i+\frac{1}{2}}}\right)_+ - \left(1-\frac{1}{\rho_{i-\frac{1}{2}}}\right)_+ - \left(1-\frac{1}{\rho_{i+\frac{3}{2}}}\right)_+\right], i\in\{1,\dots,N-2\},\\
\dot{\rho}_{\frac{1}{2}} &= -\frac{1}{\Delta s^2}\rho_{\frac{1}{2}}^2\left[2\left(1-\frac{1}{\rho_{\frac{1}{2}}}\right)_+ - \left(1-\frac{1}{\rho_{\frac{3}{2}}}\right)_+\right],\\
\dot{\rho}_{N-\frac{1}{2}} &= -\frac{1}{\Delta s^2}\rho_{N-\frac{1}{2}}^2\left[2\left(1-\frac{1}{\rho_{N-\frac{1}{2}}}\right)_+ - \left(1-\frac{1}{\rho_{N-\frac{3}{2}}}\right)_+\right].
\end{aligned} \tag{4.6}$$

In Figure 4.2 we have the same initial datum visualized in terms of $i\Delta s$ for the three different choices of variables.

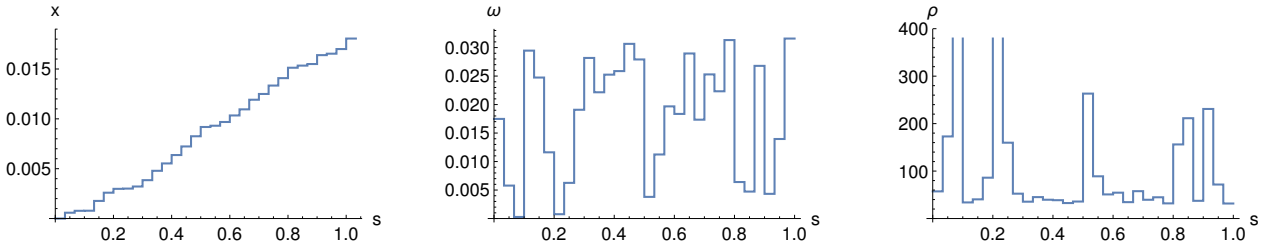

Figure 4.2: Random initial data in Lagrange coordinates for x, ω and ρ.

4.2.2 Analysis of the microscopic model

Existence results and upper resp. lower bounds

We start with classical existence results that can be formulated for our ODE system.

Theorem 4.1 (Existence and Uniqueness)**.** *For every $N\in\mathbb{N}$, $\Delta s\in\mathbb{R}^+$, there exists a unique global solution to (4.2).*

Proof. The proof is based on the fact that the right-hand side of (4.2) is Lipschitz. Using Picard–Lindelöf theorem in $\mathbb{R}^{N+1}$, following e.g. [213], finishes the proof. □

In the following, we introduce a maximum principle for System (4.5).

Theorem 4.2 (Min-Max-principle)**.** *We define for system (4.5) via*

$$\omega_{\min} := \min_i\left(\omega_{i+\frac{1}{2}}(0)\right), \qquad \omega_{\max} := \max\left(\max_i\left(\omega_{i+\frac{1}{2}}(0)\right),1\right),$$

minimum and maximum of our initial data.

1. *The following **Min-Max-principle** holds*

$$\omega_{\min}\le\omega_{i+\frac{1}{2}}(t)\le\omega_{\max},\quad \forall i\in\{1,\dots,N-2\}.$$

2. *We have $\dot{x}_0\le 0$ and $\dot{x}_N\ge 0$. Depending on the initial datum $x(0)$ we have upper respective lower bounds on x_N respective x_0 given via*

$$C\omega_{\min}\le x_N(t)-x_0(t)\le C\omega_{\max}.$$

Proof. Assuming $\omega_{i+\frac{1}{2}}$ reaches $\omega_{\min}$, equation (4.5) reformulates to

$$\begin{aligned}\dot{\omega}_{i+\frac{1}{2}} &= \frac{1}{\Delta s^2}\left[2\left(1-\omega_{\min}\right)_+ - \left(1-\omega_{i-\frac{1}{2}}\right)_+ - \left(1-\omega_{i+\frac{3}{2}}\right)_+\right] \\ &\geq \frac{1}{\Delta s^2}\left[2\left(1-\omega_{\min}\right)_+ - \left(1-\omega_{\min}\right)_+ - \left(1-\omega_{\min}\right)_+\right] = 0,\end{aligned}$$

therefore $\omega_{i+\frac{1}{2}}$ increases or stays constant. The upper bound is shown analogously.

We have

$$x_N(t) - x_0(t) = \Delta s\left(\frac{x_N(t)-x_{N-1}(t)}{\Delta s} + \cdots + \frac{x_1(t)-x_0(t)}{\Delta s}\right)$$

and therefore

$$\Delta s N \omega_{\min} \leq x_N(t) - x_0(t) \leq \Delta s N \omega_{\max}.$$

Using Theorem 4.4.1 finishes the second statement. □

The previous Theorem provides positivity of ω for suiting ω_0 and therefore well-posedness of system (4.6) for all times t. Based on the previous Theorem 4.2, we can even formulate a stronger statement for minimum and maximum of system (4.5). We therefore define for every t

$$\omega_{\min}(t) := \min_i\left(\omega_{i+\frac{1}{2}}(t)\right), \qquad \omega_{\max}(t) := \max_i\left(\omega_{i+\frac{1}{2}}(t)\right),$$

and then conclude with the following lemma.

Lemma 4.3 (A stronger Min-Max-principle)**.** *The graph $\omega_{\min}(t)$ is monotone increasing in t, similarly $\omega_{\max}(t)$ is monotone decreasing.*

Proof. Clearly we have $\omega_{\min}(t) \geq \omega_{\min}$, $\omega_{\max}(t) \leq \omega_{\max}$ through Theorem 4.2. Let i be the index of $omega_min$ at time t. The proof then follows from

$$\begin{aligned}\dot{\omega}_{i+\frac{1}{2}} &= \frac{1}{\Delta s^2}\left[2\left(1-\omega_{\min}(t)\right)_+ - \left(1-\omega_{i-\frac{1}{2}}\right)_+ - \left(1-\omega_{i+\frac{3}{2}}\right)_+\right] \\ &\geq \frac{1}{\Delta s^2}\left[2\left(1-\omega_{\min}(t)\right)_+ - \left(1-\omega_{\min}\right)_+ - \left(1-\omega_{\min}\right)_+\right] \geq 0.\end{aligned}$$

The statement for the maximum is shown analogously. □

Characteristic moments of the model

We continue with bounds of the microscopic model and therefore look at a 'discrete weak formulation' in x of problem (4.2). For a test-function φ with notation $\varphi_i := \varphi(s_i)$ the weak formulation of the dynamics is given by

$$\begin{aligned}\sum_{i=0}^{N}\dot{x}_i\varphi_i &= \frac{1}{\Delta s}\sum_{i=1}^{N-1}\left[\left(1-\frac{x_i-x_{i-1}}{\Delta s}\right)_+ - \left(1-\frac{x_{i+1}-x_i}{\Delta s}\right)_+\right]\varphi_i \\ &\quad - \frac{1}{\Delta s}\left(1-\frac{x_1-x_0}{\Delta s}\right)_+\varphi_0 + \frac{1}{\Delta s}\left(1-\frac{x_N-x_{N-1}}{\Delta s}\right)_+\varphi_N \\ &= \sum_{i=0}^{N-1}\left(1-\frac{x_{i+1}-x_i}{\Delta s}\right)_+\frac{(\varphi_{i+1}-\varphi_i)}{\Delta s}.\end{aligned} \tag{4.7}$$

Similar we derive a 'weak formulation' in ω

$$\sum_{i=0}^{N-1} \dot{\omega}_{i+\frac{1}{2}} \varphi_i = \frac{1}{\Delta s^2} \Bigg[\sum_{i=1}^{N-2} \left(1 - \omega_{i+\frac{1}{2}}\right)_+ (2\varphi_i - \varphi_{i-1} - \varphi_{i+1}) + \left(1 - \omega_{\frac{1}{2}}\right)_+ (2\varphi_0 - \varphi_1) + \left(1 - \omega_{N-\frac{1}{2}}\right)_+ (2\varphi_{N-1} - \varphi_{N-2}) \Bigg]. \tag{4.8}$$

Using the weak formulations one can show characteristic properties for our systems in ω and x.

Theorem 4.4 (Characteristic moments)**.** *For (4.2) and (4.5) we have the following properties*

1. *The total momentum $\sum_{i=0}^{N} \dot{x}_i$ is equal to 0, hence the **center of mass**, is conserved, i.e.*

$$\bar{x} := \frac{1}{N+1} \sum_{i=0}^{N} x_i = const.$$

2. *The **variance** in x*

$$\mathcal{V}_x(t) := \frac{1}{N} \sum_{i=0}^{N} (x_i - \bar{x})^2$$

increases with respect to time.

Proof. For the first part, just set $\varphi_i \equiv 1$ in (4.7) for all i. For the second part, we set $\varphi_i \equiv \left(x_i - \frac{\bar{x}}{N}\right)$ in (4.7) and one obtains

$$\dot{\mathcal{V}}_x(t) = \frac{1}{\Delta s} \sum_{i=0}^{N-1} \left(1 - \frac{x_{i+1} - x_i}{\Delta s}\right)_+ (x_{i+1} - x_i) \geq 0,$$

where the last inequality is trivial. □

4.2.3 Numerical simulations

In the following we underline the previous statements with numerical experiments in x and ω. The systems (4.2) and (4.5) have been solved with an implicit Euler algorithm to conserve the characteristic properties. We discretized as follows,

$$x_i^{n+1} = x_i^n + \frac{\Delta t}{\Delta s} \left[- \left(1 - \frac{x_{i+1}^{n+1} - x_i^{n+1}}{\Delta s}\right)_+ + \left(1 - \frac{x_i^{n+1} - x_{i-1}^{n+1}}{\Delta s}\right)_+ \right], \quad i \in \{1, \dots, N-1\},$$

based on classical ideas as in e.g. [44]. We have discretized the boundary values x_0, x_N analogously and did similar for (4.5).

We simulate $N = 20$ agents and chose a time-stepping of $\Delta t = 0.1 \Delta s^2$ with $\Delta s = 0.1$ using a typical parabolic CFL-conditions. We solved the non-linearity in $(.)_+$ with a fixed-point approach over $n = 40$ iterations as proposed in [133]. The results can be found in Figure 4.3.

The Min-Max-principle of Theorem 4.2 shows the relation with an elliptic system which has in general a smoothening effect. We see that in Figure 4.3b. However, this effect does not occur if the points x_i are too far apart. We have visualized this in Figure 4.3c, groups remain that do not interact with each other. This fact will later motivate us to consider subproblems individually. Figure 4.3d visualizes the Min-Max-principle of Theorem 4.2.1 whereas also the time-dependent version stated Lemma 4.3 can be seen.

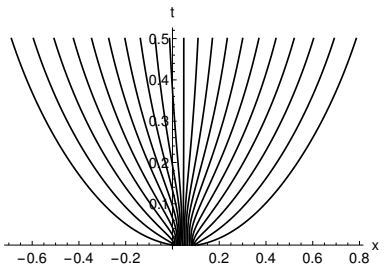

(a) The trajectories x_i over time, we see the agents moving away from each other. The initial values are chosen so that $x_i - x_{i+1} < \Delta s$ for all i, so all agents are in interaction.

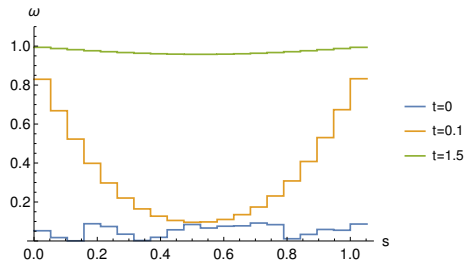

(b) The simulation associated with Figure 4.3a in ω, we see a smoothing effect with long term behavior $\omega_{i+\frac{1}{2}} \to 1$.

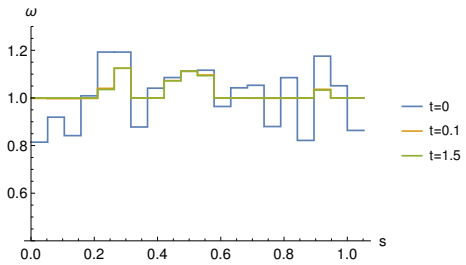

(c) Since too many $\omega_{i+\frac{1}{2}}(0)$ are greater than 1, the smoothing effect in the system does not occur. This can be seen as some plateaus do not interact with each other.

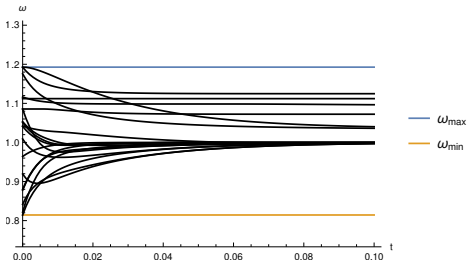

(d) The Min-Max-principle in Theorem 4.3 visualized.

Figure 4.3: The evolution of the systems in ω and x for different initial values.

4.3 The macroscopic level

We start our investigation at the macroscopic level by formally deriving the partial differential equations and their boundary conditions in the upcoming Subsection 4.3.1. Subsequently we derive jump-conditions comparable to those in classical works, see [77], from the fact that the resulting equations for ω in s as well as ρ in x are conservation laws. This can be seen as Rankine Hugenoit jump conditions and are also called the Stefan condition in the related Stefan problem [46]. Starting from the established theory of jump conditions, we formally consider the case of colliding jumps. From this, we see that our problem can always be reduced to several single minimal, so called one-sided problems, see Figure 4.4b. For this minimal problem, we perform the analysis in Subsection 4.3.2 applying the theory from [11, 46] to show existence and uniqueness, but only for regularized initial conditions. It is based on the established theory of Stefan-problems with Dirichlet boundary conditions, see [131]. The rigorous limit from our microscopic ODE-system to a macroscopic PDE can be found in Subsection 4.3.3. Via this limit we obtain existence of a weak solution in the general case, but lose uniqueness. We present in Subsection 4.3.4 numerical simulations which underline the expected behaviour.

4.3.1 Preliminary considerations

In the following, we derive the macroscopic PDEs corresponding to (4.2) and (4.5). We consider a simple case to get an understanding of the general problem. We derive the coordinate transformation from s to x. From this, we also study the jump conditions of the problem at the non-differentiable position $x_\star$ (and $s_\star$) in $(.)_+$, whose velocity we also formally study. Subsequently, we motivate a

global theory which is due to the minimal problem introduced earlier, which we analyze rigorously in Subsection 4.3.2.

Formally derived PDE in s

We now derive formally the corresponding PDEs in x and ω in Lagrangian coordinates. Important for the calculations is the fact that $(a+\mathcal{O}(\Delta s))_+ = (a)_+ + \mathcal{O}(\Delta s)$. Seeing $\frac{x_i - x_{i-1}}{\Delta s}$ in (4.2) as a central difference and replace it via $\partial_s x_{i+\frac{1}{2}} + \mathcal{O}(\Delta s)$ (same in $i - \frac{1}{2}$) we derive formally the following PDEs in $s \in [0,1]$,

$$\begin{aligned} &\partial_t x(s,t) = -\partial_s \left(1 - \partial_s x(s,t)\right)_+, \\ &\left(1 - \partial_s x(0,t)\right)_+ = \left(1 - \partial_s x(1,t)\right)_+ = 0, \\ &x(s,0) = x_0(t). \end{aligned} \tag{4.9}$$

For the boundary points we simply multiply the equations for x_0 and x_N with Δs before passing to the limit.

By definition (4.3) we have $\partial_s x = \omega$ for $\Delta s \to 0$. Analogously to x we now derive for ω

$$\begin{aligned} &\partial_t \omega(s,t) = -\partial_s^2 \left(1 - \omega(s,t)\right)_+, \\ &\left(1 - \omega(0,t)\right)_+ = \left(1 - \omega(1,t)\right)_+ = 0, \\ &\omega(s,0) = \omega_0(s). \end{aligned} \tag{4.10}$$

The PDE itself was already the discretization of the Laplace-operator for $(1-.)_+$. For the boundary points we make the assumption $\omega_{i-\frac{1}{2}}, \omega_{N+\frac{1}{2}} \geq 1$, introducing artificial points x_{-1}, x_{N+1}. This allows us to also pass to the limit in the second and third equation of (4.2).

In the following we consider system (4.10) for the special case of initial data less than 1.

The trivial case in ω and s

Assuming $0 \leq \omega_0 \leq 1$ we can simplify (4.10) to the following PDE,

$$\begin{aligned} &\partial_t \omega(s,t) = -\partial_s^2 \left(1 - \omega(s,t)\right) = \partial_s^2 \omega(s,t), \\ &\omega(0,t) = \omega(1,t) = 1 \\ &\omega(s,0) = \omega_0(s), \text{ with } 0 \leq \omega_0(s) \leq 1. \end{aligned} \tag{4.11}$$

It is a classic result, see [77], that the solution of the heat-equation with non-homogenous Dirichlet-boundary conditions can be traced back to the heat-equation with homogenous Dirichlet-boundary conditions when substituting $\omega = u + 1$. Thus the solution to (4.11) is unique. It follows directly, that with $0 < \omega_0(s) < 1$ for $s \in (0,1)$ we have $0 < \omega(s,t) < 1$ in $(0,1) \times (0,T]$ due to the strong maximum principle. The solution to (4.11) is $C^\infty([0,1] \times (0,T])$ regardless of the regularity of $\omega_0(s)$ and can be, depending on the latter, given explicitly. This allows us to see the strong agreement between microscopic and macroscopic level, see Figure 4.4a, with $\omega_0(s) = 1 - \sin(\pi s)$ and $N = 30$ agents. The well-known long-time behaviour $\omega \to 1$ of (4.11) is clearly visible.

Euler and Lagrangian coordinates, from s to x

We obtain the transformation from Lagrangian coordinates (s,t) to Eulerian coordinates (x,τ) by integrating $\partial_s x = \omega$ where we denote $x(0,t) := x_0(t)$ and $x_1(t) := x(1,t)$. The latter actually

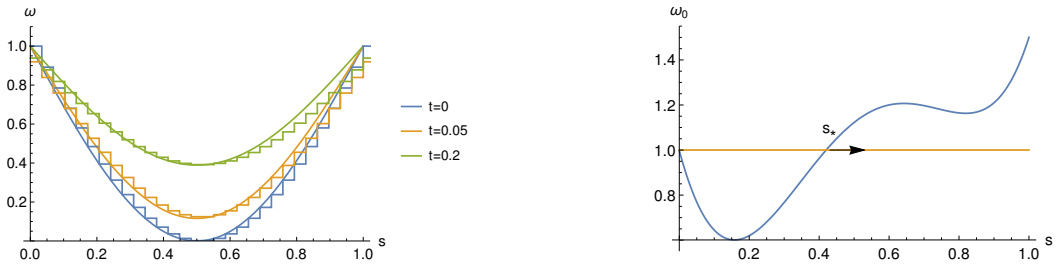

(a) Alignment of the microscopic and macro level, $N = 30$, $N\Delta s = 2$, $\Delta t = 10^{-3}\Delta s$.

(b) The so-called one-sided problem. The velocity of $s_\star$ is given by (4.15).

Figure 4.4: On the left we see alignment between the two scales for equation (4.11) in Lagrange-coordinates. On the right we see initial datum for the one-sided problem which will be the focus of our main investigation in Subsection 4.3.2.

corresponds to $x_N(t)$ in the microscopic model (4.1). We then have

$$x = x_0(t) + \int_0^s \omega(\sigma, t)d\sigma, \quad \tau = t. \tag{4.12}$$

This implies

$$\partial_s = \omega\partial_x, \quad \partial_\tau = \partial_t = \left(\dot{x}_0 + \int_0^s \partial_t\omega(\sigma, t)d\sigma\right)\partial_x.$$

For the expression in the parentheses we get, while using (4.9) and then (4.10),

$$\dot{x}_0 + \int_0^s \partial_t\omega(\sigma, t)d\sigma = \dot{x}_0 - \partial_s(1-\omega)_+|_{\sigma=0}^{s} = -\partial_s(1-\omega)_+.$$

Therefore, in terms of Eulerian variables, (4.10) becomes

$$\partial_\tau\omega - \omega\partial_x(1-\omega)_+\partial_x\omega = -\omega\partial_x(\omega\partial_x(1-\omega)_+),$$

this is equivalent to

$$\partial_\tau\omega = -\omega^2\partial_x^2(1-\omega)_+.$$

Using $\rho = \frac{1}{\omega}$ we obtain for the macroscopic density,

$$\partial_\tau\rho = \partial_x^2\left(1 - \frac{1}{\rho}\right)_+,$$

where we replace in the following τ via t. To be more precise, this can be seen as an equation on a moving domain, $x_0(t) < x < x_1(t)$ with Dirichlet boundary conditions:

$$\begin{aligned} &\partial_t\rho(x,t) = \partial_x^2\left(1 - \frac{1}{\rho(x,t)}\right)_+, \quad x \in \Omega(t) = [x_0(t), x_1(t)], \\ &\rho(x_0(t), t) = \rho(x_1(t), t) = 1, \\ &\rho(x, 0) = \rho_0(x), \end{aligned} \tag{4.13}$$

The dynamics of x_0 and x_1 are then special cases of the shock speed formulas of the following subsection.

Jump-conditions in s and x

In the following we use the fact that (4.10) is a local conservation law and therefore for any interval $[a,b] \subseteq [0,1]$ we have

$$\frac{d}{dt}\int_a^b \omega(s,t)ds = J_{|a} - J_{|b}$$

with the flux being defined as

$$J := \partial_s \left(1-\omega(s,t)\right)_+ . \tag{4.14}$$

For the derivation of our jump condition we reduce ourself in the following to a simple problem with a non-differentiability in $(.)_+$. We call this a one-sided problem and visualized ω_0 in Figure 4.4b. This means we start with initial data $\omega_0(s)$ of the form $0 < \omega_0(s) < 1$ for $s \in [0, s_\star(0))$, $\omega_0(s) > 1$ for $s \in [s_\star(0), 1]$ where $s_\star(t)$ denotes the position of non-differentiability in $(.)_+$ depending on t. Denoting by $s_\star-, s_\star+$ the left- and right-handed limit this results with $a < s_\star(t) < b$ in

$$\dot{s}_\star(t)\left(1-\omega(s_\star+,t)\right) + \int_a^{s_\star-} \partial_t \omega(s,t)ds = J|_a$$

where we used $\omega(s_\star-,t) = 1$ and $\omega(s_\star+,t) > 1$. Therefore $\partial_s \left(1-\omega(s_\star+,t)\right)_+ = 0$. We can deduce

$$\begin{aligned}
\dot{s}_\star(t)\left(1-\omega(s_\star+,t)\right) - \int_a^{s_\star-} \partial_s^2(1-\omega(s,t))ds &= J|_a, \\
\dot{s}_\star(t)\left(1-\omega(s_\star+,t)\right) - \partial_s(1-\omega(s,t))|_a^{s_\star-} &= J|_a.
\end{aligned}$$

Therefore the jump-condition in s is given via

$$\dot{s}_\star(t) = \frac{\partial_s\left(\omega(s_\star(t)-,t)\right)}{\omega(s_\star(t)+,t)-1}. \tag{4.15}$$

Analogous considerations can be made for Euclidean coordinates. For the jump $x_\star$ in x we use (4.13) with the flux $J = -\partial_x\left(1-\frac{1}{\rho(x,t)}\right)_+$. Using $\partial_s = \omega\partial_x$ and $\omega = \frac{1}{\rho}$ the following condition for the jump in x

$$\dot{x}_\star(t) = \frac{\partial_x(\frac{1}{\rho(x_\star(t)-,t)})}{1-\rho(x_\star+(t),t)} \tag{4.16}$$

can be derived.

A first investigation of the shock-speed

We start with initial data $\rho_0 = 1+cx$, $c>0$, and investigate the development of $x_\star(0) = 1$ for a small period of time t. The jump-condition (4.16) gives us for small t

$$\dot{x}_\star(t) \approx \frac{1}{2x_\star(t)},$$

therefore we have $x_\star \approx \sqrt{t}$. This infinite velocity for $t=0$ also occurs in the Stefan-problem, see e.g. example 1 in [11], Chapter 1. It can also be seen on a microscopic level in Figure 4.3a for x_0 and x_N.

Colliding jumps and dissecting a problem

Having derived our jump condition, we now analyse the case of colliding jumps, as in [77], Chapter 3.4.

In Figure 4.5b we see two colliding jumps $s_{*,1}$, $s_{*,2}$ at time $t_\star$, resulting from initial datum as seen in Figure 4.5a. Since $\omega(s_{\star,1}-,t) = \omega(s_{\star,2}+,t) = 1$, continuity of ω on $[0,1]$ at $t_\star$ is trivial. We then can reformulate our problem to problem (4.11) starting at $t_\star$ with continuous initial data $\omega(s,t_\star)$. Similar results can be formulated for (4.16).

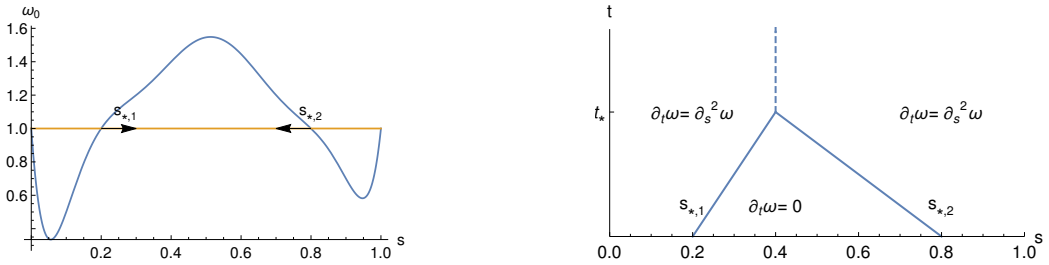

(a) Initial datum which leads to two colliding jumps $s_{*,1}$, $s_{*,2}$.

(b) Two colliding jumps and the resulting solution.

Figure 4.5: Initial-data satisfying the Dirichlet-boundary conditions and leading to colliding jumps. At $t_\star$ we can reformulate the problem with continuous initial data $\omega_{t_\star}(s)$.

After presenting a solution of the colliding jumps, we can split initial datum as in Figure 4.6 into several problems for ω in Lagrangian coordinates similar to Figure 4.4b. If these problems intersect at time $t_\star$, we reformulate the problem with a continuous initial datum $\omega_{t_\star}$. We answer the existence and uniqueness of those equivalent single problems in the following Subsection 4.3.2 for a regularized version.

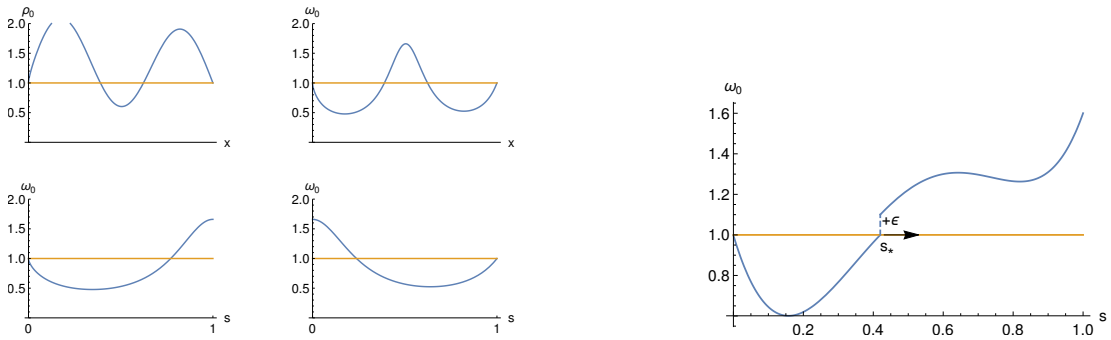

(a) Initial datum ρ_0 and corresponding ω_0 in Euler coordinates. We intersect the problem into two one-sided problems in Lagrangian coordinates. The problems will collide at a later time-point $t_\star$.

(b) Regularised initial datum ω_0 based on Figure 4.4b, as described in (4.21).

Figure 4.6: Initial-data in Euler-coordinates for ρ_0 and ω_0.

4.3.2 Uniqueness of the solution for regularised initial datum ω_0

The previous comments leads us to the conclusion that to solve our setting analytically we can reduce ourself to the previously mentioned one-sided problem in s for ω. This is strongly related to the already

mentioned Stefan-problem, see [46]. While the Stefan-problem is mostly solved with Neumann- or Robin-Boundary conditions, see [209, 210], the problem with Dirichlet-BCs is also a classic result, see [131].

We look at equation (4.10) with initial data as can be seen in Figure 4.4b, where the jump-condition is given via (4.15). However for mentioned initial datum $\omega_0(s)$ there are no dynamics occurring for $s > s_\star$, therefore the jump-condition changes to

$$\dot{s}_\star(t) = \frac{\partial_s \omega(s_\star(t)-, t)}{\omega_0(s_\star(t)+) - 1}. \tag{4.17}$$

Unlike in the classical Stefan-problem, the difficulty here lies in the singularity of (4.17) at time $t = 0$, where the denominator will vanish. The regularity of $s_\star$ therefore strongly depends on the initial data $\omega_0(s)$, which we will precise later. In general we cannot expect $s_\star$ being Lipschitz for $t = 0$ due to the just mentioned singularity, but we expect $\dot{s}_\star$ to be locally bounded for all times $t > 0$, if initial data are as in (4.19). Due to this difficulty in the jump-condition (4.17) necessary properties and methods for existence and uniqueness exceed the ones from already existing literature, as [11, 46].

We analyse the problem on the domain $(s, t) \in \Omega = [0, 1] \times [0, T)$. We assume $s_\star \in [0, 1]$ for all $t < T$. For $s > s_\star$ we have $\partial_t \omega = 0$. Therefore we want to mention that the problem becomes a trivial reformulation when $s_\star = 1$ for $t < T$ and thus investigate only the case $s_\star(t) < 1$ for $t \in [0, T)$. For abbreviation-reasons we introduce

$$\Omega_{1,T} = \{(s, t) | 0 < s < s_\star, 0 < t < T\}, \quad \Omega_{2,T} = \{(s, t) | s_\star < s < 1, 0 < t < T\}$$

and similar define Ω_1, Ω_2 in s for $t = 0$. Altogether we investigate the following problem

$$\begin{aligned}
\partial_t \omega(s, t) &= \partial_s^2 \omega(s, t) && \text{in } \Omega_{1,T} \\
\partial_t \omega(s, t) &= 0 && \text{in } \Omega_{2,T} \\
\omega(0, t) &= \omega(s_\star, t) = 1, \\
\dot{s}_\star(t) &= \frac{(\partial_s \omega(s_\star(t)-, t))}{\omega_0(s_\star(t)+) - 1} \\
s_\star(0) &= s_\star^0 \in (0, 1) \\
\omega(s, 0) &= \omega_0(s).
\end{aligned} \tag{4.18a}$$

We already see in (4.18a) that $s_\star$ will not be differentiable for $t = 0$ and will explore in the following how the regularity of ω_0 influences the regularity of the solution to problem (4.18). We hereby already summarize the necessary properties we have to assume of the initial condition ω_0:

$$\begin{aligned}
&\omega_0 \in C([0, 1]), \\
&\omega_0(0) = \omega(s_\star^0) = 1, \\
&0 < \omega_0(s) < 1 \quad \text{for } s \in (0, s_\star^0), \qquad \omega_0(s) > 1 \qquad \text{for } s \in (s_\star^0, 1], && \text{(4.19a)} \\
&\omega_0(s) \geq 1 - H(s_\star^0 - s), \text{ for } s \in [0, s_\star^0) && \text{(4.19b)}
\end{aligned}$$

where in (4.19b) we assume existence of a constant $H > 0$ acting as an lower bound on the first derivative of ω_0 at the singular point $s_\star^0$.

We now can start with defining a strong solution to problem (4.18). We call a pair $(\omega, s_\star)$ a **strong solution** to problem (4.18), if

$$\begin{aligned}
&s_\star \in C^1([0, T]), s_\star^0 \in (0, 1), s_\star(t) > 0, 0 \leq t \leq T \\
&\omega(s, t) \in C(\overline{\Omega_{1,T}}) \cap C^{2,1}(\Omega_{1,T})
\end{aligned} \tag{4.20}$$

We will assume to start with discontinuous initial data ω_0, which are jumping at $s_\star^0$. Namely, we replace ω_0 by $\omega_0 + \epsilon$ for $s > s_\star^0$, as can be seen in Figure 4.6b. This regularises the jump-condition (4.18a) and leads to the following adaptation of the assumption on the initial data,

$$\begin{aligned}
&\omega_0 \in C([0, s_\star^0]) \cap C((s_\star^0, 1]), \\
&\omega_0(0) = \omega(s_\star^0) = 1, && \text{(4.21a)} \\
&0 < \omega_0(s) < 1 \quad \text{for } s \in (0, s_\star^0), \qquad \omega_0(s) > 1 + \epsilon \quad \text{for } s \in (s_\star^0, 1], && \text{(4.21b)} \\
&\omega_0(s) \geq 1 - H(s_\star^0 - s), \text{ for } s \in [0, s_\star^0).
\end{aligned}$$

In the following we start with existence and uniqueness of problem (4.18)&(4.21). In multiple steps of our calculation it can be seen clearly that the limit $\epsilon \to 0$, therefore replacing (4.21) with (4.19), is nontrivial. Literature on the Stefan problem changes here into a weak formulation of problem (4.18), see [11]. We start with showing properties of our solution following the theory of strong solutions in just mentioned [11]:

Lemma 4.5. *A solution $(\omega, s_\star)$ as in (4.20) of (4.18) fulfils*

$$\begin{aligned}
&0 < \omega(s,t) < 1 \text{ in } \Omega_{1,T}, \\
&\dot{s}_\star > 0 \text{ for } t > 0.
\end{aligned}$$

Proof. We have $0 < \omega_0(s) < 1$ in $\Omega_{1,T}$ and $\omega_0(0) = \omega_0(s_\star) = 1$ because of (4.21a), (4.21b). The weak maximum principle, see [77], Theorem 9, Chapter 7.1.4, states that ω is attaining its maximum (and minimum) on the parabolic boundary of $\Omega_{1,T}$. We than can deduce $0 < \omega(s,t) \leq 1$. Assuming now $\omega(\bar{s}, \bar{t}) = 1$ for some $(\bar{s}, \bar{t})$ in the interior of $\Omega_{1,T}$, then the strong Maximum principle, see [77], Theorem 11, Chapter 7.1.4, leads to $\omega(s,t) = 1$ for $(0, s_\star) \times (0, \bar{t})$, a contradiction.

Hopf's Lemma for parabolic equations, see [84, 223], gives us $\partial_s \omega > 0$ on the parabolic boundary of $\Omega_{1,T}$. Since we also have $\omega_0(s_\star(t)+) - 1 > 0$ it follows

$$\dot{s}_\star(t) = \frac{(\partial_s \omega(s,t))\,|_{s_\star -}}{\omega_0(s_\star(t)+) - 1} > 0. \tag{4.22}$$

□

We continue with properties of a solution (4.20) in theorem 4.6 which results in a bootstrapping-argument for existence of our solution in theorem 4.7 following the structure of [11].

Theorem 4.6. *Let ω be a solution as in (4.20) and $s_\star \in \mathrm{Lip}([0,T])$ be non decreasing. Then we have the following properties for $(\omega, s_\star)$,*

(a) $1 - H(s_\star(t) - s) < \omega(s,t) \leq 1$, *in* $\Omega_{1,T}$,

(b) $0 < \partial_s \omega(s_\star(t), t) \leq H$, *for* $0 < t < T$,

(c) $\partial_s \omega$ *is continuous,*

(d) $s_\star \in C^1(0,T)$,

here H is the Lipschitz-constant in (4.19b).

Proof. For property (a) let us define $v(s,t) = 1 - H(s_\star(t) - s)$. It follows trivially for v

$$\begin{aligned}
&\partial_t v - \partial_s^2 v = -H\dot{s}_\star(t) \leq 0 \qquad \text{in } \Omega_{1,T}\\
&v(s_\star(t),t) = \omega(s_\star(t),t) = 1, \qquad 0 \leq t \leq T\\
&v(s,0) = 1 - H(s_\star^0 - s) \leq \omega_0(s), \qquad 0 \leq s \leq s_\star^0.
\end{aligned}$$

We therefore can deduce $v(s,t) \leq \omega(s,t)$ in $\Omega_{1,T}$. Property (b) then follows trivially.

The regularity of ω_s in the interior of $\Omega_{1,T}$ stated in (c) is trivial and follows from classical regularity results for elliptic PDEs. For the regularity at $(s_\star, t)$ we now proceed as follows. We perform a transformation of coordinates via

$$s = \frac{y}{s_\star(t)}, \quad v(y,t) = \omega(y s_\star(t), t),$$

which leads to

$$\partial_s^2\omega(s,t) = \frac{1}{s_\star^2(t)}\partial_y^2 v(y,t) \quad \text{and} \quad \partial_t\omega(s,t) = \partial_t v(y,t) + \frac{y\dot{s}_\star(t)}{s_\star(t)}\partial_y v(y,t).$$

This changes our problem moving boundary problem (4.20) into the following on $[0,1]$,

$$\begin{aligned}
\partial_t v(y,t) &= \frac{1}{s_\star^2(t)}\partial_y^2 v(y,t) - \frac{y\dot{s}_\star(t)}{s_\star(t)}\partial_y v(y,t) \quad \text{in } (0,1)\times(0,T)\\
v(0,t) &= v(1,t) = 1.
\end{aligned}$$

For $s_\star$ being Lipschitz. We now can use standard local regularity estimates for the solution of our parabolic equation, we sketch in Appendix 4.5.1 an adaption of Theorem 5 in [77], Chapter 7. Therefore we define $\frac{1}{s_\star^2(t)} =: a(t)$, $-\frac{y\dot{s}_\star(t)}{s_\star(t)} =: b(t,y)$ in (4.23) time-dependent but bounded w.r.t. time due to the regularisation (4.21). This adaption gives us $v \in L^2\left(0,T;H^2([0,1])\right) \cap L^\infty\left(0,T;H_0^1([0,1])\right)$. It follows that $\partial_s v \in H^1([0,1])$ for every t and thus it is continuous due Sobolev embedding [77]. Since we have

$$\partial_s\omega(s,t) = \frac{1}{s_\star(t)}\partial_y v(y,t)$$

our results follows.

We can continue with property (d). Remember $\omega_0(s) > 1$ for $s > s_\star^0$. Additionally we required $\omega_0 \in C(s_\star, 1]$. Therefore the jump-condition (4.22) gives us, using (c) and $s_\star$ being non-decreasing, $s_\star \in C^1(0,T]$, since the right-hand side of (4.22) is continuous. □

We can deduce for our problem the following existence- and uniqueness-result where we only sketch the proof of uniqueness following [46]. Existence of a solution to (4.18) uses a fixed point argument on a suiting convex and compact subset of a Banach space where again the regularization in (4.21) cannot be omitted.

Theorem 4.7 (Existence and Uniqueness)**.** *Assume* (4.21)*, then there exists a unique solution to* (4.18) *satisfying* (4.20)*.*

Proof. Using the properties of Theorem 4.6 together with the regularization of our initial datum we can use a similar bootstrapping-argument as in [11] to get existence of a solution. Let $(\omega, s_\star)$ be as in Theorem 4.6 and let us assume

$$s \in \Sigma := \left\{\sigma \in \mathrm{Lip}((0,T])| \quad 0 \leq \dot{\sigma} \leq \frac{H}{\epsilon}, \sigma(0) = s_\star^0\right\}$$

where H is the constant in (4.21). This is a convex and compact subset of the Banach space $C([0,T])$ in the max-norm. We now define analogue to [11] a transform $\mathcal{T}[\sigma]$ via

$$\mathcal{T}[\sigma](t) := s_\star^0 + \int_0^t \frac{(\partial_s \omega(s,\tau))\,|_\sigma}{\omega_0(\sigma(\tau)) - 1} d\tau.$$

Please note, that a fixed point of $\mathcal{T}$ is a solution of the PDE. It is easy to see we have

$$\frac{H}{\epsilon} \geq \frac{d}{dt}\mathcal{T}[\sigma](t) = \frac{(\partial_s \omega(s,t))\,|_\sigma}{\omega_0(\sigma) - 1} \geq 0.$$

Additionally our previous Theorem 4.6 gives us $\mathcal{T}[\sigma] \in C^1((0,T]) \cap \mathrm{Lip}([0,T])$, thus $\mathcal{T} : \Sigma \to \Sigma$ follows.

It is not hard to also show $\mathcal{T}$ being continuous in the max-norm, thus Schauder's fixed-point theorem gives us the existence of a solution. In more detail, in the following we have

$$\begin{aligned}\mathcal{T}[\sigma_1](t) - \mathcal{T}[\sigma_2](t) &\leq \frac{1}{\epsilon}\int_0^t (\partial_s \omega(s,t))\,|_{\sigma_1 -} - (\partial_s \omega(s,t))\,|_{\sigma_2 -} dt \\ &\leq t\tilde{C}H\|\sigma_1 - \sigma_2\|_{\infty,t}\end{aligned}$$

since $\partial_s \omega$ is continuous.

We showed in Theorem 4.6 the necessary properties of our system needed for the existence of a solution following [11] where e.g. [46] shows a different proof based on similar properties. We now sketch the monotone dependence on the initial data, following the latter, which results in an Uniqueness-argument. Let $(\omega_1, s_{\star,1})$ and $(\omega_2, s_{\star,2})$ be solutions of system (4.18) with $s^0_{\star,1} \leq s^0_{\star,1}$ and $\omega_{0,1} \leq \omega_{0,2}$, then $s_{\star,1} \leq s_{\star,2}$ follows, see [46] Theorem 17.2.1. We then can deduce that there is a unique solution. The proof is based on the application of the Maximum Principle together with the Uniqueness Theorem for parabolic equations, see [46], Theorem 1.6.4. We refer the reader for more details of the complete proof to [46], Chapter 17. An alternative proof can be found in [11], Chapter 1.5. □

We now transfer our results to the problem in ρ and x. Initial datum as in (4.19) leads to $\omega > 0$. Therefore corresponding ρ_0 implies $\rho > 0$ holds for all time t. Positivity of ω results in (4.12) being monotone, regularity-results guarantee continuity. Same results can be transferred since we have

$$\partial_s = \omega \partial_x = \frac{1}{\rho}\partial_x$$

we can trace back (4.24) to our one-sided problem (4.18) and apply Theorem 4.7. We hereby sketched the proof of the following Lemma for the one-sided problem in ρ and x.

Corollary 4.8. *The system*

$$\partial_t \rho(x,t) = \partial_x^2 \left(1 - \frac{1}{\rho(x,t)}\right)_+, \tag{4.24a}$$

$$\rho(0,t) = \rho(x_\star(t),t) = 1,$$

$$0 < \rho_0(x) < \frac{1}{1+\epsilon}, \ \textit{for } x < x_\star,$$

$$\rho_0(x) > 1, \ \textit{for } x > x_\star,$$

$$\dot{x}_\star(t) = \frac{\left(\partial_x \frac{1}{\rho(x_\star(t)-,t)}\right)}{1 - \rho_0(x_\star+)}. \tag{4.24b}$$

has a unique solution for ρ_0 corresponding to (4.21). The solution has the same regularity corresponding to (4.20).

4.3.3 Existence of a solution in the general case via a rigorous limit

The formal macroscopic limit taken in Section 4.3.1 will be made rigorous in this section. We will proceed in multiple steps for convenience of the reader. We introduce first the discrete weak formulation of problem (4.5). In the next step, we perform the limit on the left-hand side of our model, in the time derivative. In the third step, we perform the limit on the right-hand side. Control over the TV (TV) of the discrete solutions will be sufficient to be able to pass to the limit on the nonlinear right-hand side. A brief overview about the TV can be found in Appendix 4.5.2. In step 4, we will see that for monotone initial data we obtain boundedness of the TV of the limiting sequence, allowing us to pass to the limit. We then extend this idea to the general case in step 5 to show existence in the main result Theorem 4.11.

1. Weak formulation

The **weak formulation** of the macroscopic model (4.10) up to time $T > 0$ is given by

$$\int_0^1 \int_0^T \omega(s,t)\dot{\varphi}(s,t)\,dt\,ds - \int_0^1 \omega(s,0)\varphi(s,0)\,ds + \int_0^T \int_0^1 \partial_s^2\varphi(s,t)\,(1-\omega(s,t))_+\,ds\,dt = 0$$

for a suiting test-function φ. Now remember $N = C/\Delta s$ and let us define the sequence $\{\omega^N(s,t)\}_N$, $s \in [0,1]$, $t \in \mathbb{R}_+$ as

$$\omega^N(s,t) := \sum_{i=0}^{N-1} \frac{x_{i+1}(t) - x_i(t)}{\Delta s} \mathbb{1}_{[s_i,s_{i+1})}(s) = \sum_{i=0}^{N-1} \omega_{i+\frac{1}{2}}(t)\mathbb{1}_{[s_i,s_{i+1})}(s), \tag{4.25}$$

which can be seen as a discretization of ω. In order to show that the limit function ω also fulfils the macroscopic differential equation (4.10) we will use the **discrete weak formulation** of the interaction operator for the density. Let therefore $\varphi : [0,1] \times [0,T] \to \mathbb{R}$ be a suitable test-function.We denote $\varphi_i(t) := \varphi(s_i,t)$, for $t \in [0,T]$. In more detail, analogous to (4.25), we also introduce

$$\varphi^N(s,t) := \sum_{i=0}^{N-1} \varphi_i(t)\mathbb{1}_{[s_i,s_{i+1})}(s). \tag{4.26}$$

The discrete weak formulation in s-direction is therefore of the form

$$\begin{aligned}
\Delta s \sum_{i=0}^{N-1} \dot{\omega}_{i+\frac{1}{2}}\varphi_i =& \Delta s \sum_{i=1}^{N-2} \frac{2\left(1-\omega_{i+\frac{1}{2}}\right)_+ - \left(1-\omega_{i-\frac{1}{2}}\right)_+ - \left(1-\omega_{i+\frac{3}{2}}\right)_+}{\Delta s^2}\varphi_i \\
&+ \frac{2\left(1-\omega_{\frac{1}{2}}\right)_+ - \left(1-\omega_{\frac{3}{2}}\right)_+}{\Delta s}\varphi_0 + \frac{2\left(1-\omega_{N-\frac{1}{2}}\right)_+ - \left(1-\omega_{N-\frac{3}{2}}\right)_+}{\Delta s}\varphi_{N-1} \\
=& -\Delta s \sum_{i=1}^{N-2} \frac{\varphi_{i-1} - 2\varphi_i + \varphi_{i+1}}{\Delta s^2}\left(1-\omega_{i+\frac{1}{2}}\right)_+ \\
&+ \frac{2\varphi_0 - \varphi_1}{\Delta s}\left(1-\omega_{\frac{1}{2}}\right)_+ + \frac{2\varphi_{N-1} - \varphi_{N-2}}{\Delta s}\left(1-\omega_{N-\frac{1}{2}}\right)_+ .
\end{aligned} \tag{4.27}$$

as already introduced in the context of (4.8). Using (4.27), we obtain that for a test-function $\varphi = \varphi(s,t)$ the weak formulation of the dynamics of ω^N in s and t is of the form

$$\begin{aligned}
\Delta s \sum_{i=0}^{N-1} \int_0^T \dot{\omega}_{i+\frac{1}{2}}\varphi_i dt = -\int_0^T \Bigg[& \Delta s \sum_{i=1}^{N-2} \frac{\varphi_{i-1} - 2\varphi_i + \varphi_{i+1}}{\Delta s^2}\left(1-\omega_{i+\frac{1}{2}}\right)_+ \\
& + \frac{2\varphi_0 - \varphi_1}{\Delta s}\left(1-\omega_{\frac{1}{2}}\right)_+ + \frac{2\varphi_{N-1} - \varphi_{N-2}}{\Delta s}\left(1-\omega_{N-\frac{1}{2}}\right)_+ \Bigg] dt.
\end{aligned}$$

2. Left-hand side limit

In order to perform the limit on the left hand side we note that from Theorem 4.2.1 we obtain boundedness of ω^N for bounded initial data. Therefore $\omega_{\min} \leq \omega^N(s,0) \leq \omega_{\max}$ implies

$$\omega_{\min} \leq \omega^N(s,t) \leq \omega_{\max}, \quad \forall t > 0, \forall s \in [0,1]. \tag{4.28}$$

The bounds (4.28) of ω^N let us conclude that for all $T > 0$ there exists a subsequence, again denoted by $\{\omega^N\}_N$, and $\omega \in L^1([0,1] \times [0,T])$ such that

$$\omega^N \rightharpoonup \omega, \quad \text{as } N \to \infty \text{ in } L^1([0,1] \times [0,T]), \quad \text{for all} \quad T > 0.$$

Now we integrate by parts with respect to time,

$$\begin{aligned}
&\Delta s \sum_{i=0}^{N-1} \int_0^T \dot{\omega}_{i+\frac{1}{2}} \varphi_i \, dt = \Delta s \sum_{i=0}^{N-1} \left[- \int_0^T \omega_{i+\frac{1}{2}} \dot{\varphi}_i \, dt + \omega_{i+\frac{1}{2}}(T)\varphi(s,T) - \omega_{i+\frac{1}{2}}(0)\varphi(s,0) \right] \\
&= \int_0^1 \left[- \int_0^T \omega^N(s,t) \dot{\varphi}^N(s,t) \, dt + \omega^N(s,T)\varphi^N(s,T) - \omega^N(s,0)\varphi^N(s,0) \right] ds.
\end{aligned}$$

Passing to the limit $N \to \infty$, we obtain

$$- \int_0^1 \int_0^T \omega(s,t) \dot{\varphi}(s,t) \, dt \, ds - \int_0^1 \omega(s,0)\varphi(s,0) \, ds$$

for the left-hand side and a test-function φ being C_0^1 in time t.

3. Right-hand side limit

We first note

$$\frac{\varphi_{i-1} - 2\varphi_i + \varphi_{i+1}}{\Delta s^2} = \partial_s^2 \varphi(s_i, t) + \mathcal{O}(\Delta s^2),$$

which together with notation (4.25) allows us to write the right-hand side as follows

$$- \int_0^T \int_0^1 \partial_s^2 \varphi^N(s,t) \left(1 - \omega^N(s,t)\right)_+ ds dt + \mathcal{O}(\Delta s). \tag{4.29}$$

Non-linear functions and weak convergence do not commute due to e.g. possible high oscillatory behaviour of the ω^N as $N \to \infty$ in (4.29). Therefore we need to ensure enough control of the oscillation and we do this via the **Total-Variation** (TV). See Appendix 4.5.2 for definitions and tools. In the following step we show regularity for our problem in the monotone case.

4. The limit in the monotone case

We now want to use the fact that the TV is easily calculable for monotone functions as in (4.37). However, it is not enough that we use monotone initial data in our model since monotonicity will be violated for e.g. $\omega_{\frac{1}{2}}$ converging to 1. We therefore modify our model (4.5) in the following and show the rigorous limit for it:

I.1) Let $\omega_0 \in BV([0,1])$ and $0 \leq \omega_0$. We denote by ω_0^N its discretisation. Moreover, let $\omega_{i+\frac{1}{2}}^N(0)$ be a monotone increasing sequence in i for all N and we fix $\omega_{\frac{1}{2}}^N$ in time, i.e. $\dot{\omega}_{\frac{1}{2}} = 0$.

For initial data satisfying I.1) together with the additional changes for the left boundary point $\omega_{i+\frac{1}{2}}$ being constant in time, we have the following Lemma visualized in Figure 4.7a.

Lemma 4.9 (Preservation of monotonicity)**.** *Let $\omega_{i+\frac{1}{2}}(0)$ be as in I.1). Then the sequence $\omega_{i+\frac{1}{2}}(t)$ is is monotone in i for all $t > 0$.*

Proof. Assume we have initially strictly ordered sequence

$$\omega_{\frac{1}{2}}(0) < \cdots < \omega_{i+\frac{1}{2}}(0) < \cdots < \omega_{N-\frac{1}{2}}(0)$$

and let $\tilde{t} > 0$ be the smallest time such that there exists an $i \in \{0, \dots, N-1\}$ with

$$\omega_{i-\frac{1}{2}}(\tilde{t}) = \omega_{i+\frac{1}{2}}(\tilde{t}).$$

At that time $\tilde{t}$ the dynamics of $\omega_{i-\frac{1}{2}}$ and $\omega_{i+\frac{1}{2}}$ are given by

$$\dot{\omega}_{i+\frac{1}{2}}(\tilde{t}) = \frac{1}{\Delta s^2}\left[\left(1-\omega_{i+\frac{1}{2}}(\tilde{t})\right)_+ - \left(1-\omega_{i+\frac{3}{2}}(\tilde{t})\right)_+\right] \geq 0,$$

since $\omega_{i+\frac{3}{2}}(\tilde{t}) \geq \omega_{i+\frac{1}{2}}(\tilde{t})$. And

$$\dot{\omega}_{i-\frac{1}{2}}(\tilde{t}) = \frac{1}{\Delta s^2}\left[\left(1-\omega_{i-\frac{1}{2}}(\tilde{t})\right)_+ - \left(1-\omega_{i-\frac{3}{2}}(\tilde{t})\right)_+\right] \leq 0,$$

since $\omega_{i-\frac{3}{2}}(\tilde{t}) \leq \omega_{i-\frac{1}{2}}(\tilde{t})$. □

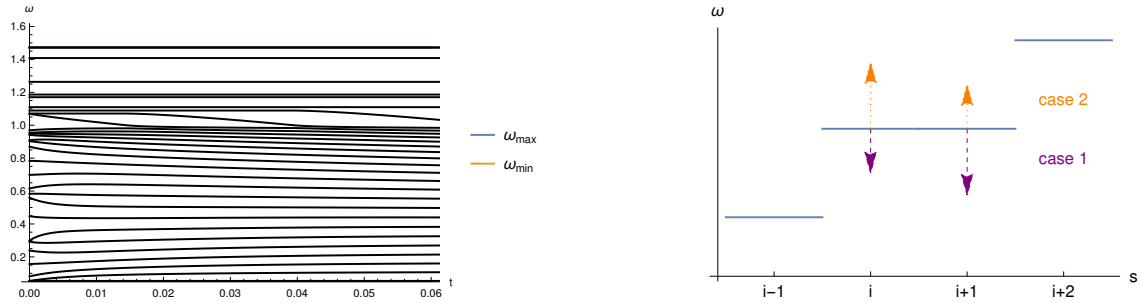

(a) The statement of Lemma 4.9 visualized, the trajectories do not intersect for monotone initial data as in I.1).

(b) The two cases (dashed and dotted) how new minima and maxima can occur, both lead to a contradiction.

Figure 4.7: Ideas for uniform bounds on the TV visualized.

This monotonicity property from Lemma 4.9 is crucial to find uniform bounds on the TV in space, which in the following will allow us to pass to the limit on the right-hand side. Indeed, we can prove the following Lemma:

Lemma 4.10. *Let the initial data fulfil the same assumptions as in Lemma 4.9, then there exists a sequence $\left\{\omega^N\right\}_N$ of solutions to the microscopic model (4.5), which converges to a weak solution of*

$$\begin{aligned} &\partial_t \omega(s,t) = -\partial_s^2 \left(1-\omega(s,t)\right)_+, \\ &\omega(0,t) = \omega_{\frac{1}{2}}(0) \\ &\left(1-\omega(1,t)\right)_+ = 0, \\ &\omega(s,0) = \omega_0(s). \end{aligned} \tag{4.30}$$

in $L^1([0,T);\, L^1([0,1]))$*, for every fixed but arbitrary time* $T>0$*. In other words, System* (4.30) *with monotone initial datum* $\omega_0 \in BV([0,1])$ *has a weak solution in* $L^1([0,T);\, L^1([0,1]))$*.*

Proof. In order to be able to pass to the limit on the right-hand side in (4.29), we aim to show compactness of the limiting sequence $\{\omega^N\}_N$ in $L^1\left([0,T);\, L^1[0,1]\right)$. For this, we shall apply a classical result from [205] regarding characterisation of compactness in spaces of the form $L^p\left([0,T);\, B\right)$ via interpolation, with B being a Banach space, in our case $B = L^1([0,1])$.

We start by first observing that due to the maximum-principle (4.28), ω^N has a bound, uniform in N, in the space $L^\infty([0,T);\, L^1[0,1])$ given by

$$\|\omega^N\|_{L^\infty([0,T);\, L^1(0,1))} \leq T\omega_{max}.$$

Next we see that due to the monotonicity assumption I.1) we have uniform control over the TV in s-direction. Indeed, for every $t \in [0,T)$ we calculate

$$TV(\omega^N(\cdot,t)) := \sum_{i=0}^{N-2} \left|\omega_{i+\frac{3}{2}}(t) - \omega_{i+\frac{1}{2}}(t)\right| = \omega_{N-\frac{1}{2}}(t) - \omega_{\frac{1}{2}}(t) \leq \omega_{\max} - \omega_{\min},$$

where we again used (4.28). This crucial observation gives us an N-independent bound of $\{\omega^N\}$ in $L^1_{loc}\left([0,T); BV([0,1])\right)$.

Moreover, the above bound on the TV also ensures an uniform bound on the set of time derivatives of the sequence $\{\dot\omega^N\}_N$ in $L^1_{loc}\left([0,T); W^{-1,\infty}([0,1])\right)$. Indeed, for every $\varphi \in W^{1,\infty}([0,1])$ we can estimate

$$\begin{aligned}\left|\int_0^1 \dot\omega^N(s,t)\varphi^N(s)ds\right| &= \left|\sum_{i=1}^{N-2} \frac{J_{i+1}(t)-J_i(t)}{\Delta s}\varphi^N(s)\Delta s\right| = \left|\Delta s \sum_{i=1}^{N-2} J_i(t)\frac{\varphi_{i+1}-\varphi_i}{\Delta s}\right| \\ &\leq \|\partial_s\varphi^N\|_{L^\infty([0,1])}\Delta s \sum_{i=1}^{N-2}|J_i(t)| \leq TV(\omega^N(\cdot,t)) \leq \omega_{\max}-\omega_{\min},\end{aligned}$$

where φ^N is defined as in (4.26). We used the abbreviation

$$J_i(t) := \frac{\left(1-\omega_{i+\frac{1}{2}}(t)\right)_+ - \left(1-\omega_{i-\frac{1}{2}}(t)\right)_+}{\Delta s}, \qquad i \in \{1,\dots,N-1\},$$

analogous to (4.14) for the flux governing the dynamics, i.e.

$$\dot\omega^N_{i+\frac{1}{2}}(t) = \frac{J_{i+1}(t)-J_i(t)}{\Delta s}.$$

The resulting fact that $\{\dot\omega^N\}$ is uniformly bounded in the space $L^1_{loc}\left([0,T); W^{-1,\infty}([0,1])\right)$ together with the observation that $BV([0,1]) \subset L^q(0,1) \subset W^{-1,1}(0,1)$, while noting that the first inclusion is compact [[153], Corollary 3.49]. This allows us to conclude that the sequence $\{\omega^N\}_N$ is relatively compact in $L^p\left([0,T);[0,1]\right)$ for every $p<\infty$. Especially, we obtain relative compactness in $L^1\left([0,T); L^1[0,1]\right)$, which concludes the proof since it allows us to pass to the limit in (4.29). □

5. The limit in the general case.

One can extend the above result shown for the problem with monotone initial data to the general case by dividing the limiting sequence into its monotone parts where the above arguments concerning

the TV can be applied. This, of course, is only possible provided one has a bound uniform in N and in time on the number of parts, where ω^N is monotone. While it is clear from the construction of ω^N that the index N does not have influence on the number of extrema, a little more arguments are needed in order to show that the number of minima and maxima cannot increase with respect to time.

Therefore, let us assume that at time $s \geq 0$ we have three points in monotone order, without loss of generality we consider them to be monotonically increasing, i.e. $\omega_{i-\frac{1}{2}}(s) < \omega_{i+\frac{1}{2}}(s) < \omega_{i+\frac{3}{2}}(s)$. Should a new extremum occur, there has to be a time $\tilde{t} > s$ such that, again without loss of generality, $\omega_{i+\frac{1}{2}}(\tilde{t}) = \omega_{i+\frac{3}{2}}(\tilde{t})$ and $\omega_{i+\frac{1}{2}}(t) > \omega_{i+\frac{3}{2}}(t)$ for $t > \tilde{t}$ have to hold. To create such a situation, the velocity of the $i+\frac{1}{2}$-th particle has to be bigger than the one of the $i+\frac{3}{2}$-th particle, which leads to the condition

$$\omega_{i+\frac{5}{2}}(\tilde{t}) < \omega_{i-\frac{1}{2}}(\tilde{t}).$$

Due to continuity, also $\omega_{i+\frac{5}{2}}(t) < \omega_{i-\frac{1}{2}}(t)$ had to hold for $t \in [\underline{t}, \tilde{t}]$ for some $\underline{t} < \tilde{t}$. Hence,

$$\omega_{i+\frac{5}{2}}(t) < \omega_{i-\frac{1}{2}}(t) < \omega_{i+\frac{1}{2}}(t) < \omega_{i+\frac{3}{2}}(t), \quad t \in [\underline{t}, \tilde{t}],$$

and

$$\omega_{i+\frac{1}{2}}(t) < \omega_{i+\frac{3}{2}}(t) < \omega_{i-\frac{5}{2}}(t), \quad \omega_{i-\frac{1}{2}}(t) < \omega_{i+\frac{1}{2}}(t), \quad t > \tilde{t},$$

which means that a previously existing maximum at $\omega_{i+\frac{3}{2}}$ changed position to $\omega_{i+\frac{1}{2}}$, but no new extremum occurred. Similar arguments for the case of three monotonically decreasing points leads to the conclusion that extrema can only change position, but no new can occur while time evolves.

That is enough to show the following Theorem of existence.

Theorem 4.11 (Existence of a solution)**.** *Let $\omega_0 \in BV([0,1])$ hold, then there exists a sequence $\left\{\omega^N\right\}_N$ of solutions to the microscopic model (4.5), which converges to a weak solution of*

$$\begin{aligned} &\partial_t \omega(s,t) = -\partial_s^2 \left(1-\omega(s,t)\right)_+, \\ &\left(1-\omega(0,t)\right)_+ = \left(1-\omega(1,t)\right)_+ = 0, \\ &\omega(s,0) = \omega_0(s). \end{aligned} \tag{4.31}$$

in $L^1([0,T); L^1([0,1]))$, for every fixed but arbitrary time $T > 0$. In other words, System (4.31) with monotone initial datum $\omega_0 \in BV([0,1])$ has a weak solution in $L^1([0,T); L^1([0,1]))$.

We see that in this case the existence of the solution is also independent of the jump condition (4.22). We also formulate our result in ρ before concluding with numerical experiments.

Proof. Let M be the number of extrema of ω_0^N. The argument above as well as (4.28) let us conclude that M is an upper bound on the number of extrema of $\omega^N(t)$, for all $t > 0$, which allows us to estimate

$$TV(\omega^N(\cdot,t)) \leq M\left(\omega_{max} - \omega_{min}\right),$$

again independent of N. The remainder of the proof can be done as in the proof of Lemma 4.10. □

Corollary 4.12. *Let $\rho_0 \in BV([a,b])$, where $[a,b] \subset \mathbb{R}$ is a closed interval. Then system*

$$\begin{aligned} &\partial_t \rho(s,t) = \partial_x^2 \left(1 - \frac{1}{\rho(x,t)}\right)_+, \\ &\rho(x,0) = \rho_0(x). \end{aligned}$$

has a weak solution in $L^1([0,T); L^1([0,1]))$.

4.3.4 Numerical simulations on a macroscopic level

We investigate problem (4.24) on an open domain $\mathbb{R}$ with $\rho_0 > 0$. Therefore we discretize equation (4.24a) as $\rho(i\Delta x, j\Delta t) = \rho_i^j$ explicit in time via

$$\rho_i^{j+1} = \rho_i^j + \frac{\Delta t}{\Delta x^3}\left[(1 - 1/\rho_{i+1}^j)_+ - 2(1 - 1/\rho_i^j)_+ + (1 - 1/\rho_{i-1}^j)_+\right]. \tag{4.32}$$

Here we discretized the Laplacian as usual.

We choose $\Delta x = 0.001$ for a sharp visualisation of the shock and $\Delta t = 0.1\Delta x^2$ in compliance with typical CFL-conditions, following classical literature, see [150]. In Figure (4.8a) we see the smoothening-effect for non-continuous initial data of system (4.24) for $\rho_0 > 1$.

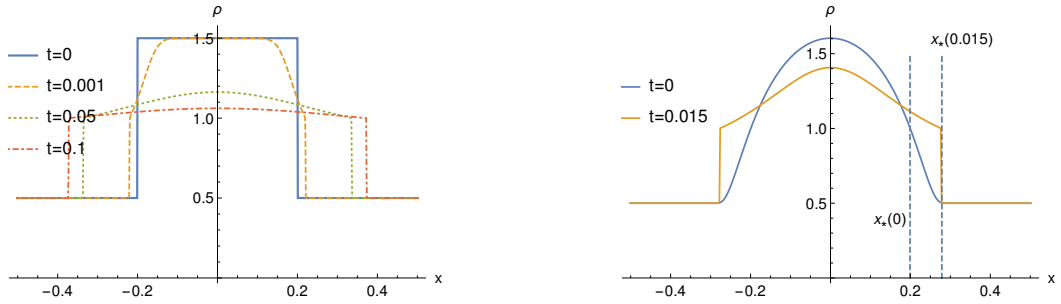

(a) Non-continuous initial data, we see the smoothening effect of (4.24).

(b) Smooth initial-data and the position of the shock $x_\star$ calculated from (4.24b).

Figure 4.8: Macroscopic simulations for a two-sided problem.

In Figure (4.8b) we also plot the position of the jump $x_\star$ calculated via (4.24b). We used for the discretization of (4.24b) an explicit Euler algorithm for solving the ODE. Knowing $x_\star$ is monotone increasing and considering the left- and right-handed limits, we used in the numerator a Downwind- and for the Denominator an Upwind-approach. We see that the discretisation (4.32) creates the correct shock-speed. Additionally continuous initial data as in (4.19) leads to satisfying results since as mentioned, the discontinuity only occurs for $t = 0$ and (4.17) is Lipschitz for $t > 0$.

4.4 Conclusion and Outlook

4.4.1 Applications and open questions

In the following, we mention two possible combinations for the new diffusion term $\partial_x^2\left(1 - \frac{1}{\rho(x,t)}\right)_+$. The authors assume that both suggested models can presumably be derived microscopically.

Bacterial Growth

A classical growth term is exponential growth, which is well known to describe bacteria, see [166],

$$\partial_t \rho(x,t) = \rho(x,t).$$

This new diffusive effect needs to be investigated in the context of cell-exclusion, occurring in bacterial growth. This was done on a microscopic level by e.g. [66]. In a well known biological experiment, see [225], quite natural a version of a one-sided problem is investigated. Bacteria divide, and can leave

a one-dimensional channel only on one side. The other has mathematically seen No-Flux boundary conditions. The experiment was done to investigate a growth-rate $\alpha > 0$. In our case, this corresponds to a one-sided problem with a source-term, e.g. in

$$\partial_t \rho(x,t) = \partial_x^2 \left(1 - \frac{1}{\rho(x,t)}\right)_+ + \alpha\rho(x,t).$$

From a mathematical perspective, questions regarding the existence of solutions and blow-ups are natural. The biological problem was investigated already with different technics, see [191], and this new diffusive term can broaden the perspective.

Alignments within a drift

We have shown how our diffusive term results in a desired density at the microscopic and macroscopic levels. In addition, this term can be studied in systems with drift, for example, due to an external potential φ. If we motivate the drift term similar to a linear Fokker-Planck equation, it leads us to the following equation

$$\partial_t \rho(x,t) = \partial_x \left(\partial_x \left(1 - \frac{1}{\rho(x,t)}\right)_+ + \rho(x,t)\partial_x \varphi(x)\right)$$

with φ being a suitable potential depending on x. This model has applications in 1D and 2D, see e.g. the self-organising system of birds during their travels, visualized in Figure 4.9.

The diffusion term D leads to a desired density ρ of 1, scaled here, but unlike macroscopic models based on cellular automata with cell exclusion, this can be exceeded and solve problems in modelling and calibration in the context of pedestrian dynamics, see [80, 94]. This new diffusion allows to introduce a parameter for the desired density ρ_d quite simply via

$$\partial_x^2 \left(1 - \frac{\rho_d}{\rho(x,t)}\right)_+ .$$

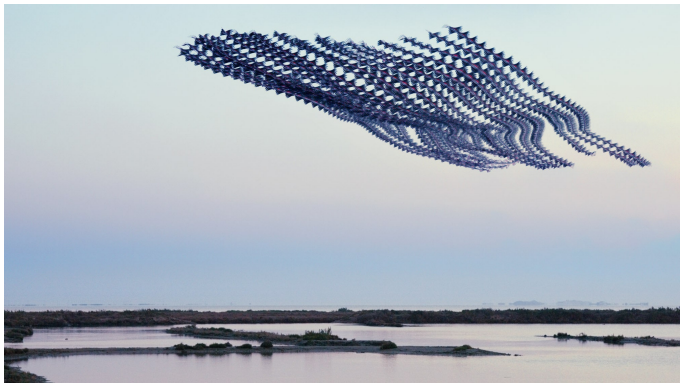

Figure 4.9: Birds showing a local diffusive effect, aligning in similar distance to each other on their travel. Image thankfully provided by the photographer, see [3].

2D-setting

In the case of 2D even the formal derivation of the macroscopic model is an open question. The alignment in 1D arising from Lagrangian coordinates s was a key component to introduce the discrete

(a) Voronoi-diagram of random initial data in 2D.

(b) Corresponding Delaunay-diagram, it is the dual graph.

Figure 4.10: The Voronoi-diagramms partitions the plane into sets s_i where x_i is the closest, while the Delaunay-diagram connects interacting particles based on the first.

density ρ. Nearby ideas of the authors is investigating the problem in 2D using e.g. Delaunay- and or Voroi-diagramms in combination with Lagrange-coordinates as in Figure 4.10. The latter are typical in measuring density in pedestrian dynamics, see [6], while the dual graph, the Delaunay-triangulation, see [171], can be used to define the interacting particles.

4.4.2 Summary and Conclusion

In this work we modelled particles interacting in a certain radius. We introduce the scaled distance ω, which can also be seen as a derivative in Lagrangian coordinates s. From this, we it was possible to define a microscopic density ρ.

For the microscopic systems (4.2) and (4.5) we could proof strong statements and underline them with simulations. Properties of (4.5) can be transferred to the density.

On a macroscopic level our main focus was on (4.10) and (4.13), conservation laws for which we can derive jump conditions of the non-differentiability in $(1 - .)_+$. We outline how a global theory of existence for system (4.13) can be constructed, based on the decomposition of the problem to minimal one-sided versions in Lagrangian coordinates. Mentioned jump condition corresponds to the moving boundary of a Stefan problem, whose theory we used to show the existence and uniqueness of a solution in the regularized case of the one-sided problem. An alternative to this is a rigorous limit to transfer the existence of a solution of the ODE system to the PDE. Due to non-differentiability in the systems, this approach is non-trivial. To find a weakly convergent sequence for system (4.5), we choose the technique of total variation TV. This seems to be a suitable tool to show the limit even in more general cases but is beyond the scope of this paper. As outlined, this new diffusion term itself requires more intensive investigation. To emphasize this, we have presented in this Section 4.4 possible applications and possible combinations with already known terms from modelling.

4.5 Appendix

4.5.1 An improved regularity result for parabolic equations

The following is an adaption of Theorem 5 in [77], Chapter 7 for time-dependent coefficients. The parabolic problem

$$\begin{aligned} \partial_t v(y,t) &= a(t)\partial_y^2 v(y,t) + b(y,t)\partial_y v(y,t) \quad \text{in } (0,1)\times(0,T) \\ v(0,t) &= v(1,t) = 1 \\ v(y,0) &= v_0(y) \end{aligned} \tag{4.33a}$$

has a unique weak solution for $a \in L^\infty([0,T])$, $b \in L^\infty([0,1]\times[0,T])$ following Theorem 3 and 4 in [77], Chapter 7. Theorem 5 then shows stronger regularity-results with a, b time-independent.

Let in the following a, b be time-dependent, whereas the following regularity-result is an adaption of Theorem 5 to show improved regularity of (4.23). In our model we have $a(t) = \frac{1}{s_\star^2(t)}$ and $b(y,t) = \frac{y\dot{s}_\star(t)}{s_\star(t)}$ which are bounded due our regularisation via (4.21) for $\dot{s}_\star$ defined in (4.15). We will sketch that a solution v of (4.33) fulfils

$$v \in L^2\left(0,T; H^2([0,1])\right) \cap L^\infty\left(0,T; H_0^1([0,1])\right). \tag{4.34}$$

The author in [77] uses a discrete Galerkin approximation v_m. We will derive the needed bounds for passing to the limit $m \to \infty$ using the notation introduced in [77], Chapter 6 and 7. To abbreviate, the following calculations are done for homogeneous Dirichlet boundary conditions. It is well known, we refer to mentioned book Chaper 3, and discussed it ourself shortly in Subsection 4.3.1, this does not present a problem.

Equation (4.33a) in weak formulation has the following form

$$(\partial_t v_m, \partial_t v_m) + \mathcal{L}[v_m, \partial_t v_m] = 0$$

for almost everywhere $0 \le t \le T$ and $\mathcal{L}$ being our differential operator. We now investigate bounds for $\mathcal{L}$ to pass to the limit. We have

$$\mathcal{L}[v_m, \partial_t v_m] = \int_0^1 a(t)(\partial_y v_m)(\partial_t \partial_y v_m)dy + \int_0^1 b(y,t)(\partial_y v_m)(\partial_t v_m)dy =: \mathcal{A} + \mathcal{B}.$$

We find estimates using Cauchy-Schwartz

$$|\mathcal{B}| = \int_0^1 b(y,t)(\frac{1}{\delta}\partial_y v_m)(\delta \partial_t v_m)dy \le c_2\left(\frac{c_1}{\delta}\|v_m\|_{H_0^1([0,1])} + \delta\|\partial_t v_m\|_{L^2([0,1])}\right) \tag{4.35}$$

for every $\delta > 0$. The constant c_2 depends on $\sup_{[0,1]}(b)$, in model (4.23) we have $|b(y,t)| \le \frac{H/\epsilon}{s_\star(0)}$ due our regularisation. We rewrite $\mathcal{A}$ as

$$\mathcal{A} = \int_0^1 a(t)(\partial_y v_m)(\partial_t \partial_y v_m)dy = a(t)\int_0^1 (\partial_y v_m)(\partial_t \partial_y v_m)dy = a(t)\partial_t\left(\frac{1}{2}A[v_m, v_m]\right) \tag{4.36}$$

with A being a symmetric bilinear form

$$A[v_m, u_m] = \int_0^1 (\partial_y v_m)(\partial_y u_m)dy, \quad v_m, u_m \in H_0^1([0,1]).$$

Combining (4.35), (4.36), choosing $\delta = \frac{1}{2}$ and integrating over t as in [77] we get

$$\begin{aligned}
&\int_0^T \|\partial_t v_m\|^2_{L^2([0,1])} + \sup_{0\le t\le T}|a(t)| \sup_{0\le t\le T} A[v_m(t), v_m(t)] \\
&\le c_3 \left(A[v_m(0), v_m(0)] + \int_0^T \|v_m\|^2_{H_0^1([0,1])} dt \right) \\
&\le c\|v_0\|^2_{H_0^1([0,1])}
\end{aligned}$$

where c_3 now also depends on $\sup|a(t)|$. We want to note briefly that no regularization was needed for the bounds on a in our example, because $s_\star$ is monotonically increasing. For the second inequality we used the energy estimates in Theorem 2 Chapter 7 in mentioned [77], in more detail we have for our approximations v_m the following estimate

$$\|v_m(0)\|_{H_0^1([0,1])} \le \|v_0\|_{H_0^1([0,1])}.$$

Additionally we use $A[v,v] \ge \int_0^1 |\partial_y v|^2 dy$ for every $v \in H_0^1([0,1])$. Combining everything we have

$$\sup_{0\le t\le T} \|v_m(t)\|^2_{H_0^1([0,1])} \le c\|v_0\|^2_{H_0^1([0,1])}.$$

We then can pass to limits $m \to \infty$ and deduce $v \in L^\infty(0,T; H_0^1([0,1])$ and $\partial_t v \in L^2(0,T; L^2([0,1])$. We than can follow step 3 of the mentioned proof to receive the higher regularity (4.34).

4.5.2 Lemmas and Definitions in the context of TV and BV

We repeat in the following definitions and Lemmas needed throughout the calculations and estimates in Section 4.3.3. We start with a short introduction of the **Total Variation** (TV) for piecewise-functions. Let $\omega^N(s) = \sum_{i=0}^{N-1} \omega_{i+\frac{1}{2}} \mathbb{1}_{[s_i, s_{i+1})}(s)$ be a piece-wise function in s with respect to the grid $\{s_0, \dots, s_N\}$, then its TV is given, following e.g. [206], via

$$TV\left(\omega^N(s)\right) := \sum_{i=1}^{N-1} \left| \omega_{i+\frac{1}{2}} - \omega_{i-\frac{1}{2}} \right|.$$

For (in space s) monotone increasing ω^N the previous definition results in

$$TV(\omega^N(s)) = \left| \omega_{N-\frac{1}{2}} - \omega_{\frac{1}{2}} \right|. \tag{4.37}$$

The **set of all functions with bounded variation**is denoted by $BV([0,1])$.

Bibliography

[1] Bradley-terry model. https://www.encyclopediaofmath.org//index.php?title=Bradley-Terry_model&oldid=22181. Accessed: 2020-03-02.

[2] Brazil vs. germany: Goalimpact of lineups. http://www.goalimpact.com/blog//2014/07/brazil-vs-germany-goalimpact-of-lineups.html. Accessed: 2021-08-30.

[3] Xavi bou. https://www.xavibou.com/contact/. Accessed: 2022-03-30.

[4] Crowding and queuing at entrances, 2018. http://ped.fz-juelich.de/da/doku.php?id=wuptmp.

[5] Jupedsim, 2019. https://www.jupedsim.org.

[6] J. Adrian, M. Boltes, S. Holl, A. Sieben, and A. Seyfried. Crowding and queuing in entrance scenarios: influence of corridor width in front of bottlenecks. *arXiv preprint arXiv:1810.07424*, 2018.

[7] G. Albi, L. Pareschi, G. Toscani, and M. Zanella. *Recent advances in opinion modeling: control and social influence*. Birkhäuser, Cham, 2017.

[8] G. Albi, L. Pareschi, and M. Zanella. Boltzmann-type control of opinion consensus through leaders. *Philosophical Transactions of the Royal Society A: Mathematical, Physical and Engineering Sciences*, 372(2028):20140138, 2014.

[9] G. Albi, L. Pareschi, and M. Zanella. Boltzmann games in heterogeneous consensus dynamics. *J. Stat. Phys.*, 175(1):97–125, 2019.

[10] A. Almet, M. Pan, B. Hughes, and K. Landman. When push comes to shove: Exclusion processes with nonlocal consequences. *Physica A: Statistical Mechanics and its Applications*, 437, 05 2015.

[11] D. Andreucci. Lecture notes on the stefan problem. *Lecture notes, Universitá da Roma La Sapienza, Italy*, 2004.

[12] K. Anguige and C. Schmeiser. A one-dimensional model of cell diffusion and aggregation, incorporating volume filling and cell-to-cell adhesion. *Journal of mathematical biology*, 58(3):395–427, 2009.

[13] C. S. Applegate, S. D. Laycock, and A. M. Day. Real-time traffic simulation using cellular automata. In *TPCG*, pages 91–98, 2010.

[14] A. Aron and E. N. Aron. *Statistics for psychology*. Prentice-Hall, Inc, 1999.

[15] G. Arumugam and J. Tyagi. Keller-segel chemotaxis models: a review. *Acta Applicandae Mathematicae*, 171(1):1–82, 2021.

[16] M. Bardi and I. Capuzzo-Dolcetta. *Optimal Control and Viscosity Solutions of Hamilton-Jacobi-Bellman Equations*. Modern Birkhäuser Classics. Birkhäuser Boston, 2008.

[17] S. Bartels. Total variation minimization with finite elements: convergence and iterative solution. *SIAM Journal on Numerical Analysis*, 50(3):1162–1180, 2012.

[18] H. Benaroya and S. Han. *Probability models in engineering and science*. Taylor & Francis, 2013.

[19] D. Benedetto, E. Caglioti, and M. Pulvirenti. A kinetic equation for granular media. *ESAIM: Mathematical Modelling and Numerical Analysis*, 31(5):615–641, 1997.

[20] E. Bernardi, L. Pareschi, G. Toscani, and M. Zanella. Effects of vaccination efficacy on wealth distribution in kinetic epidemic models. *Entropy*, 24(2):216, 2022.

[21] M. Bicher. *Classification of microscopic models with respect to aggregated system behaviour*. PhD thesis, Technische Universität Wien, 2017.

[22] M. Bicher, C. Urach, and N. Popper. Gepoc abm: a generic agent-based population model for austria. In *2018 Winter Simulation Conference (WSC)*, pages 2656–2667. IEEE, 2018.

[23] A. Blanchet and P. Degond. Kinetic models for topological nearest-neighbor interactions. *Journal of Statistical Physics*, 169(5):929–950, 2017.

[24] J. Blitzstein and J. Hwang. *Introduction to Probability*. Chapman & Hall/CRC Texts in Statistical Science. CRC Press/Taylor & Francis Group, 2014.

[25] V. J. Blue and J. L. Adler. Cellular automata microsimulation for modeling bi-directional pedestrian walkways. *Transportation Research Part B: Methodological*, 35(3):293–312, 2001.

[26] F. Bolley, J. A. Cañizo, and J. A. Carrillo. Mean-field limit for the stochastic vicsek model. *Applied Mathematics Letters*, 25(3):339–343, 2012.

[27] L. Boltzmann. Weitere studien über das wärmegleichgewicht unter gasmolekülen. In *Kinetische Theorie II*, pages 115–225. Springer, 1970.

[28] L. Boltzmann. Further studies on the thermal equilibrium of gas molecules. In *The kinetic theory of gases: an anthology of classic papers with historical commentary*, pages 262–349. World Scientific, 2003.

[29] L. Boudin and F. Salvarani. Opinion dynamics: kinetic modelling with mass media, application to the Scottish independence referendum. *Physica A*, 444:448–457, 2016.

[30] R. A. Bradley and M. E. Terry. Rank analysis of incomplete block designs: I. the method of paired comparisons. *Biometrika*, 39(3/4):324–345, 1952.

[31] M. Bruna, M. Burger, H. Ranetbauer, and M.-T. Wolfram. Cross-diffusion systems with excluded-volume effects and asymptotic gradient flow structures. *Journal of Nonlinear Science*, 27(2):687–719, 2017.

[32] M. Bruna and S. J. Chapman. Diffusion of multiple species with excluded-volume effects. *The Journal of chemical physics*, 137(20):204116, 2012.

[33] M. Bruna and S. J. Chapman. Excluded-volume effects in the diffusion of hard spheres. *Physical Review E*, 85(1):011103, 2012.

[34] M. Burger. Mathematische Modellierung. *Vorlesungsskriptum, Westfälische Wilhelms Universität Münster, Institut für Numerische und Angewandte Mathematik*, 24, 2012.

[35] M. Burger. Network structured kinetic models of social interactions. *Vietnam Journal of Mathematics*, 49(3):937–956, 2021.

[36] M. Burger, L. Caffarelli, P. A. Markowich, and M.-T. Wolfram. On a boltzmann-type price formation model. *Proceedings of the Royal Society A: Mathematical, Physical and Engineering Sciences*, 469(2157):20130126, 2013.

[37] M. Burger, M. Di Francesco, and Y. Dolak-Struss. The Keller–Segel model for chemotaxis with prevention of overcrowding: Linear vs. nonlinear diffusion. *SIAM Journal on Mathematical Analysis*, 38(4):1288–1315, 2006.

[38] M. Burger, M. Di Francesco, J.-F. Pietschmann, and B. Schlake. Nonlinear cross-diffusion with size exclusion. *SIAM Journal on Mathematical Analysis*, 42(6):2842–2871, 2010.

[39] M. Burger, S. Hittmeir, H. Ranetbauer, and M.-T. Wolfram. Lane formation by side-stepping. *SIAM Journal on Mathematical Analysis*, 48, 07 2015.

[40] M. Burger, A. Lorz, and M.-T. Wolfram. Balanced growth path solutions of a boltzmann mean field game model for knowledge growth. *Kinetic and Related Models*, 10, 02 2016.

[41] M. Burger, A. Lorz, and M.-T. Wolfram. On a boltzmann mean field model for knowledge growth. *SIAM Journal on Applied Mathematics*, 76(5):1799–1818, 2016.

[42] M. Burger and J.-F. Pietschmann. Flow characteristics in a crowded transport model. *Nonlinearity*, 29(11):3528, Nov 2016.

[43] C. Burstedde, K. Klauck, A. Schadschneider, and J. Zittartz. Simulation of pedestrian dynamics using a two-dimensional cellular automaton. *Physica A: Statistical Mechanics and its Applications*, 295:507–525, 06 2001.

[44] J. C. Butcher. *Numerical methods for ordinary differential equations*. John Wiley & Sons, 2016.

[45] L. Caffarelli and M. Crandall. Distance functions and almost global solutions of eikonal equations. *Communications in Partial Differential Equations*, 35:391–414, 03 2010.

[46] J. R. Cannon and F. E. Browder. *The One-Dimensional Heat Equation*. Encyclopedia of Mathematics and its Applications. Cambridge University Press, 1984.

[47] J. A. Carrillo, Y.-P. Choi, and M. Hauray. The derivation of swarming models: mean-field limit and wasserstein distances. In *Collective dynamics from bacteria to crowds*, pages 1–46. Springer, 2014.

[48] J. A. Carrillo, M. Fornasier, J. Rosado, and G. Toscani. Asymptotic flocking dynamics for the kinetic cucker–smale model. *SIAM Journal on Mathematical Analysis*, 42(1):218–236, 2010.

[49] J. A. Carrillo, M. Fornasier, G. Toscani, and F. Vecil. *Particle, kinetic, and hydrodynamic models of swarming*, pages 297–336. Birkhäuser Boston, Boston, 2010.

[50] C. Cercignani. *The Boltzmann equation and its applications*. Springer, New York, NY, 1988.

[51] C. Cercignani, R. Illner, and M. Pulvirenti. *The mathematical theory of dilute gases*, volume 106. Springer Science & Business Media, 2013.

[52] A. N. Ceretani, N. N. Salva, and D. A. Tarzia. An exact solution to a stefan problem with variable thermal conductivity and a robin boundary condition. *Nonlinear Analysis: Real World Applications*, 40:243–259, 2018.

[53] A. Chakraborti and B. K. Chakrabarti. Statistical mechanics of money: how saving propensity affects its distribution. *The European Physical Journal B-Condensed Matter and Complex Systems*, 17(1):167–170, 2000.

[54] H. Chaté, F. Ginelli, G. Grégoire, F. Peruani, and F. Raynaud. Modeling collective motion: variations on the vicsek model. *The European Physical Journal B*, 64(3):451–456, 2008.

[55] A. Corbetta, J. A. Meeusen, C.-m. Lee, R. Benzi, and F. Toschi. Physics-based modeling and data representation of pairwise interactions among pedestrians. *Physical Review E*, 98:062310, Dec 2018.

[56] S. Cordier, L. Pareschi, and C. Piatecki. Mesoscopic modelling of financial markets. *Journal of Statistical Physics*, 134:161–184, 01 2009.

[57] K. Crane, C. Weischedel, and M. Wardetzky. The heat method for distance computation. *Communications of the ACM*, 60(11):90–99, 2017.

[58] E. Cristiani, B. Piccoli, and A. Tosin. *Multiscale Modeling of Pedestrian Dynamics*. Springer International Publishing, 2014.

[59] E. Cristiani and A. Tosin. Reducing complexity of multiagent systems with symmetry breaking: an application to opinion dynamics with polls. *Multiscale Model. Simul.*, 16(1):528–549, 2018.

[60] F. Cucker and S. Smale. Emergent behavior in flocks. *IEEE Transactions on Automatic Control*, 52(5):852–862, 2007.

[61] W. Daamen, S. P. Hoogendoorn, and P. H. Bovy. First-order pedestrian traffic flow theory. *Transportation research record*, 1934(1):43–52, 2005.

[62] M. E. Davis. *Numerical methods and modeling for chemical engineers*. Courier Corporation, 2013.

[63] P. Degond. Macroscopic limits of the boltzmann equation: a review. *Modeling and computational methods for kinetic equations*, pages 3–57, 2004.

[64] M. Di Francesco, S. Fagioli, and E. Radici. Deterministic particle approximation for nonlocal transport equations with nonlinear mobility. *Journal of Differential Equations*, 266(5):2830–2868, 2019.

[65] M. Di Francesco, P. Markowich, J.-F. Pietschmann, and M.-T. Wolfram. On the Hughes' model for pedestrian flow: the one-dimensional case. *Journal of Differential Equations*, 250(3):1334–1362, 2 2011.

[66] M. Doumic, S. Hecht, and D. Peurichard. A purely mechanical model with asymmetric features for early morphogenesis of rod-shaped bacteria micro-colony. *Mathematical biosciences and engineering : MBE*, 17 6:6873–6908, 2020.

[67] D. C. Duives, W. Daamen, and S. Hoogendoorn. Trajectory analysis of pedestrian crowd movements at a Dutch music festival. In *Pedestrian and Evacuation Dynamics 2012*, pages 151–166. Springer, 2014.

[68] B. Düring, A. Jüngel, and L. Trussardi. A kinetic equation for economic value estimation with irrationality and herding. *Kinet. Relat. Models*, 10(1):239–261, 2017.

[69] B. Düring, P. Markowich, J. Pietschmann, and M. Wolfram. Boltzmann and fokker-planck equations modelling opinion formation in the presence of strong leaders. *Proc. R. Soc. A.*, 465:3687–3708, 2009.

[70] B. Düring, D. Matthes, and G. Toscani. Kinetic equations modelling wealth redistribution: A comparison of approaches. *Phys. Rev. E*, 78:056103, 11 2008.

[71] B. Düring, M. Torregrossa, and M. Wolfram. Boltzmann and fokker-planck equations modelling the elo rating system with learning effects. *J. Nonlinear Sci.*, 29:1095–1128, 2019.

[72] B. Düring and M.-T. Wolfram. Opinion dynamics: inhomogeneous boltzmann-type equations modelling opinion leadership and political segregation. *Proceedings of the Royal Society A: Mathematical, Physical and Engineering Sciences*, 471(2182):20150345, 2015.

[73] M.-C. Duvernoy, T. Mora, M. Ardré, V. Croquette, D. Bensimon, C. Quilliet, J.-M. Ghigo, M. Balland, C. Beloin, S. Lecuyer, et al. Asymmetric adhesion of rod-shaped bacteria controls microcolony morphogenesis. *Nature communications*, 9(1):1–10, 2018.

[74] F. I. D. Echecs. *The Official Laws of Chess and Other Fide Regulations*. Collier Books, 1990.

[75] A. Elo. *The Rating of Chessplayers, Past and Present*. Ishi Press, 1986.

[76] R. Erban and S. J. Chapman. Reactive boundary conditions for stochastic simulations of reaction–diffusion processes. *Physical Biology*, 4(1):16, 2007.

[77] L. C. Evans. *Partial differential equations*. American Mathematical Society, Providence, R.I., 2010.

[78] K. Fellner, L. Neumann, and C. Schmeiser. Convergence to global equilibrium for spatially inhomogeneous kinetic models of non-micro-reversible processes. *Monatshefte für Mathematik*, 141(4):289–299, 2004.

[79] M. Fischer. Local and global pushing on bounded domains. "PDE and Probability for Biology", 2020.

[80] M. Fischer, G. Jankowiak, and M.-T. Wolfram. Micro-and macroscopic modeling of crowding and pushing in corridors. *Networks & Heterogeneous Media*, 15(3), 2020.

[81] F. Font. A one-phase stefan problem with size-dependent thermal conductivity. *Applied Mathematical Modelling*, 63:172–178, 2018.

[82] J. B. J. Fourier. *Théorie de la propagation de la chaleur dans les solides*. 1972.

[83] G. A. Frank and C. O. Dorso. Room evacuation in the presence of an obstacle. *Physica A: Statistical Mechanics and its Applications*, 390(11):2135–2145, 2011.

[84] A. Friedman. Remarks on the maximum principle for parabolic equations and its applications. *Pacific Journal of Mathematics*, 8:201–211, 1958.

[85] M. Fukui and Y. Ishibashi. Self-organized phase transitions in cellular automaton models for pedestrians. *Journal of the physical society of Japan*, 68(8):2861–2863, 1999.

[86] V. García-Morales. Universal map for cellular automata. *Physics Letters A*, 376(40-41):2645–2657, 2012.

[87] Á. Garcimartín, D. Maza, J. M. Pastor, D. R. Parisi, C. Martín-Gómez, and I. Zuriguel. Redefining the role of obstacles in pedestrian evacuation. *New Journal of Physics*, 20(12):123025, 2018.

[88] A. Garcimartín, I. Zuriguel, J. Pastor, C. Martín-Gómez, and D. Parisi. Experimental evidence of the "faster is slower" effect. *Transportation Research Procedia*, 2:760–767, 2014.

[89] C. W. Gardiner et al. *Handbook of stochastic methods*, volume 3. springer Berlin, 1985.

[90] J. Gayon. From mendel to epigenetics: History of genetics. *Comptes rendus biologies*, 339(7-8):225–230, 2016.

[91] D. C. Gazis, R. Herman, and R. W. Rothery. Nonlinear follow-the-leader models of traffic flow. *Operations research*, 9(4):545–567, 1961.

[92] J. W. Gibbs. On the fundamental formula of statistical mechanics, with applications to astronomy and thermodynamics. In *Proceedings of the American Association for the Advancement of Science*, pages 57–58, 1884.

[93] M. Glickman. Parameter estimation in large dynamic paired comparison experiments. *Journal of the Royal Statistical Society: Series C (Applied Statistics)*, 48, 11 1998.

[94] S. N. Gomes, A. M. Stuart, and M.-T. Wolfram. Parameter estimation for macroscopic pedestrian dynamics models from microscopic data. *SIAM Journal on Applied Mathematics*, 79(4):1475–1500, 2019.

[95] S. Göttlich, S. Knapp, and P. Schillen. A pedestrian flow model with stochastic velocities: Microscopic and macroscopic approaches. *arXiv preprint arXiv:1703.09134*, 2017.

[96] H. Grad. Principles of the kinetic theory of gases. In *Thermodynamik der Gase/Thermodynamics of Gases*, pages 205–294. Springer, 1958.

[97] G. Grégoire and H. Chaté. Onset of collective and cohesive motion. *Physical review letters*, 92(2):025702, 2004.

[98] S. Gualandi and G. Toscani. Pareto tails in socio-economic phenomena: a kinetic description. *Economics*, 12(1), 2018.

[99] M. Haghani, M. Sarvi, and Z. Shahhoseini. When 'push'does not come to 'shove': Revisiting 'faster is slower'in collective egress of human crowds. *Transportation research part A: policy and practice*, 122:51–69, 2019.

[100] K. Harkness. *Official Chess Handbook*. D. McKay Co., 1967.

[101] J. Haskovec. Flocking dynamics and mean-field limit in the cucker–smale-type model with topological interactions. *Physica D: Nonlinear Phenomena*, 261:42–51, 2013.

[102] J. Haškovec and C. Schmeiser. Convergence of a stochastic particle approximation for measure solutions of the 2d keller-segel system. *Communications in Partial Differential Equations*, 36(6):940–960, 2011.

[103] F. H. Hassan. Using microscopic pedestrian simulation statistics to find clogging regions. In *2016 SAI Computing Conference (SAI)*, pages 156–160. IEEE, 2016.

[104] B. Hein. *Agent-based modelling for crowding and queuing in front of bottlenecks*. Bachelor's thesis, University of Wuppertal, 2019.

[105] D. Helbing. Similarities between granular and traffic flow. In *Physics of Dry Granular Media*, pages 547–552. Springer, 1998.

[106] D. Helbing, I. Farkas, and T. Vicsek. Simulating dynamical features of escape panic. *Nature*, 407(6803):487–490, 2000.

[107] D. Helbing, A. Johansson, and H. Z. Al-Abideen. Dynamics of crowd disasters: An empirical study. *Physical review E*, 75(4):046109, 2007.

[108] D. Helbing and P. Molnár. Social force model for pedestrian dynamics. *Physical Review E*, 51(5):4282, 1995.

[109] D. Helbing, P. Molnár, I. J. Farkas, and K. Bolay. Self-organizing pedestrian movement. *Environment and planning B: planning and design*, 28(3):361–383, 2001.

[110] R. Herbrich, T. Minka, and T. Graepel. Trueskill: A bayesian skill rating system. *NIPS*, pages 569–576, 01 2006.

[111] R. Herzog, J.-F. Pietschmann, and M. Winkler. Optimal control of hughes' model for pedestrian flow via local attraction. *arXiv preprint arXiv:2011.03580*, 2020.

[112] K. Hirai and K. Tarui. A simulation of the behavior of a crowd in panic. *Systems and Control*, 1977.

[113] S. Hittmeir, L. Kanzler, A. Manhart, and C. Schmeiser. Kinetic modelling of colonies of myxobacteria. *arXiv preprint arXiv:2001.02711*, 2020.

[114] Q. Hong, M.-j. Lai, and J. Wang. The convergence of a numerical method for total variation flow. *Journal of Algorithms & Computational Technology*, 15:17483026211011323, 2021.

[115] H. Huang and J. Qiu. The microscopic derivation and well-posedness of the stochastic keller–segel equation. *Journal of nonlinear science*, 31(1):1–31, 2021.

[116] H.-J. Huang and R.-Y. Guo. Static floor field and exit choice for pedestrian evacuation in rooms with internal obstacles and multiple exits. *Physical Review E*, 78(2):021131, 2008.

[117] R. Hughes. A continuum theory for the flow of pedestrians. *Transportation Research Part B: Methodological*, 36:507–535, 07 2002.

[118] S.-R. Hysing and S. Turek. The eikonal equation: numerical efficiency vs. algorithmic complexity on quadrilateral grids. In *Proceedings of ALGORITMY*, volume 22, 2005.

[119] O. A. Igoshin, R. Welch, D. Kaiser, and G. Oster. Waves and aggregation patterns in myxobacteria. *Proceedings of the National Academy of Sciences*, 101(12):4256–4261, 2004.

[120] A. Ihsan and J. Tuwankotta. Godunov method for stefan problems with neumann and robin type boundary condition using dimensionless enthalpy formulation. In *AIP Conference Proceedings*, volume 2296, page 020086. AIP Publishing LLC, 2020.

[121] P.-E. Jabin and S. Junca. A Continuous Model For Ratings. *SIAM Journal on Applied Mathematics*, 75(2):420–442, 2015.

[122] P.-E. Jabin and Z. Wang. Mean field limit for stochastic particle systems. In *Active Particles, Volume 1*, pages 379–402. Springer, 2017.

[123] A. Johansson. Data-driven modeling of pedestrian crowds. 2009.

[124] A. Johansson and D. Helbing. Analysis of empirical trajectory data of pedestrians. *Pedestrian and Evacuation Dynamics 2008*, pages 203–214, 12 2010.

[125] S. Junca. Contractions to update Elo ratings for round-robin tournaments. 2021. Preprint.

[126] A. Jüngel. Mathematische modellierung mit differentialgleichungen. *Vorlesungsskript. Fachbereich Mathematik und Informatik Johannes Gutenberg-Universität Mainz*, page 151, 2003.

[127] A. Jüngel. The boundedness-by-entropy method for cross-diffusion systems. *Nonlinearity*, 28(6):1963, 2015.

[128] L. Kanzler. *Kinetic modelling of colonies of myxobacteria.* PhD thesis, Universität Wien, Wien, 2021.

[129] L. Kanzler and C. Schmeiser. Kinetic model for myxobacteria with directional diffusion. *arXiv preprint arXiv:2109.13184*, 2021.

[130] L. Kanzler, C. Schmeiser, and V. Tora. Two kinetic models for non-instantaneous binary alignment collisions. *arXiv preprint arXiv:2203.15711*, 2022.

[131] A. Kar and J. Mazumder. Analytic solution of the stefan problem in finite mediums. *Quarterly of Applied Mathematics*, 52(1):49–58, 1994.

[132] E. F. Keller and L. A. Segel. Initiation of slime mold aggregation viewed as an instability. *Journal of theoretical biology*, 26(3):399–415, 1970.

[133] C. T. Kelley. *Iterative methods for linear and nonlinear equations.* SIAM, 1995.

[134] S. K. Kim and D. Kaiser. C-factor: a cell-cell signaling protein required for fruiting body morphogenesis of m. xanthus. *Cell*, 61(1):19–26, 1990.

[135] A. Kirchner, K. Nishinari, and A. Schadschneider. Friction effects and clogging in a cellular automaton model for pedestrian dynamics. *Physical review E*, 67(5):056122, 2003.

[136] A. Kirchner and A. Schadschneider. Simulation of evacuation processes using a bionics-inspired cellular automaton model for pedestrian dynamics. *Physica A: Statistical Mechanics and its Applications*, 312:260–276, 09 2002.

[137] A. Kirchner and A. Schadschneider. Simulation of evacuation processes using a bionics-inspired cellular automaton model for pedestrian dynamics. *Physica A: statistical mechanics and its applications*, 312(1-2):260–276, 2002.

[138] C. Koutschan, H. Ranetbauer, G. Regensburger, and M.-T. Wolfram. Symbolic derivation of mean-field PDEs from lattice-based models. *2015 17th International Symposium on Symbolic and Numeric Algorithms for Scientific Computing (SYNASC)*, pages 27–33, 2015.

[139] S. Krauß, P. Wagner, and C. Gawron. Metastable states in a microscopic model of traffic flow. *Physical Review E*, 55(5):5597, 1997.

[140] T. Kretz. An overview of fundamental diagrams of pedestrian dynamics. 10 2019.

[141] K. Krupp. *Kinetische Modelle für die Rangeinstufung von Spielern.* Master's thesis, WWU Münster, 2016.

[142] O. Ladyzhenskaya. *Linear and Quasilinear Elliptic Equations.* ISSN. Elsevier Science, 1968.

[143] O. E. Lanford. Time evolution of large classical systems. *Dynamical systems, theory and applications*, pages 1–111, 1975.

[144] C. Lattanzio, A. Maurizi, and B. Piccoli. Moving bottlenecks in car traffic flow: a pde-ode coupled model. *SIAM Journal on Mathematical Analysis*, 43(1):50–67, 2011.

[145] P. LeFloch. Explicit formula for scalar nonlinear conservation laws with boundary condition. *Mathematical Methods in the Applied Sciences*, 10(3):265–287, 1988.

[146] P. LeFloch and J.-C. Nédélec. Explicit formula for weighted scalar nonlinear hyperbolic conservation laws. *Transactions of the American Mathematical Society*, 308(2):667–683, 1988.

[147] C. Lehrenfeld. *On a Space-Time Extended Finite Element Method for the Solution of a Class of Two-Phase Mass Transport Problems.* PhD thesis, RWTH Aachen, February 2015.

[148] O. Leingang. *Continuous and discrete approximations of cross-diffusion and chemotaxis systems.* PhD thesis, Technische Universität Wien, 2019.

[149] A. Y. Leroux. *Approximation de quelques problèmes hyperboliques non-linéaires.* Thèse d'état, Rennes, 1979.

[150] R. J. LeVeque and R. J. Leveque. *Numerical methods for conservation laws*, volume 214. Springer, 1992.

[151] M. Levy, H. Levy, and S. Solomon. A microscopic model of the stock market: cycles, booms, and crashes. *Economics Letters*, 45(1):103–111, 1994.

[152] P. Lin, J. Ma, T. Liu, T. Ran, Y. Si, and T. Li. An experimental study of the "faster-is-slower" effect using mice under panic. *Physica A: Statistical Mechanics and its Applications*, 452:157–166, 2016.

[153] D. P. Luigi Ambrosio, Nicola Fusco. *Functions of bounded variation and free discontinuity problems.* Oxford Mathematical Monographs. Oxford University Press, USA, 2000.

[154] B. B. Mandelbrot and R. L. Hudson. *The (mis) behaviour of markets: a fractal view of risk, ruin and reward.* Profile books, 2010.

[155] A. Masoudi-Nejad, G. Bidkhori, S. H. Ashtiani, A. Najafi, J. H. Bozorgmehr, and E. Wang. Cancer systems biology and modeling: microscopic scale and multiscale approaches. In *Seminars in cancer biology*, volume 30, pages 60–69. Elsevier, 2015.

[156] B. Maury. A time-stepping scheme for inelastic collisions. *Numerische Mathematik*, 102(4):649–679, 2006.

[157] B. Maury and S. Faure. *Crowds in equations*. Advanced Textbooks in Mathematics. World Scientific Publishing Co. Pte. Ltd., Hackensack, NJ, 2019. An introduction to the microscopic modeling of crowds, With a foreword by Laure Saint-Raymond.

[158] B. Maury and J. Venel. A discrete contact model for crowd motion. *ESAIM: Mathematical Modelling and Numerical Analysis*, 45(1):145–168, 2011.

[159] J. C. Maxwell. Iv. on the dynamical theory of gases. *Philosophical transactions of the Royal Society of London*, (157):49–88, 1867.

[160] C. M. Mayr and G. Köster. Social distancing with the optimal steps model. *Collective Dynamics*, 6:1–24, Dec. 2021.

[161] A. M. Meirmanov. *The stefan problem*, volume 3. Walter de Gruyter, 2011.

[162] F. Miksch, C. Urach, N. Popper, G. Zauner, G. Endel, I. Schiller-Frühwirth, and F. Breitenecker. Pin101 new insights on the spread of influenza through agent based epidemic modeling. *Value in Health*, 14(7):A284, 2011.

[163] T. Minka, R. Cleven, and Y. Zaykov. Trueskill 2: An improved bayesian skill rating system. *Technical Report*, 2018. Accessed: 2021-10-22.

[164] S. Mischler and C. Mouhot. Stability, convergence to self-similarity and elastic limit for the boltzmann equation for inelastic hard spheres. *Communications in Mathematical Physics*, 288(2):431–502, 2009.

[165] S. Mischler, C. Mouhot, and M. R. Ricard. Cooling process for inelastic boltzmann equations for hard spheres, part i: The cauchy problem. *Journal of statistical physics*, 124(2):655–702, 2006.

[166] J. Monod. The growth of bacterial cultures. *Annual review of microbiology*, 3(1):371–394, 1949.

[167] J. J. Moreau. Evolution problem associated with a moving convex set in a hilbert space. *Journal of differential equations*, 26(3):347–374, 1977.

[168] P. M. Morse and H. Feshbach. Methods of theoretical physics. *American Journal of Physics*, 22(6):410–413, 1954.

[169] S. Motsch and D. Peurichard. From short-range repulsion to hele-shaw problem in a model of tumor growth. *Journal of mathematical biology*, 76(1):205–234, 2018.

[170] M. Moussaïd, D. Helbing, S. Garnier, A. Johansson, M. Combe, and G. Theraulaz. Experimental study of the behavioural mechanisms underlying self-organization in human crowds. *Proceedings. Biological sciences / The Royal Society*, 276:2755–62, 06 2009.

[171] O. R. Musin. Properties of the delaunay triangulation. In *Proceedings of the thirteenth annual symposium on Computational geometry*, pages 424–426, 1997.

[172] T. N. Narasimhan. Fourier's heat conduction equation: History, influence, and connections. *Reviews of Geophysics*, 37(1):151–172, 1999.

[173] A. Nicolas. Dense pedestrian crowds versus granular packings: An analogy of sorts. In *Traffic and Granular Flow 2019*, pages 411–419. Springer, 2020.

[174] S. Nowak and A. Schadschneider. Quantitative analysis of pedestrian counterflow in a cellular automaton model. *Physical Review E*, 85, 06 2012.

[175] S. Okazaki. A study of pedestrian movement in architectural space. *Trans. of A.I.J.*, 283, 1979.

[176] P. C. Ordeshook et al. Game theory and political theory. *Cambridge Books*, 1986.

[177] G. C. Papanicolaou. Asymptotic analysis of transport processes. *Bulletin of the American Mathematical Society*, 81(2):330–392, 1975.

[178] L. Pareschi and G. Toscani. *Interacting multiagent systems. Kinetic equations and Monte Carlo methods*. Oxford University Press, 11 2013.

[179] L. Pareschi and G. Toscani. Wealth distribution and collective knowledge: a boltzmann approach. *Philosophical Transactions of the Royal Society A: Mathematical, Physical and Engineering Sciences*, 372(2028):20130396, 2014.

[180] L. Pareschi, G. Toscani, A. Tosin, and M. Zanella. Hydrodynamic models of preference formation in multi-agent societies. *J. Nonlinear Sci.*, 29(6):2761–2796, 2019.

[181] J. M. Pastor, A. Garcimartín, P. A. Gago, J. P. Peralta, C. Martín-Gómez, L. M. Ferrer, D. Maza, D. R. Parisi, L. A. Pugnaloni, and I. Zuriguel. Experimental proof of faster-is-slower in systems of frictional particles flowing through constrictions. *Physical Review E*, 92(6):062817, 2015.

[182] J. A. Perez. *Convergence of numerical schemes in the total variation sense*. New York University, 2004.

[183] B. Perthame et al. *Kinetic formulation of conservation laws*, volume 21. Oxford University Press, 2002.

[184] D. Peurichard, F. Delebecque, A. Lorsignol, C. Barreau, J. Rouquette, X. Descombes, L. Casteilla, and P. Degond. Simple mechanical cues could explain adipose tissue morphology. *Journal of theoretical biology*, 429:61–81, 2017.

[185] B. Piccoli and A. Tosin. Time-evolving measures and macroscopic modeling of pedestrian flow. *Archive for Rational Mechanics and Analysis*, 199(3):707–738, Mar 2011.

[186] R. Pinnau and C. Totzeck. Space mapping-based receding horizon control for stochastic interacting particle systems: dogs herding sheep, 2019.

[187] J. Pitt-Francis, P. Pathmanathan, M. O. Bernabeu, R. Bordas, J. Cooper, A. G. Fletcher, G. R. Mirams, P. Murray, J. M. Osborne, A. Walter, et al. Chaste: a test-driven approach to software development for biological modelling. *Computer Physics Communications*, 180(12):2452–2471, 2009.

[188] S. Price. How fifa's new ranking system will change international soccer. *Forbes*, 2018. Accessed: 2021-10-22.

[189] J. Qian, Y.-T. Zhang, and H.-K. Zhao. Fast sweeping methods for eikonal equations on triangular meshes. *SIAM J. Numerical Analysis*, 45:83–107, 01 2007.

[190] H. Ranetbauer. *Asymptotic Gradient Flow Structures in Interacting Particle Systems.* PhD thesis, Linz, 2018.

[191] L. Robert, M. Hoffmann, N. Krell, S. Aymerich, J. Robert, and M. Doumic. Division in escherichia coliis triggered by a size-sensing rather than a timing mechanism. *BMC biology*, 12(1):1–10, 2014.

[192] P. Romanczuk, U. Erdmann, H. Engel, and L. Schimansky-Geier. Beyond the Keller-Segel model. *The European Physical Journal Special Topics*, 157(1):61–77, 2008.

[193] L. Rubinstein. *The Stefan Problem*, volume 8. American Mathematical Soc., 2000.

[194] C. Rudloff, T. Matyus, and S. Seer. Comparison of different calibration techniques on simulated data. In *Pedestrian and Evacuation Dynamics 2012*, pages 657–672. Springer, 2014.

[195] B. Sager and D. Kaiser. Intercellular c-signaling and the traveling waves of myxococcus. *Genes & Development*, 8(23):2793–2804, 1994.

[196] E. Samanidou, E. Zschischang, D. Stauffer, and T. Lux. Agent-based models of financial markets. *Reports on Progress in Physics*, 70(3):409, 2007.

[197] L. Samuelson. Game theory in economics and beyond. *Journal of Economic Perspectives*, 30(4):107–30, 2016.

[198] A. Schadschneider, C. Eilhardt, S. Nowak, and R. Will. Towards a calibration of the floor field cellular automaton. *Pedestrian and Evacuation Dynamics*, pages 557–566, 01 2011.

[199] A. Schadschneider, H. Klüpfel, T. Kretz, C. Rogsch, and A. Seyfried. *Fundamentals of Pedestrian and Evacuation Dynamics*, pages 124–154. IGI Global, 06 2009.

[200] B. A. Schlake. *Mathematical models for particle transport: Crowded motion.* PhD thesis, Westfälische Wilhelms-Universität Münster, 2011.

[201] M. J. Seitz and G. Köster. Natural discretization of pedestrian movement in continuous space. *Physical Review E*, 86(4):046108, 2012.

[202] J. A. Sethian. A fast marching level set method for monotonically advancing fronts. *Proceedings of the National Academy of Sciences*, 93(4):1591–1595, 1996.

[203] E. T. Seung-Yeal Ha. From particle to kinetic and hydrodynamic descriptions of flocking. *Kinetic and Related Models*, 1, 2008.

[204] N. Silver and R. Fischer-Baum. How we calculate nba elo ratings, 2015. Accessed: 2021-10-22.

[205] J. Simon. Compact sets in the space $L^p(O,T;B)$. *Annali di Matematica pura ed applicata*, 146(1):65–96, 1986.

[206] L. Simon et al. *Lectures on geometric measure theory.* The Australian National University, Mathematical Sciences Institute, Centre ..., 1983.

[207] M. J. Simpson, K. A. Landman, and B. D. Hughes. Multi-species simple exclusion processes. *Physica A: Statistical Mechanics and its Applications*, 388(4):399–406, 2009.

[208] S. A. Soria, R. Josens, and D. R. Parisi. Experimental evidence of the "faster is slower" effect in the evacuation of ants. *Safety science*, 50(7):1584–1588, 2012.

[209] L. Tao. Solidification of a binary mixture with arbitrary heat flux and initial conditions. *Archive for Rational Mechanics and Analysis*, 76:167–181, 1981.

[210] L. N. TAO. ON SOLIDIFICATION OF A BINARY ALLOY. *The Quarterly Journal of Mechanics and Applied Mathematics*, 33(2):211–225, 05 1980.

[211] D. Tarwidi and S. Pudjaprasetya. Godunov method for stefan problems with enthalpy formulations. *East Asian Journal on Applied Mathematics*, 3:2013, 05 2013.

[212] K. Teknomo, Y. Takeyama, and H. Inamura. Review on microscopic pedestrian simulation model. *arXiv preprint arXiv:1609.01808*, 2016.

[213] G. Teschl. *Ordinary differential equations and dynamical systems*, volume 140. American Mathematical Soc., 2012.

[214] G. Toscani. Kinetic models of opinion formation. *Comm. Math. Sci.*, 4(3):481–496, 2006.

[215] G. Toscani. Kinetic models of opinion formation. *Commun. Math. Sci.*, 4, 09 2006.

[216] P. T. Tošic and G. A. Agha. Parallel vs. sequential threshold cellular automata: Comparison and contrast. 2005.

[217] A. Tosin and M. Zanella. Boltzmann-type description with cutoff of follow-the-leader traffic models. In *Trails in Kinetic Theory*, pages 227–251. Springer, 2021.

[218] J. Towers. Convergence of a difference scheme for conservation laws with a discontinuous flux. *SIAM Journal on Numerical Analysis*, 38, 12 1999.

[219] X. Trepat and J. J. Fredberg. Plithotaxis and emergent dynamics in collective cellular migration. *Trends in cell biology*, 21(11):638–646, 2011.

[220] A. Tveito. Convergence and stability of the lax-friedrichs scheme for a nonlinear parabolic polymer flooding problem. *Advances in Applied Mathematics*, 11(2):220–246, 1990.

[221] M. Twarogowska, P. Goatin, and R. Duvigneau. Comparative study of macroscopic pedestrian models. *Transportation Research Procedia*, 2, 12 2014.

[222] L. D. Vanumu, K. Ramachandra Rao, and G. Tiwari. Fundamental diagrams of pedestrian flow characteristics: A review. *European transport research review*, 9(4):1–13, 2017.

[223] R. Viborni. On properties of solutions of some boundary value problems for equations of parabolic type. *Doklady Akad. Nauk SSSR (n.s.)*, 117:563–565, 1957.

[224] T. Vicsek, A. Czirók, E. Ben-Jacob, I. Cohen, and O. Shochet. Novel type of phase transition in a system of self-driven particles. *Phys. Rev. Lett.*, 75:1226–1229, Aug 1995.

[225] P. Wang, L. Robert, J. Pelletier, W. L. Dang, F. Taddei, A. Wright, and S. Jun. Robust growth of escherichia coli. *Current biology*, 20(12):1099–1103, 2010.

[226] U. Weidmann. *Transporttechnik der Fussgänger: transporttechnische Eigenschaften des Fussgängerverkehrs*. Schriftenreihe des IVT. IVT, 1993.

[227] U. Weidmann, U. Kirsch, and M. Schreckenberg. *Pedestrian and evacuation dynamics 2012*. Springer Science & Business, 2014.

[228] W. Weng, T. Chen, H. Yuan, and W. Fan. Cellular automaton simulation of pedestrian counter flow with different walk velocities. *Physical Review. E*, 74:036102, 10 2006.

[229] T. Witelski and M. Bowen. *Methods of mathematical modelling*. Springer, 2015.

[230] M. L. Woods, C. Carmona-Fontaine, C. P. Barnes, I. D. Couzin, R. Mayor, and K. M. Page. Directional collective cell migration emerges as a property of cell interactions. *PLoS One*, 9(9):e104969, 2014.

[231] Y. Xiao, M. Yang, Z. Zhu, H. Yang, L. Zhang, and S. Ghader. Modeling indoor-level non-pharmaceutical interventions during the covid-19 pandemic: a pedestrian dynamics-based microscopic simulation approach. *Transport policy*, 109:12–23, 2021.

[232] Q. Xu, M. Chraibi, and A. Seyfried. Anticipation in a velocity-based model for pedestrian dynamics. *Transportation research part C: emerging technologies*, 133:103464, 2021.

[233] Q. Xu, M. Chraibi, and A. Seyfried. Prolonged clogs in bottleneck simulations for pedestrian dynamics. *Physica A: Statistical Mechanics and its Applications*, 573:125934, 2021.

[234] K. Yamori. Going with the flow: Micro–macro dynamics in the macrobehavioral patterns of pedestrian crowds. *Psychological review*, 105(3):530, 1998.

[235] C. Yates, A. Parker, and R. Baker. Incorporating pushing in exclusion-process models of cell migration. *Physical Review E*, 91, 04 2015.

[236] Z. You, D. J. Pearce, A. Sengupta, and L. Giomi. Geometry and mechanics of microdomains in growing bacterial colonies. *Physical Review X*, 8(3):031065, 2018.

[237] Y. Zhao and H. Zhang. A unified follow-the-leader model for vehicle, bicycle and pedestrian traffic. *Transportation research part B: methodological*, 105:315–327, 2017.

[238] I. Zuriguel, J. Olivares, J. M. Pastor, C. Martín-Gómez, L. M. Ferrer, J. J. Ramos, and A. Garcimartín. Effect of obstacle position in the flow of sheep through a narrow door. *Physical Review E*, 94(3):032302, 2016.

[239] I. Zuriguel, D. R. Parisi, R. C. Hidalgo, C. Lozano, A. Janda, P. A. Gago, J. P. Peralta, L. M. Ferrer, L. A. Pugnaloni, E. Clément, et al. Clogging transition of many-particle systems flowing through bottlenecks. *Scientific reports*, 4(1):1–8, 2014.